Important Notice

UNIVERSITY OF CALGARY

The use of common scatter point gathers to detect amplitude variation with offset

by

Shuang Sun

A THESIS

SUBMITTED TO THE FACULTY OF GRADUATE STUDIES

IN PARTIAL FULFILLMENT OF THE REQUIREMENTS FOR THE

DEGREE OF MASTER OF SCIENCE

DEPARTMENT OF GEOLOGY AND GEOPHYSICS

CALGARY, ALBERTA

March, 2003

THE UNIVERSITY OF CALGARY
FACULTY OF GRADUATE STUDIES

The undersigned certify that they have read, and recommended to the Faculty of Graduate Studies for acceptance the thesis entitled " The use of common scatter point gathers to detect amplitude variation with offset " submitted by Shuang Sun in partial fulfillment of the requirements for the degree of Master of Science.

                                           Supervisor, Dr. John C. Bancroft
                                           Department of Geology and Geophysics

                                           Dr. Larry R. Lines
                                           Department of Geology and Geophysics

                                           Dr. Jim W. Haslett
                                           Department of Electrical and Computer Engineering

Date

ABSTRACT

The use of common scatterpoint (CSP) gathers for amplitude variation with offset analysis is investigated. Both the migration aperture and the scaling factor used during CSP gathering are considered. The Fresnel zone concept was expanded for an offset section and then generalized to the prestack data volume, to define the minimum migration aperture. A migration aperture larger than this size had no improvement on the migration amplitude.

Three methods are presented that use limited aperture and different weighting schemes when forming the CSP gathers. The first method uses an aperture that is half the size of the Fresnel zone along with a fold balancing scheme that is based on the sample fold. The second method uses the full size of the Fresnel zone and scaling with the equivalent wavenumber migration (EWM) weighting function. The third method also uses the full size of the Fresnel zone but with an exponential scaling factor. The three methods are applied both to synthetic and field data. The results verify that the first and third approximations provide reliable amplitudes in the CSP gather that can be used for amplitude variation with offset (AVO) analysis.

ACKNOWLEDGEMENTS

To the love of my life: Zhong and Dudu

TABLE OF CONTENTS

LIST OF FIGURES

Chapter 1

An introduction to angle dependent reflectivity

1.1 Chapter summary

The variation of reflection and transmission coefficients with angle of incidence (AVA) (and corresponding increasing offset) is often referred to as offset-dependent reflectivity, and is the basis for amplitude-versus-offset (AVO) analysis. In the late 1960s, several oil companies noticed that, in environments of young clastic sediments, large seismic amplitudes were associated with gas-saturated sands. This method of correlating lithology to normal incidence reflectivities was appropriately named the 'bright spot' technique. For the next decade, geophysicists tried numerous techniques to resolve the ambiguity associated with lithologic identification by means of normal incidence reflectivities. Finally, in the early 1980's, Ostrander's work on AVO led to the AVO tool for gas-saturated sand detection, based on the principle that the reflection is angle-dependent, over the past twenty years, AVO has evolved from a relatively new technology to an increasingly mature application. Today, AVO analysis is widely used in hydrocarbon detection, lithology identification and fluid parameter analysis due to the fact that seismic amplitudes at reflection boundaries are affected by the variation of physical properties above and below the boundaries.

In this Chapter, the theory of AVO analysis is introduced. In addition, the accuracy of the Aki and Richards approximation, which is used widely today and is used in this thesis for calculating *P-P* reflection coefficients, is tested.

1.2 The compressional wave propagation

In seismic exploration, the seismic waves propagate through a complex underground medium. Various energy reflections, transmissions, conversions and attenuations occur within this process, which may not be described in exact terms, given the complex nature of the physical properties of earth media. Some understanding of the phenomena observed in seismic exploration may be derived from the use of a simplified model, such as a layered earth model, which is usually assumed in the study of AVO phenomena, and the single reflection interface, which is investigated as a starting point for AVO analysis. In conventional seismic exploration, waves that are generated by a source and reflected by the subsurface, are usually regarded as compressional (P) waves. The compressional wave's propagation becomes fundamental in AVO analysis. When the compressional wave travels down to a reflector that is more than several wavelengths from the source point, it is regarded as a plane wave that obeys Snell's law. Plane wave incidence is another fundamental principal in AVO analysis, and this assumption leads to difficulties for AVO analysis after prestack migration.

1.3 Snell's law and Zoeppritz equation

When the compressional plane wave propagates across a medium interface that has different properties on each side, the energy carried by the wave is reflected and transmitted in the form of compressional (P) waves and converted shear (S) waves. As described above, the incident plane wave obeys Snell's law as shown in Figure 1.1.
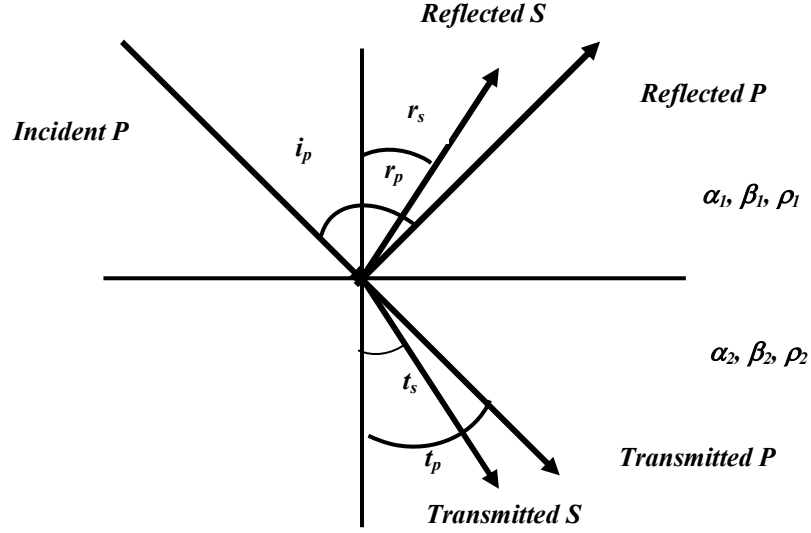
Figure 1.1. Incident P wave generates four kinds of waves at an interface.

Figure 1.1 illustrates the wave propagation of a compressional wave at a welded solid-solid interface between two infinite elastic half spaces. The sine of the incident angle i_p, reflection angle r_s and r_p, and transmitted angle t_s and t_p, together with P wave velocities, α_1 and α_2, and S wave velocities, β_1 and β_2, of both sides, obey Snell's law as described by equation (1.1).

$$\frac{\sin(i_p)}{\alpha_1} = \frac{\sin(r_p)}{\alpha_1} = \frac{\sin(r_s)}{\beta_1} = \frac{\sin(t_p)}{\alpha_2} = \frac{\sin(t_s)}{\beta_2} = p, \qquad (1.1)$$

where p is the ray parameter.

Knott (1899) and Zoeppritz (1919) invoked continuity of displacement and stress at the reflecting interface as boundary conditions to solve for the reflection and transmission coefficients as functions of incident angle, and the elastic properties of the media (densities, bulk and shear modulus). However, the resulting Knott and Zoeppritz's equations are notoriously complex. Aki and Richards (1980) and Waters (1981) gave an easily solved matrix form

$$Q = P^{-1}R, \qquad (1.2)$$

where Q, P, and R are given in Castagna and Backus, 1993.

For the ideal interface and incident plane wave, the Zoeppritz equations describe the relationships among the incident, transmitted and reflected waves. Aki and Richards (1980) expressed the Zoeppritz equations in convenient forms. In this thesis, only the reflection coefficient of the *P-P* wave is studied. The reflection coefficient of the incident *P* wave and reflected *P* wave is shown as follows:

$$R_{pp} = \left[\left(b \frac{\cos(i_p)}{\alpha_1} - c \frac{\cos(t_p)}{\alpha_2} \right) F - \left(a + d \frac{\cos(i_p)}{\alpha_1} \frac{\cos(r_s)}{\beta_1} \right) Hp^2 \right] / D, \qquad (1.3)$$

where

$$a = \rho_2(1 - 2\beta_2^2 p^2) - \rho_1(1 - 2\beta_1^2 p^2),$$

$$b = \rho_2(1 - 2\beta_2^2 p^2) + 2\rho_1\beta_1^2 p^2,$$

$$c = \rho_1(1 - 2\beta_1^2 p^2) + 2\rho_2\beta_2^2 p^2,$$

$$d = 2(\rho_2\beta_2^2 - \rho_1\beta_1^2),$$

$$E = b \frac{\cos(i_p)}{\alpha_1} + c \frac{\cos(t_p)}{\alpha_2},$$

$$F = b \frac{\cos(r_s)}{\beta_1} + c \frac{\cos(t_s)}{\beta_2},$$

$$G = a - d \frac{\cos(i_p)}{\alpha_1} \frac{\cos(t_s)}{\beta_2},$$

$$H = a - d \frac{\cos(t_p)}{\alpha_2} \frac{\cos(r_s)}{\beta_1},$$

and

$$D = EF + GHp^2.$$

In this solution of the Zoeppritz equation, the reflection coefficients of the *P-P* wave is expressed as a function of incident, reflected, and transmitted angles along with the compressional and shear velocities and densities from both sides of the interface. The Zoeppritz equations provide solutions for any ideal plane wave propagation case.

From this simplified equation, Koefoed (1955) first pointed out the practical possibilities of using AVO analysis as an indicator of V_P/V_S variations and empirically established several rules, which were later verified by Shuey (1985) for moderate angles of incidence. Four rules among them are:

a) When the underlying medium has the greater longitudinal [P-wave] velocity and other relevant properties of the two strata are equal to each other, an increase of Poisson's ratio for the underlying medium, causes an increase of the reflection coefficient at the larger angles of incidence (in Encyclopedic Dictionary of Exploration Geophysics, the Poisson's ratio is defined as: the ratio of the fractional transverse contraction to the fraction longitudinal extension when a rod is stretched, and can be expressed by the ratio of P- and S- wave velocities).

b) When, in the above case, Poisson's ratio for the incident medium is increased, the reflection coefficient at the larger angles of incidence is decreased.

c) When, in the above case, Poisson's ratios for both media are increased and kept equal to each other, the reflection coefficient at the larger angles of incidence is increased.

d) The effect mentioned in (a) becomes more pronounced as the velocity contrast becomes smaller.

Bortfeld (1961) linearized the Zoeppritz equations by assuming small changes in layer properties $\left(\Delta\rho/\rho, \Delta V_P/V_P, \Delta V_S/V_S \ll 1\right)$. This approach was also followed by Aki and Richards (1980), who derived a form of approximation parameterized in terms of the changes in density, P-wave velocity, and S-wave velocity across the interface, as will be introduced next.

1.4 Aki and Richards' approximation of *P-P* reflection coefficient

1.4.1 Simplified and meaningful equations

Although the Zoeppritz equations have exact solutions for reflection coefficients, it is not easy to directly apply them to the actual seismic data. One reason is that if the

subsurface is to be evaluated using the Zoeppritz equations, too many unknowns exist. Secondly, because of the complex nature of the earth, the seismic record is not composed of ideal reflected plane waves. Equations with a simple format and good accuracy have been sought by researchers. Aki and Richards (1980) gave approximations for reflection coefficients. These approximations are simpler and more practical than the Zoeppritz equations and the reflection coefficient of a *P-P* wave is expressed as:

$$R_{pp} = \frac{1}{2}(1 - 4\beta^2 p^2)\frac{\Delta\rho}{\rho} + \frac{1}{2\cos^2 i}\frac{\Delta\alpha}{\alpha} - 4\beta^2 p^2 \frac{\Delta\beta}{\beta}, \qquad (1.4)$$

The elastic properties evident in the above equation are related as follows to those on each side of the interface:

$$\Delta\alpha = \alpha_2 - \alpha_1,$$

$$\alpha = \frac{\alpha_1 + \alpha_2}{2},$$

$$\Delta\beta = \beta_2 - \beta_1,$$

$$\beta = \frac{\beta_2 + \beta_1}{2},$$

$$\Delta\rho = \rho_2 - \rho_1,$$

$$\rho = \frac{\rho_2 + \rho_1}{2},$$

$$i = \frac{i_p + t_p}{2},$$

and

$$j = \frac{r_s + t_s}{2}.$$

1.4.2 Ostrander's Hypothetical Gas Sand Model

Aki and Richards' approximations of reflection coefficients have good accuracy when the property contrast and incident angles are small. The requirement of small property contrast is generally satisfied in the real cases (usually less than *0.1*). Ostrander (1984),

devised a hypothetical gas sand model to analyze the plane wave reflection coefficients as a function of the angle of incidence, and to test the accuracy of various approximations of reflection coefficients. Figure 1.2 shows this three-layer gas sand model with parameters that are typical for a shallow young geologic section. Here, gas sand with a Poisson's ratio of *0.1* is embedded in shale having a Poisson's ratio of *0.4*. There is a *20% P* wave velocity reduction going into the sand, from *10,000 ft/s* to *8000 ft/s,* a *10%* density reduction from *2.40 g/cm³* to *2.14 g/cm³*, and an increase of *S* wave velocity from *4082 ft/s* to *5333 ft/s*. The Poisson's ratio becomes *0.4* if there is no gas in the sand layer, thus simulating the case of low velocity, brine-saturated young sandstone embedded in shale. This kind of AVO phenomena generates a bright spot of stacked data. In this thesis, this model is used as a synthetic data example.
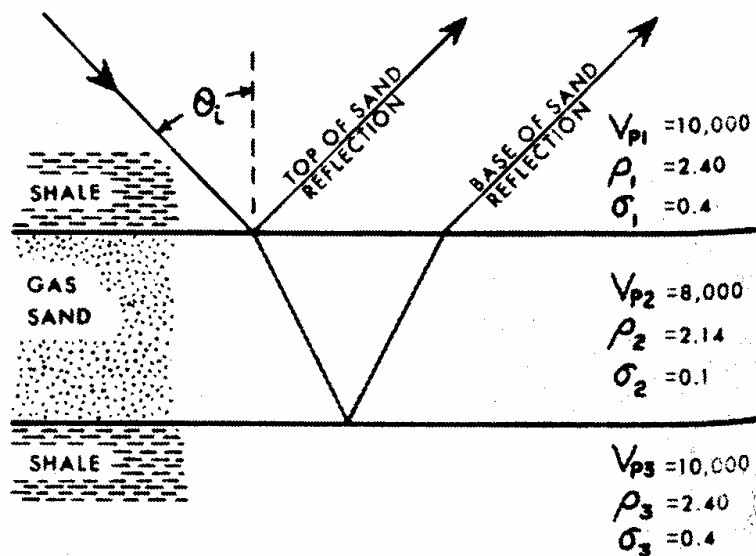
Figure 1.2. Ostrander's Gas Sand Model.

1.4.3 Accuracy of Aki and Richards' approximation

Before applying the approximation, the accuracy is tested for reliability. In Figure 1.3, the exact *P-P* reflection coefficient, as defined by Zoeppritz equation and the

reflection coefficient by Aki and Richards approximation, are compared for the media with the elastic properties specified in Figure 1.2. The solid lines represent the exact reflection coefficient and the broken lines represent Aki-Richards' approximations of the reflection coefficient. The case without gas in the sand of the second layer shown in Figure 1.2 are also presented in Figure 1.3, using a Poisson ratio of *0.4*. Part (a) shows the *P-P* reflection coefficient for the two interfaces in Figure 1.2 with gas in the sand layer. Part (b) shows the *P-P* reflection coefficient for the two interfaces in Figure 1.2 without gas in the sand layer. After comparing the two parts, it is observed that Aki and Richards' approximation demonstrates the sufficient accuracy for AVO analysis under certain assumptions and conditions.
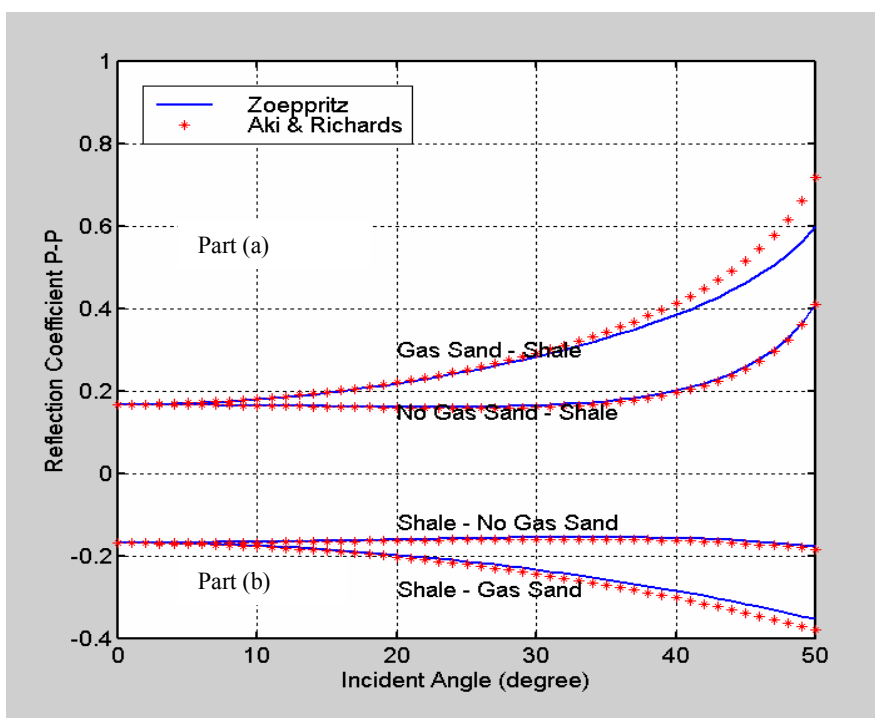
Figure 1.3. The accuracy of Aki & Richards approximation of the P-P reflection coefficient is compared with the full Zoeppritz equation.

1.5 Seismic data processing flow for AVO analysis

When selecting an appropriate data processing scheme for AVO analysis, two factors must be considered seriously, as Castagna pointed out in 1993:

1. Noise suppression and isolation of the reflectivity of the event of interest;
2. Not biasing or otherwise corrupting the reflectivity variation with offset.

1.5.1 Several processing schemes

Ostrander (1984), presented a useful processing scheme, which is composed of seven steps and terminates before stack.

1. Spherical divergence correction
2. Exponential gain correction
3. Minimum-phase spiking deconvolution
4. Velocity analysis
5. NMO correction
6. Trace equalization
7. Horizontal trace summing.

Chiburis (1984), presented another processing flow as:

1. Mild f-k multiple suppression
2. Spherical divergence and NMO correction
3. Whole-trace equalization
4. Flattening on a consistent reference event
5. Horizontal trace summing
6. Peak amplitude picked interactively
7. Smoothed least-squares curve fitting
8. Despiking of outliers
9. Curve refitting
10. Result clipped and smoothed.

Yu (1985), presented another processing flow as:

1. Apply exponential gain, suppress coherent noise, and remove gain.
2. Offset compensation
3. Deconvolution
4. NMO correction
5. Surface consistent correction
6. Partial trace sum
7. Bandpass
8. Section dependent equalization

Although many authors had various schemes, the basic steps in so many flows includes:

1. Spherical divergence correction
2. Deconvolution
3. NMO correction

1.5.2 Do we need more steps?

As Castagna and Backus (Castagna and Backus, 1993) wrote: "All too often, however, the potential of AVO analysis has not been realized. Under proper (sometimes fortuitous) circumstances, AVO has proved to be a useful prospecting tool…. In other situations, the technique has simply failed." The list of AVO pitfalls is long and has forced geophysicists to look more deeply into certain areas of rock properties, seismic data acquisition, and seismic data processing than they had dreamed would be necessary 20 years ago. One problem for AVO analysis arises when we apply it on unmigrated data. In areas of structural geologic complexity, with gentle dips or moderate velocity variation, the amplitude anomalies may be uncertain. In stratigraphic areas, with geologic bed truncations or low-relief fault zones, the anomalies might be corrupted with diffraction energy. Since the search for hydrocarbons has pushed the use of AVO away from simple structures of sedimentary basins, problems such as these have become increasingly common.

The next step: prestack migration. Prestack migration is used most often as a tool for structural imaging problems, with only incidental regard for amplitude preservation. However, some of the developers of migration theory have realized the importance of preserving amplitude information during migration and have insisted on seeing it pushed into practice. Such amplitude-preserving migration called true amplitude migration, will be introduced in the next chapter.

1.6 Chapter conclusions

Seismic reflections are angle dependent. This property leads to an AVO technique as a tool for gas detection or as a lithology indicator. Geophysicists use the Zoeppritz equations and their approximations as an AVO analysis tool. Among these approximations, Aki and Richards (Aki and Richards, 1980) gave a simpler reflectivity equation, introduced and tested for accuracy in this Chapter, and this approximation will be used in this thesis for reflection coefficient calculations.

However the pitfalls of AVO analysis applied to unmigrated data should not be neglected. Recently, migration geophysicists have been trying to do AVO analysis after prestack migration. The next Chapters will discuss using common scatterpoint (CSP) gathers, which are formed during the equivalent offset method (EOM) of prestack migration, as an AVO tool. In doing this, both the migration aperture and the scaling factor during CSP gathering are determining factors. The size of the migration aperture will be discussed in Chapter 3, and the scaling factor during EOM will be discussed in Chapter 4. The results show that a CSP gather with limited aperture and proper scaling factor can be used as an AVO tool.

1.7 Summary of the thesis

The main objective of this thesis is to find a practical scaling method that can be applied during the kinematical formation of CSP gathers, so that the CSP gathers can be

used as an AVO tool. In doing this, approximations are used to get the approximated equivalent offset dependent reflectivity, instead of angle dependent reflectivity.

In Chapter 1, the preliminary theory of AVO or AVA analysis was introduced, and the accuracy of Aki and Richards approximation to calculate the reflection coefficient of the *P-P* wave was investigated. The accuracy test showed that the Aki and Richards approximation gives reliable reflectivity in the *P-P* wave case, compared with the full Zoeppritz calculation. Traditional AVO analysis in a common midpoint (CMP) gather assumes that the subsurface is horizontally layered. In fact, even with mild structure, the reflection point is smeared in a CMP gather. One more step is necessary for such structure: prestack migration.

In Chapter 2, the EOM migration algorithm will be introduced. Compared to other Kirchhoff migration algorithms, EOM has several advantages: it is faster, it provides a middle step to re-evaluated velocities, it is naturally anti-aliasing and it is not as sensitive to input velocity as other methods. The concept of true-amplitude migration and limited aperture migration will be discussed. True-amplitude migration is used as AVO/AVA analysis after prestack migration, and the concept is useful to determine the scaling factors or weighting functions used in EOM. Kirchhoff time migration methods are aperture dependent, so the size of aperture determines the migration result. With a certain size aperture, Kirchhoff migration methods provide reliable amplitudes.

The main contributions of this thesis can be introduced as follows:

1. The Fresnel zone size relates to the source wavelet. With different kinds of source wavelets, the Fresnel zone is different (in Chapter 3).
2. With a limited band seismic wavelet, the reflected energy reaches its maximum at the radius of the Fresnel zone size (in Chapter 3).
3. The amplitude of reflection is influenced by the reflector size. The amplitude variation with the reflector size in the zero offset case has been investigated using three typical reflector sizes, which are larger than the Fresnel zone size, equal to the Fresnel zone size and smaller than the Fresnel zone size (in Chapter 3).

4. The reflector edge effects on the amplitude are discussed (in Chapter 3).

5. The Fresnel zone concept is expanded to the offset section as defined in Section 3.6.

6. The Fresnel zone in prestack data volume, i.e. Cheops Pyramid, is described (in Chapter 3).

7. Minimum migration aperture is derived using the Fresnel zone concept in prestack data volume (in Chapter 3).

8. Note that when the aperture is larger than the Fresnel zone size, there is no change in the migration amplitude response. We therefore include a taper zone beyond the definition of migration aperture as it has no effect on the migration amplitude. If the taper were included within the aperture, then the shape of the taper would affect the migration amplitude (Other authors (Sun, 1996) included the taper in the definition of the migration aperture).

9. The smearing factors during CSP gathering are discussed (in Chapter 4).

10. Three kinds of scaling approximations were investigated during the CSP gathering. Reducing smearing effects and divided CSP gather by sample-by-sample fold with half the Fresnel zone size as aperture is the first kind of approximation. With Equivalent Wavenumber Migration (EWM)'s factor together with the Fresnel zone size as aperture scales the amplitude in the CSP gather is the second kind of approach. The third good approximation of scaling during CSP gathering is introduced: exponential scaling within the Fresnel zone (in Chapter 4).

In Chapter 5, the limited CSP gathering method will be applied both to synthetic data and field data. The synthetic data has two amplitude phenomena, one with the AVO anomaly and the other without. The field data is the Blackfoot dataset acquired in 1997.

Chapter 2

EOM and Limited Aperture Migration

2.1 Chapter summary

As mentioned in Chapter 1, analyzing seismic amplitude and its dependence on variations in rock properties, made its first impact on the hydrocarbon industry in the early 1980's. Its accumulated impact in the intervening years has been profound. Amplitude analysis i.e. AVO is used by geophysicists to detect gas sands and oil sands, and even to identify porosity and other fine scale properties of the rock. As also mentioned in Chapter 1, the processing flow for AVO analysis needs an additional step, i.e., prestack migration, to correct smearing in areas of even mild structural geologic complexity. Prestack migration is used most often as a tool for minimizing the problems with structural imaging. However, developers of migration theory have long realized the importance of preserving amplitude information during migration, and have persisted to see amplitude-preserving migration pushed into practice. Migration with preserved amplitude has the ability to sort the migrated data according to the incidence angle, and can therefore give more reliable estimates of amplitude variation with angle (AVA).

Equivalent offset prestack time migration (EOM) was first introduced by Bancroft and his co-workers at the University of Calgary (Bancroft and Geiger, 1994). EOM is a Kirchhoff prestack migration algorithm, and it is easier to implement and faster than conventional Kirchhoff prestack migration algorithms.

In this Chapter, the EOM algorithm is first introduced, followed by the concept of true-amplitude migration. Finally, limited aperture migration will be introduced.

2.2 EOM

2.2.1 Prestack Migration

The migration of seismic data is a process that attempts to reconstruct the image of the subsurface reflecting structure from a recorded seismic wavefield. In this thesis, migration related discussions focus on 2D Kirchhoff prestack time migration for pure-mode (no mode conversion), surface seismic data.

Scatter Point Model

In seismic data processing, the subsurface of the earth is often modelled as a layered medium with uniform acoustic properties. The reflection energy from the interface between the layers, can be considered as the sum of the scattered energy from a large number of points (referred to as scatterpoints), closely located on the interfaces. The reflection amplitude at each scatterpoint is taken as proportional to the reflection coefficient of the interface at this point location. This model is called the Scatterpoint Model, which forms the basis of Kirchhoff migration methods. The points that are not on any recognizable layer interface, but can still be considered as scatterpoints with zero or very small reflection amplitudes, enable the whole subsurface to be considered as a grid of scatterpoints.

The subsurface is initially considered as a one-layer isotropic medium, where the seismic compressional wave propagation velocity is a constant v. A scatterpoint at (x_{sp}, z_{sp}) and a source-receiver pair at surface location x_s and x_r with $z=0$, are identified in Figure 2.1. The travel time T of a seismic wave travelling from the source to the scatterpoint and then to the receiver can be expressed as

$$T = \frac{1}{v}\left(\sqrt{z_{sp}^2 + (x_s - x_{sp})^2} + \sqrt{z_{sp}^2 + (x_r - x_{sp})^2}\right) \tag{2.1}$$

The traveltime T is a function of source and receiver locations x_s and x_r, and it is called the traveltime response of the scatterpoint (x_{sp}, z_{sp}). The geometry of a scatterpoint is shown in Figure 2.1.
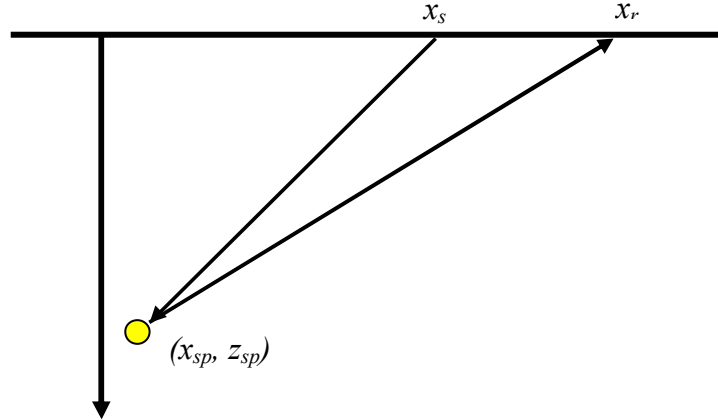
Figure 2.1. Geometry of a scatterpoint model.

The two-way vertical traveltime t_0 is defined by

$$t_0 = \frac{2z_{sp}}{v},$$

(2.2)

which is proportional to the depth z when the velocity is constant, and allows equation (2.1) to be rewritten as

$$T = \sqrt{\frac{t_0^2}{4} + \frac{(x_s - x_{sp})^2}{v^2}} + \sqrt{\frac{t_0^2}{4} + \frac{(x_r - x_{sp})^2}{v^2}} \quad .$$

(2.3)

Subsurface images are expected to be functions of spatial coordinates (x, z), as they ideally represent the reflection coefficients at all subsurface points. Practically, it may be easier to obtain a subsurface image in x-t_0 space than in x-z space. These x-t_0 domain images are called time migration sections. Each point on a time migrated section can be called a scatterpoint, because of its correspondence with the spatial domain scatterpoint. This extension of the scatterpoint concept, from depth to time, is exact when the wave velocity is constant. When velocity varies only with depth $v(z)$, the one-to-one relation between scatterpoint in depth and scatterpoint in time domain still holds, and the velocity can be defined in vertical time $v(t_0)$. Thus equation (2.3) can still approximate the

traveltime response of a scatterpoint with properly defined velocity. The migration velocity for prestack Kirchhoff time migration is approximated by root-mean-squared (RMS) velocity, which is defined in the time domain as

$$v_{rms}^2(t_0) = \frac{1}{t_0} \int_0^{t_0} v^2(\tau') d\tau'. \tag{2.4}$$

Prestack migration based on scatterpoint model

Equation (2.3) is called the double-square-root (DSR) equation. The location of the source x_s, and the receiver x_r are often more conveniently expressed as combinations of midpoint x_{cmp} and half source receiver offset h, where

$$x_{cmp} = \frac{x_s + x_r}{2},$$

and

$$h = \left| \frac{x_s - x_r}{2} \right|.$$

Equation (2.3) may then be written as

$$t = \sqrt{\frac{t_0^2}{4} + \frac{(x_{cmp} - x_{sp} - h)^2}{v_{rms}^2}} + \sqrt{\frac{t_0^2}{4} + \frac{(x_{cmp} - x_{sp} + h)^2}{v_{rms}^2}}, \tag{2.5}$$

When considering only one scatterpoint with many source and receiver locations, it is convenient to define the origin of the x axis at x_{sp}, i.e. $(x_{sp}, 0)$, and use the term x_{cmp} for the x location of common midpoint (CMP), the equation (2.5) can be rewritten as,

$$t = \sqrt{\frac{t_0^2}{4} + \frac{(x_{cmp} - h)^2}{v_{rms}^2}} + \sqrt{\frac{t_0^2}{4} + \frac{(x_{cmp} + h)^2}{v_{rms}^2}}. \tag{2.6}$$

In 3D space (x_{cmp}, h, t), DSR equation describes a surface called Cheops Pyramid (Claerbout, 1985), as shown in Figure 2.2.
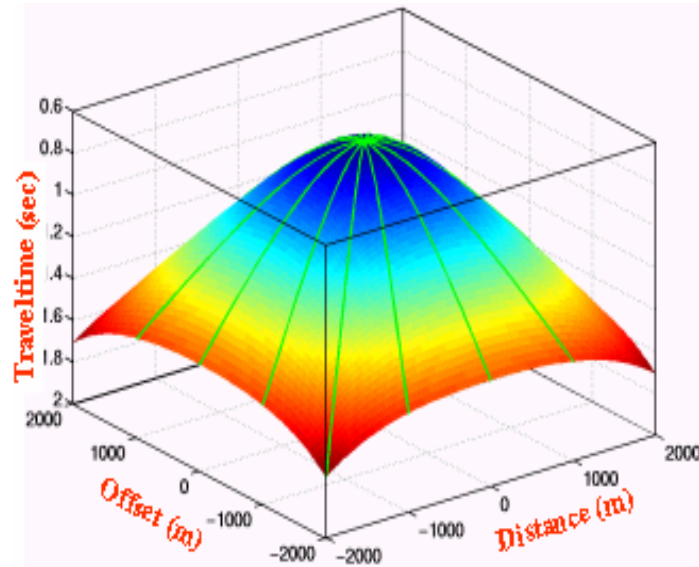
Figure 2.2. Cheops Pyramid described by DSR equation in (x_{cmp}, h,t) domain.

In terms of a Scatterpoint Model, the migration process attempts to collect all the energy scattered from this point as a way to estimate the reflection at this point.

2.2.2 Equivalent Offset Method (EOM)

Prestack Kirchhoff migration is a process that collects all the energy along the surface defined by Cheops Pyramid, and places it at the scatterpoint. The Equivalent Offset Method (EOM) of prestack time migration is also a Kirchhoff migration, but divides the process into two steps, a gather process and a moveout correction process.

Definition of equivalent offset

The DSR equation (2.6) can be rearranged by splitting the time-related term and the space-offset term as

$$t_0^2 = t^2 - \frac{4h^2}{v_{rms}^2} - \frac{4x_{cmp}^2}{v_{rms}^2} + \frac{16x_{cmp}^2 h^2}{v_{rms}^2 (v_{rms} t)^2} , \tag{2.7}$$

and

$$t_0^2 = t^2 - \frac{4}{v_{rms}^2}(h^2 + x_{cmp}^2 - \frac{4x_{cmp}^2 h^2}{v_{rms}^2 t^2}), \qquad (2.8)$$

Then the equivalent offset h_e can be defined as

$$h_e^2 = h^2 + x_{cmp}^2 - \frac{4x_{cmp}^2 h^2}{v_{rms}^2 t^2}, \qquad (2.9)$$

Thus, using equivalent offset, the DSR equation can be expressed simply as

$$t^2 = t_0^2 + \frac{4h_e^2}{v_{rms}^2}. \qquad (2.10)$$

Equation (2.9) defines an equivalent offset for each sample in the prestack seismic data volume relative to the scatterpoint location. The equivalent offset changes with the output scatterpoint location and the related velocity. The equivalent offset can not be smaller than the half source-receiver offset because $v_{rms}t$ can not be smaller than the source-receiver offset.

The equivalent offset has an intuitive geometric explanation. As in Figure 2.3, for source-receiver pair located at x_s and x_r, and a scatterpoint at (x_{sp}, z_{sp}), there is always one surface location, x_e, such that the two-way traveltime from $(x_e, 0)$ to (x_{sp}, z_{sp}) equals the traveltime from $(x_s, 0)$ to (x_{sp}, z_{sp}) then to $(x_r, 0)$. The horizontal distance between the surface location x_e and scatterpoint x_{sp} is the equivalent offset.
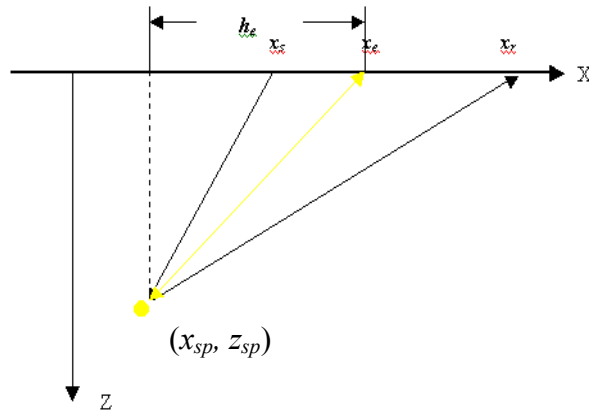
Figure 2.3. Geometric explanation of equivalent offset.

Common Scatterpoint (CSP) gather and EOM

Any seismic trace may contain scattered energy from any scatterpoint in the relevant range. If the energy can be sorted by scatterpoint locations instead of CMP locations, migration related problems should be much easier to solve. The equivalent offset concept, based on the Scatterpoint Model, introduces a convenient method for gathering reflected and scattered energy in the seismic data.

A common scatterpoint (CSP) gather at a certain surface location (called CSP location), is a rearrangement of the seismic energy in equivalent offset and traveltime. In a CSP gather, the energy from those scatterpoints vertically aligned at this CSP location will be gathered, and the Cheops Pyramids corresponding to these scatterpoints will be collapsed to hyperbolas as expressed by equation (2.10). Energy from scatterpoints that are not below the CSP location will also be summed, but the energy will be destructively dispersed with a sum that tends to zero.

CSP gathers can be formed at any surface location from data with arbitrary acquisition geometry. Once the CSP gathers are formed, kinematically only NMO correction and stacking applied on these CSP gathers are left for a full prestack migration. A very important property of CSP gathers, is that they provide a direct method to observe the migration velocity using tools of conventional velocity analysis.

It is important to mention that during the CSP gathering process, no time-shifting is involved. The time-direction energy-moving process for the final migration is left for the NMO correction at each CSP location. This no-time shift property of CSP gathering significantly reduces the velocity dependence in the formation of the CSP gathers.

Amplitude scaling during CSP gathering

As mentioned above, prestack migration collects all the energy along the Cheops Pyramid to the scatterpoint. In general, Kirchhoff type migration methods are referred to as diffraction summation methods. For 2D poststack data the diffractions are hyperbolas,

and for prestack data the diffractions are Cheops Pyramids. The amplitude information along the diffractions is not uniformly distributed.

For 2-D poststack migration, the oblique factor can be approximated as t_0/t. However for 2-D prestack migration the question of how to scale the amplitude during CSP gathering is not obvious and will be evaluated in this thesis.

2.3 True-amplitude migration concept

2.3.1 What is true-amplitude?

Amplitude is the maximum departure of a wave from the average value. In seismic data, the amplitude records the contrast of the acoustic impedance. Reflectivity or reflection coefficient refers to the ratio of the amplitude of the displacement of a reflected wave to that of the incident wave. Thus the true amplitude defined here is the reflectivity, or related to reflectivity. According to Schleicher's (Schleicher, 1993) definition, the true amplitude includes the source wavelet, the transmission loss and the reflection coefficient.

2.3.2 True-amplitude migration

AVO or AVA analysis on unmigrated data is often hindered by the effects of common mid-point smear, incorrectly specified geometrical spreading loss, source/receiver directivity, as well as other factors. It is possible to correct some of these problems by analyzing common-reflection-point gathers after prestack migration, provided that the migration is capable of undoing all the amplitude distortions of wave propagation between sources and the receivers.

A migration method capable of undoing such distortions, and thus producing angle-dependent reflection coefficients at analysis points in a lossless, isotropic, elastic earth is called a "true-amplitude migration".

2.3.3 Principles of true-amplitude migration

Samuel Gray, in 1997, concluded that the true-amplitude migration principles are as described next. The simplest illustration of true-amplitude migration is one where no migration (repositioning of reflection data from an unmigrated section to a migrated section) takes place at all. This happens when earth properties vary in only one direction (depth z), there is only one reflector (at depth z_m), and the incident waves are vertically traveling plane waves. In this trivial 1-D case, no geometrical spreading loss occurs that can complicate the calculation of amplitudes. The wavefield observed at $z=0$ is merely a delayed version of the incident waveform, multiplied by the normal-incidence reflection coefficient:

$$P(z = 0) = delay \cdot R(z_m) \cdot W(z = z_m), \tag{2.11}$$

where P is the observed wavefield, R is the reflection coefficient, and $W(z_m)$ is the incident wavefield immediately above the reflector. Equation (2.11) is written as a product in the frequency domain. However in the time domain, the products become convolutions.

Removing the delay is the same as moving the observation depth to z_m:

$$P(z = z_m) = R(z_m) \cdot W(z = z_m), \tag{2.12}$$

and the reflection coefficient R can be found by division. If we wish to find normal-incidence reflection coefficients for reflectors beneath the shallowest one at depth z_m, we need to begin accounting for transmission coefficients as the wavefield passes through the shallow reflectors on its way to and from the deep reflectors. We should also account for multiple reflections, but recall that our primaries only model permits us to ignore the multiples in processing the actual seismic data.

The situation becomes slightly more complicated if the incident plane wave is not normally incident on the reflector. Now we can invert equation (2.11) for $R(z_m, \theta)$, where θ is the incidence angle of the plane wave on the reflector. Again, the incident and reflected plane waves undergo no geometrical spreading loss, so that amplitude

preservation is trivial above the shallowest reflector. For deeper reflectors, we must begin to consider not only the transmission coefficients, but also Snell's law, which changes the direction of the plane wave as it passes through a velocity discontinuity encountered at a reflector. As long as θ remains less than the critical angle at a given reflector, we can continue to find the reflection coefficient for deeper reflectors.

We can gradually add complications that force us to refine our expression to be inverted. For example, 2-D allows lateral variations of both propagation velocity and reflector structure, but the incident wavefield is a cylindrical wave from a line source in three dimensions; 2.5-D is the same as 2-D except that the incident wave is a spherical wave. For all these cases, the fundamental problem is the same, namely to deduce an expression for the angle-dependent reflection coefficient at an image point from the expression for the observed wavefield at the receiver locations.

In this thesis, only the 2-D case was studied and actually, for geometrical spreading factor, in this sense, it is 2.5-D. Since nearly all the geometrical spreading correction is done before migration, in this thesis, it is not considered.

2.3.4 Assumptions in true-amplitude migration

Geophysicists realize that to perform a true-amplitude migration according to wave equation solutions, there should be always such assumptions as:
1. The earth is lossless, isotropic and elastic.
2. The convolutional model of the source wavelet and reflectivity.
3. High frequency and stationary phase.
4. Multiples are neglected.

2.4 Limited aperture migration approach

Since the work of Newman (1975), attempts have been made to incorporate amplitude in diffraction stack seismic migration schemes. Recently, Sun (1996)

developed different weight functions for limited aperture Kirchhoff migration (LAM). In the next part, it will be introduced.

Sun (1996) first published his works on true-amplitude migration or limited aperture true-amplitude migration for the 2-D case.

For the 2-D case, sources and receivers are distributed along a single line. In this instance, since no information in the direction orthogonal to the exploration line is available, it is assumed that the subsurface is homogeneous in the orthogonal direction. As a consequence of this assumption, one is forced to use a 2-D model of wave motion for processing the data recorded along the exploration line. If this 2-D model is used in Kirchhoff-type migration, the recorded data will be diffraction-stacked over a given interval called migration aperture. Yilmaz (1987) shows that both the excessively large and the excessively small migration aperture lead to a poor migrated image. Here, only his weight function for diffraction stack is introduced.

Structure of the migration image

Let $O(P,t)$ denote the time-dependent migrated image at the subsurface point P, $O(P,t)$ can be written as (Bleistein et al., 1987)

$$O(P,t) = \int_{-\xi_a}^{\xi_b} Q(\xi)W(P,\xi)F^{-1}[D(\xi,\omega)]d\xi ,$$ (2.13)

with

$$D(\xi,\omega) = \sqrt{i\omega}U(\xi,\omega)\exp(-i\Phi_W)\exp[i\omega t_D(\xi)].$$ (2.14)

Here, ω is the angular frequency, ξ is the parameter describing any source-receiver configuration (Bleistein et al., 1987), where ξ_a and ξ_b are positive numbers that define the migration aperture [$-\xi_a$, ξ_b], $Q(\xi)$ is the differential arc element that takes the curvature of the recording line into account, $W(P, \xi)$ is a real weight function, $U(\xi, \omega)$ is the spectrum of the input seismic data, $\exp(-i\Phi_W)$ denotes the filter operator that compensates the phase shift caused by caustics during wave propagation from the source point to receiver

point, $t_D(\xi) = t_D[\mathbf{r}_s(\xi), \mathbf{r}_g(\xi)]$ denotes the traveltime of point-diffracted rays, and $D(\xi, \omega)$ is the input seismic data free from the phase shift caused by propagation and from the filtering effect caused by diffraction stack.

Note that the time-dependent migrated image $O(P, t)$ can be displayed in the time as well as in the depth domain (Schleicher et al., 1993). In the time domain (time migration), $O(P, t)$ gives the reconstructed wavefield. In the depth domain (depth migration), $O(P, t)$ leads to the depth-migrated image $O(P, t=0)$.

Using the Fourier transform together with $U(\xi, \omega) = A_{sg}(\xi) \exp[-i\omega t_r(\xi)]$, according to the ray theory, the migrated image $O(P, t)$ given by equation (2.13) can be transformed into

$$O(P, \omega) = \sqrt{i\omega} J \, , \qquad (2.15)$$

with

$$J = \int_{-\xi_a}^{\xi_b} E(\xi) \exp[i\omega\tau(\xi)] d\xi \, , \qquad (2.16)$$

and

$$E(\xi) = Q(\xi) W(P, \xi) A_{sg}(\xi) \exp(-i\Phi_W) \, . \qquad (2.17)$$

In the above two equations, $\tau(\xi) = t_D(\xi) - t_r(\xi)$ where $t_r(\xi)$ denotes the traveltime of reflected rays, and $A_{sg}(\xi)$ is the ray amplitude factor of the seismic wavefield, i.e.,

$$A_{sg}(\xi) = \frac{\exp(i\Phi_C)}{\Re(\xi)} C_R \wp S(\omega) \, . \qquad (2.18)$$

where Φ_C denotes the phase shift caused by caustics, $\Re(\xi)$ denotes the non-negative normalized geometrical spreading factor, C_R is the plane-wave reflection coefficient, the factor $\wp$ describes the transmission losses and angle dependence during propagation and source excitation, and $S(\omega)$ denotes the spectrum of the source wavelet.

In general, equation (2.17) can only be evaluated asymptotically by using the method of stationary phase. For convenience, assume that only one stationary point exists. Since

in practice any portion of the ξ-axis may be chosen as the migration aperture, the stationary point may lie inside or outside of the migration aperture. The distance between ξ_s and the two endpoints may be large, small, or zero. If ξ_s is in the migration aperture, the stationary point is an isolated interior one. In this case, the contributions from ξ_s, $-\xi_a$ and ξ_b can be considered separately. If ξ_s lies near any of the two endpoints, the contribution from ξ_s and that from the endpoint have to be considered together because in this case, the stationary point is no longer isolated. If the migration aperture is large enough, the endpoint effect can be eliminated by the taper or another weight function.

The following will study the cases abovementioned separately. For convenience, the coordinate system originates from the surface location of the stationary point or reflection point ξ_S, i.e., $\xi_S=0$ and let the ξ-axis of the coordinate system be tangent to the earth's surface at the point ξ_S. Also assuming that near ξ_S the earth's surface can be written as $z=z(\xi)$. Thus, in a small subaperture containing ξ_S, $Q(\xi) = \sqrt{1 + z'^2(\xi)}$ where the prime denotes the first derivative with respect to ξ.

Interior stationary point

If ξ_S is an isolated interior stationary point, the migration aperture $[-\xi_a, \xi_b]$ can be divided into three subapertures. The first subaperture is the central part of the migration aperture defined by $[-\xi_c, \xi_c]$ where ξ_c is a positive number smaller than ξ_a and ξ_b. The others are the intervals $[-\xi_a, -\xi_c]$ and $[\xi_c, \xi_b]$.

In the central part of the migration aperture, $E(\xi) \approx E(\xi_s) + E'(\xi_s)\xi$ and $\tau(\xi) = t_D(\xi) - t_r(\xi) \approx \tau''(\xi_s)\xi^2 / 2$ because at ξ_s the traveltime curves of point-diffracted and reflected rays are tangent to each other. The primes denote the derivatives with respect to ξ.

Thus, equation (2.16) reduces to

$$J_c = G(\xi_s) \int_{-\xi_c}^{\xi_c} \exp[i\omega \frac{\tau''(\xi_s)}{2} \xi^2] d\xi, \tag{2.19}$$

because $E'(\xi_s) \, \xi$ gives a zero contribution to J_c. Here, the subscript c labels the central part of the migration aperture, and $G(\xi) = E(\xi)\exp[i\omega\tau(\xi)]$. Note that $G(\xi_s) = E(\xi_s) = W(P, \xi_s) A_{sg}(\xi_s)\exp(-i\Phi_W)$ because $\tau(\xi_s) = 0$ and $Q(\xi_s) = 1$.

Following equation (2.19), it can be determined that:

$$J_c = \frac{2\sqrt{2} G(\xi_s)}{|\omega\tau''(\xi_s)|^{\frac{1}{2}}} \left[\frac{\sqrt{\pi}}{2} \exp(i\sigma\frac{\pi}{4}) - F_\sigma(\eta) \right], \tag{2.20}$$

where $\sigma = \mathrm{sgn}[\omega\tau''(\xi_s)]$, $\eta = \xi_c \sqrt{|\omega\tau''(\xi_s)|/2}$, and $F_\sigma(y) = F_+(y)$ if $\sigma > 0$ and $F_\sigma(y) = F_-(y)$ otherwise. Here, $F_\pm(y)$ is defined by

$$F_\pm(y) = \int_y^\infty \exp(\pm ix^2) dx, \tag{2.21}$$

Further, by developing equation (2.20) the relation

$$F_\pm(0) = \frac{\sqrt{\pi}}{2} \exp(\pm i\frac{\pi}{4}). \tag{2.22}$$

was used. In equation (2.20) the first term is the migrated image when the migration aperture is infinitely large, and the second term describes the boundary effect from $\pm\xi_c$. Note also, that η stands for the normalized size of the central part of the migration aperture.

Investigate the contribution from the other two parts of the migration aperture. Since in these two intervals no stationary point exists, the diffraction stack can be evaluated by integrating by parts. Let J_a and J_b denote the contribution from $[-\xi_a, -\xi_c]$ and $[\xi_c, \xi_b]$, then

$$J_a = -\frac{1}{i\omega} \left[\frac{G(-\xi_a)}{\tau'(-\xi_a)} + \frac{G(-\xi_c)}{\tau''(\xi_s)\xi_c} \right], \tag{2.23}$$

and

$$J_b = \frac{1}{i\omega}\left[\frac{G(\xi_b)}{\tau'(\xi_a)} - \frac{G(\xi_c)}{\tau''(\xi_s)\xi_c}\right]. \tag{2.24}$$

If $\eta \geq 3$, $F_\sigma(\eta)$ can be approximated by the first term of its asymptotic expansion $F_\sigma(\eta) \approx \exp[i\sigma(\eta^2 + \frac{\pi}{2})]/2\eta$. Using $\eta = \xi_c\sqrt{|\omega\tau''(\xi_s)|/2}$ in this equation yields

$$F_\sigma(\eta) \approx -\frac{\sigma}{i\xi_c|2\omega\tau''(\xi_s)|^{\frac{1}{2}}}\exp\left[i\omega\frac{\tau''(\xi_s)}{2}\xi_c^2\right]. \tag{2.25}$$

Inserting it into equation (2.20) gets

$$J_c \approx J_s + \frac{2G(\xi_s)}{i\omega\tau''(\xi_s)\xi_c}\exp\left[i\omega\frac{\tau''(\xi_s)}{2}\xi_c^2\right], \tag{2.26}$$

with

$$J_s = \frac{\sqrt{2\pi}}{|\omega\tau''(\xi_s)|^{\frac{1}{2}}}G(\xi_s)\exp(i\sigma\frac{\pi}{4}), \tag{2.27}$$

where the subscript s labels the contribution from the stationary point.

By constructing $J_c+J_a+J_b$ under the conditions that $E(\xi) \approx E(\xi_s) + E'(\xi_s)\xi$ and $\tau(\xi) \approx \tau''(\xi_s)\xi^2/2$, it is obtained that $J=J_s+J_e$ where J_s is given in the above equation and

$$J_e = \frac{1}{i\omega}\left[\frac{G(\xi_b)}{\tau'(\xi_b)} - \frac{G(-\xi_a)}{\tau''(-\xi_a)}\right]. \tag{2.28}$$

Here, the index e labels the contribution from the endpoints of the migration aperture.

In summary, the migrated image produced by a 2-D LAM operator consists of three components. One is the contribution from the stationary point; the others are from the endpoints of the migration aperture. Furthermore, the contribution of the stationary point is independent of the size of the migration aperture as long as the stationary point lies well within the migration aperture, whereas the contributions from the two endpoints are aperture dependent. If the stationary point lies outside of the migration aperture and far away from the two endpoints, the migrated image comes solely from the two endpoints.

Physically, the contribution of the stationary point is the migration signal because from this contribution, one can compute the migrated image with true amplitude defined in Schleicher et al. (1993). In contrast, the contributions from the two endpoints are migration noise because these contributions produce diffraction-like events.

Weight functions

The weight function mentioned here can be obtained by using J_s given in equation (2.26) under the condition that corresponding migrated image $O_s(P,\omega) = \sqrt{i\omega} J_s$ gives the true-amplitude reflection, i.e.,

$$O_s(P,\omega) = U_{TA}(\xi,\omega) = C_R A_{sg} S(\omega),\qquad(2.29)$$

where the subscript *TA* indicates the true-amplitude reflection.

To obtain the true-amplitude reflection defined in the above equation, the boundary effect described by equation (2.27) must be removed. This is possible, if only the weight function vanishes at the endpoints. Thus $W(P,\xi)$ has to be a product of two functions, i.e., $W(P,\xi) = W_1(P,\xi) W_2(P,\xi)$ where W_1 should guarantee the true-amplitude reconstruction and W_2 should remove the boundary effects.

Using equation (2.17) and (2.27) together with equation (2.18), the weight function can be derived as

$$W_1(P,\xi) = \Re_{sg}(\xi) \left| \frac{\tau''(\xi)}{2\pi} \right|^{\frac{1}{2}},\qquad(2.30)$$

and phase shift

$$\Phi_W = \Phi_C + \operatorname{sgn}(\omega)\frac{\pi}{4} + \operatorname{sgn}[\omega\tau''(\xi)]\frac{\pi}{4}.\qquad(2.31)$$

The other weight function W_2 is only for eliminating the boundary effect of the migration aperture, so it should be continuous and within the defined optimum aperture, and it should be unity. Actually, it acts like a window function. It is not important which

window or taper function is in use, and in the next Chapter, it will be proven that for a CSP-gather, there is no effect if the migration aperture is defined properly.

Sun also investigated the two cases of no stationary point in the aperture and stationary point near one end of the aperture. In this thesis, only the first condition is of concern because if the tangent point is located, then migration can be viewed as in the first case.

However, finding the tangent point is still a problem for geophysicists. One practical method is to migrate the data several times and then to find the tangent point location for the target. Nevertheless, for the layered model with the RMS velocity assumption, the tangent point is always in the center of the aperture. But for a dipping event, the larger the dip, the larger the distance between the tangent point and the scatter point of the surface.

In Sun's work, he also derived the aperture size with the time difference between the diffraction and reflection. However, it comes back to the tangent point again as the reflection time is unknown. In Chapter 3 of this thesis, the aperture size is related to the Fresnel zone concept, and it is easier to calculate using two-way vertical travel time compared to Sun's definition.

It also should be mentioned that Sun's aperture definition includes taper size, also in the next Chapter, as long as the migration aperture is large enough, the taper function is just used to eliminate the migration artifacts, so it should not be considered part of the migration aperture definition.

2.5 Chapter conclusions

In this Chapter, first the EOM migration algorithm was introduced. Compared to traditional Kirchhoff migration algorithms, EOM has several advantages:
1. It is fast;
2. It provides a middle step to re-evaluated velocities.

3. It is naturally anti-aliasing.

4. It is not as sensitive to input velocity as other methods.

The concept of true-amplitude migration was discussed. True-amplitude migration is used as AVO/AVA analysis after prestack migration, and the concept is useful to determine the scaling factors or weighting functions used in EOM. Finally, Sun's approach to limited migration aperture concept was introduced.

Chapter 3

The minimum migration aperture

3.1 Chapter summary

Webster's dictionary defines the term "aperture" in its usage in optics as " the diameter of the stop in an optical system that determines the diameter of the bundle of rays traversing the instrument". In seismic processing, aperture is defined as the spatial range of the data considered in a calculation (Bleistain, 1987). A Kirchhoff-type migration with a finitely large migration aperture is called limited aperture migration (Sun, 1998). In comparison with its infinitely large aperture counterpart, a limited aperture migration gives a migrated image that depends on both the size and the location of the migration aperture.

In the previous Chapter, some limited aperture migration methods and EOM were introduced. In this Chapter the size of migration aperture and the effect of taper size will be discussed, and the minimum migration aperture will be derived. The synthetic data examples show that the minimum migration aperture should be the size of the Fresnel zone.

3.2 The Fresnel zone concept

Geophysicists commonly recognize that a sizeable portion of a reflector is involved in causing a reflection, as seen on a seismic trace, however the area extent is usually not calculated and hence not appreciated. These concepts are simply transferred from classical physical optics referred to as the Fresnel zone effects. The first Fresnel zone is

that portion of a reflector from which reflected energy can reach a detector within the first one-half wavelength of the reflection; contributions from this zone add constructively to produce a reflection. There is a second Fresnel zone from which energy arrives, delayed one-half to one cycle, adding destructively to the energy from the first zone. Similarly, there is a third zone, which adds constructively, and so on. When the contributions of all zones are added together, a reflection from a plane reflector is one-half of the response of the first Fresnel zone, the effects of all subsequent zones cancelling each other, and the adjective 'first' is often dropped (Sheriff, 1980).

Attention to the Fresnel zone has increased as more efforts are devoted to improving the seismic resolution. Fresnel zone considerations are the essence of horizontal resolution. Attention has also been increasing because of a greater awareness of three-dimensional effects. Hagedoorn (1954) points out that the vertical resolution can also be thought of as a Fresnel-zone problem.

The geometry for calculating the radius of the first Fresnel zone is shown in Figure 3.1 for coincident source and receiver and constant velocity using the Pythagorean theorem,

$$(z + \lambda/4)^2 = z^2 + R^2, \tag{3.1}$$

where z is the reflector depth, λ the wavelength, and R the radius of the Fresnel zone. Solving for R gives,

$$R = (\lambda z/2 + \lambda^2/16)^{\frac{1}{2}} \approx \sqrt{\lambda z/2} \approx \sqrt{vz/2f}, \tag{3.2}$$

with the λ^2 term usually being small enough to be neglected. This can also be expressed in terms of two-way vertical travel time t_0, velocity v, and wavelet period τ using the familiar relationships $z = vt_0/2$ and $\lambda = v\tau$, thus gives (Sheriff, 1980)

$$R = (v/2)\sqrt{t_0\tau}. \tag{3.3}$$
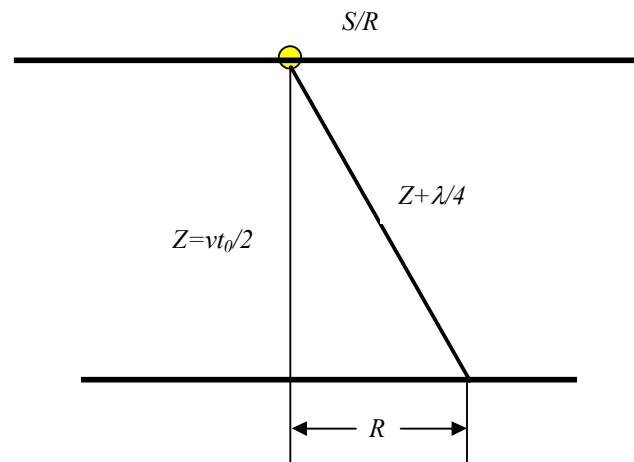
Figure 3.1. Geometry for calculating radius of Fresnel zone.

For example, if the subsurface has a constant velocity, the Fresnel zone varies with frequency and depth, as shown in Figure 3.2. With linear velocity, which can be found at a classic tertiary sedimentary basin, the Fresnel zone size varies with depth and frequency as shown in Figure 3.3.

(a)   (b)
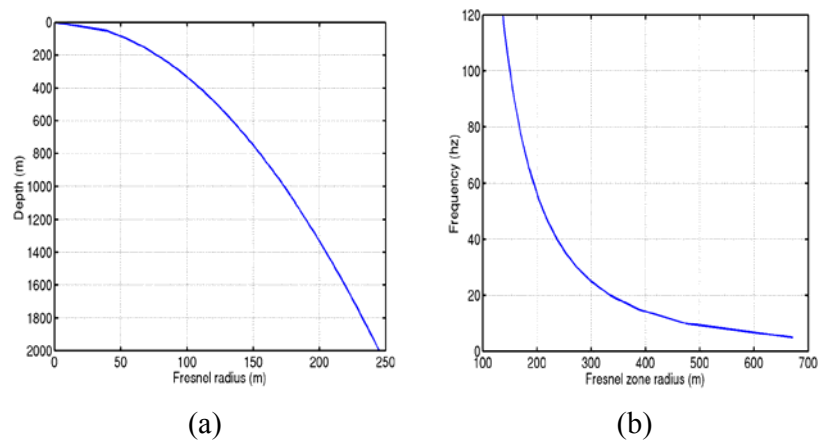
Figure 3.2. The Radius of the Fresnel zone varies with depth and frequency with constant velocity v=3000m/s. (a) the radius of the Fresnel zone varies with depth at frequency 50hz; (b) the radius of the Fresnel zone varies with frequency at depth 1500m.
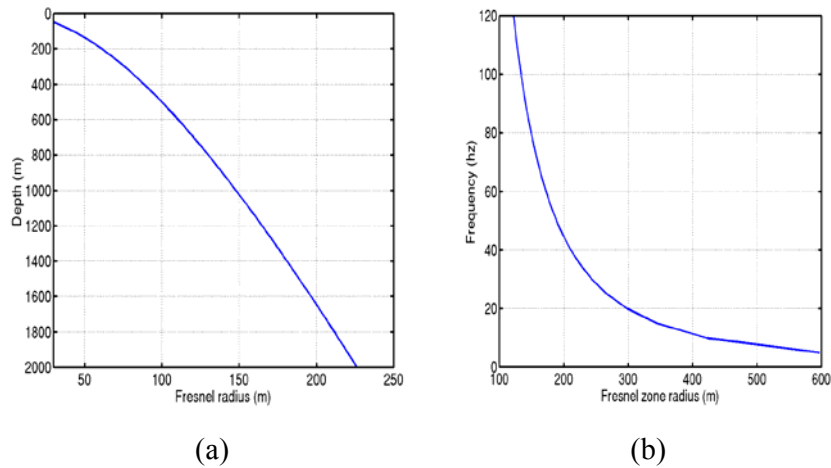
Figure 3.3. The radius of the Fresnel zone varies with depth and frequency with linear velocity v=1800+0.8z. (a) the radius of the Fresnel zone varies with depth at frequency 50hz; (b) the radius of the Fresnel zone varies with frequency at depth 1500m.

3.3 The Fresnel zone and source type

The Fresnel zone effect described above is observed in optics using monochromatic light shining through holes of different sizes. But in seismology the source type is called a broadband wavelet. In the next section, the Fresnel zone will be discussed as it relates to source type.

To investigate the relationships between the Fresnel zone and the source type, the easiest horizontal circular reflector and zero-offset data are used as Figure 3.4 shows. The calculation was done in the time domain using the methods of Trorey (1970):

$$R(t) = \frac{1}{T_0} f(t - T_0) - \frac{z}{T\xi} f(t - T), \qquad (3.4)$$

where $R(t)$ is the reflected signal, $f(t)$ is the source wavelet which includes the reflection coefficient, z is the depth of the reflector, T_0 is two-way normal-incidence time to reflector, ξ is the distance from source to the edge of the reflector and T is two-way travel time to the edge of the reflector. From equation (3.4), the first term is the desired reflection, the source wavelet retarded by the time T_0, the second term is the

polarity reversed source wavelet with retardation *T*, and from the edge of the reflector corresponding with a truncation effect caused by the finite integration area. For a reflector with infinite radius, ξ tends to infinity, then the truncation term vanishes, and $R(t)$ is exactly equal to the desired reflection.
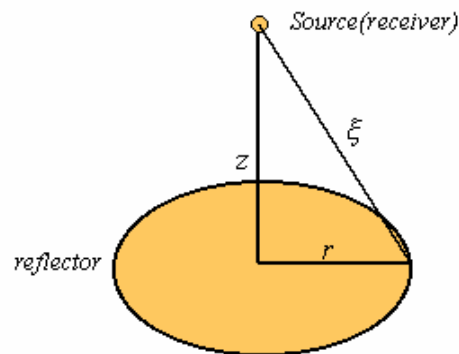
Figure 3.4. Easiest horizontal circular reflector example.

3.3.1 Monochromatic wavelet source

Using equation (3.4) the energy of the reflected signal at the source location as a function of the reflector radius can be computed. For a monochromatic source, i.e. a sinusoid function, the reflected energy relates to reflector size is shown in Figure 3.5.
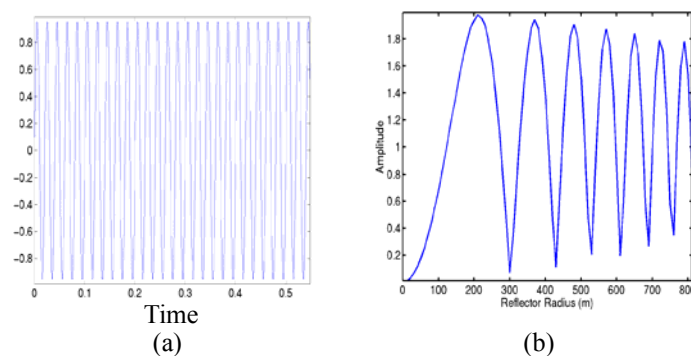
Figure 3.5. Sinusoid source function and reflected energy. (a) The sinusoid source function; (b) The reflected energy with the reflector radius.

For a monochromatic signal, such as Figure 3.5a, the energy is oscillating. The first

maximum of the curve defines the boundary of the radius of the first Fresnel zone, the other extreme corresponds to the boundaries of the higher order radius of the Fresnel zones.

3.3.2 Ricker wavelet source

The Ricker wavelet to be used here is defined in (Sheriff, 1995) as

$$f(t) = (1 - 2\pi^2 \upsilon^2 t^2) e^{-\pi^2 \upsilon^2 t^2} . \tag{3.5}$$

where υ is the dominant frequency and t is time. For this kind of source wavelet, the reflected energy is shown in Figure 3.6.
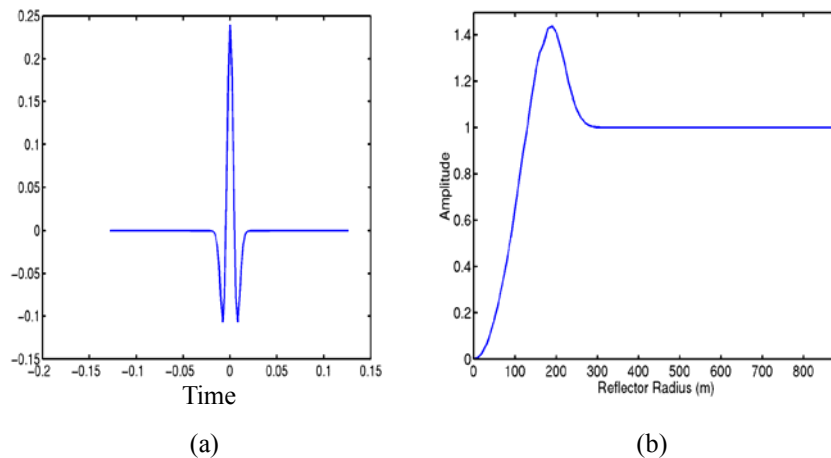
Figure 3.6. Ricker source wavelet and reflected energy. (a) Ricker source wavelet; (b) Reflected energy with reflector radius.

The reflection energy with the Ricker source wavelet builds up to a maximum as it does also for the other signals, but it quickly stabilizes to a constant value.

3.3.3 Delta function source

With a band limited Delta source function, the energy shows some oscillation as Figure 3.7 shows. With a different frequency band, the radius of the Fresnel zone,

which is the area when the energy reaches its maximum, varies with the bandwidth. The more broad the frequency slope is, the smaller the size of the radius of the Fresnel zone is.

| | (a) | | (b) |
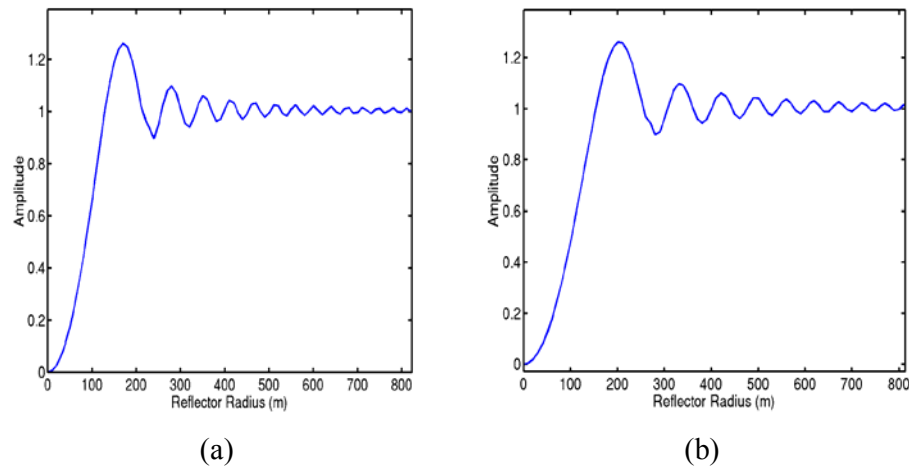
Figure 3.7. Reflected energy relates to reflector radius with Delta source. (a) Frequency is 0-150hz; (b) Frequency is 0-120hz.

In summary, the radius of the Fresnel zone for a broadband source wavelet is defined by the radius when the reflected energy reaches its maximum. The ringing of the amplitude is a result of the sharp truncation of the frequency bandwidth, and is reduced when there is more natural taper as shown in Figure 3.6. Restricting the reflector radius to smaller than the radius of the Fresnel zone will result in a change of the reflected wavelet with respect to the input wavelet. The figures of reflected energy show that for removing the truncation effect (second term in equation 3.4) or edge effect, the reflector radius should be larger than the radius of the Fresnel zone, and be at some point where the energy becomes stable. In the next section I will show that by using diffraction theory, for true amplitude modelling of the Fresnel zone effect, i.e., the edge effect must be considered.

3.4 Amplitude variation within the Fresnel zone in the zero-offset case

To investigate the relationship between the Fresnel zone and the reflection strength, the easiest model, i.e., zero-offset 2D case data, is used. According to the diffraction theory (Berryhill, 1977), the diffraction amplitude at zero source-receiver offset due to the termination of a planar reflector, can be calculated by convolving the reflection wavelet with a time-domain operator called the normalized diffraction response. The diffraction response at zero-offset can be written in the forms

$$p_n(t) = f(t) * D_0(t)U(t - t_e),$$
(3.6)

and

$$D_0(t') = \frac{\cos\theta_0}{\pi} \frac{t_e^2}{(t'+t_e)^2} \frac{d}{dt'}[\arctan(\sqrt{t'(t'+2t_e)}/(t_e\sin\theta_0))].$$
(3.7)

in which

t_e, minimum two-way travel time to the edge of the reflector;

$t'=t-t_e$, time measured after onset time t_e ;

θ_0, the angle between the normal to the reflector and raypath of the minimum travel time to the edge of the reflector;

$f(t)$, source wavelet function;

$U(t-t_e)$, unit step function to maintain zero value prior to t_e.

3.4.1 D_0 operator

Using equation (3.7) the D_0 operator calculation requires knowledge of only two parameters, t_e and θ_0. In practical applications, D_0 is evaluated numerically with t' taking values which are multiples of some discrete time sample interval. The derivative term in equation (3.7) then becomes a difference, and the result is suitable for digital convolution with a seismic wavelet. Figure 3.8 presents the results of evaluating D_0 at one value of $t_e=1.0$ for four different choices of θ_0.
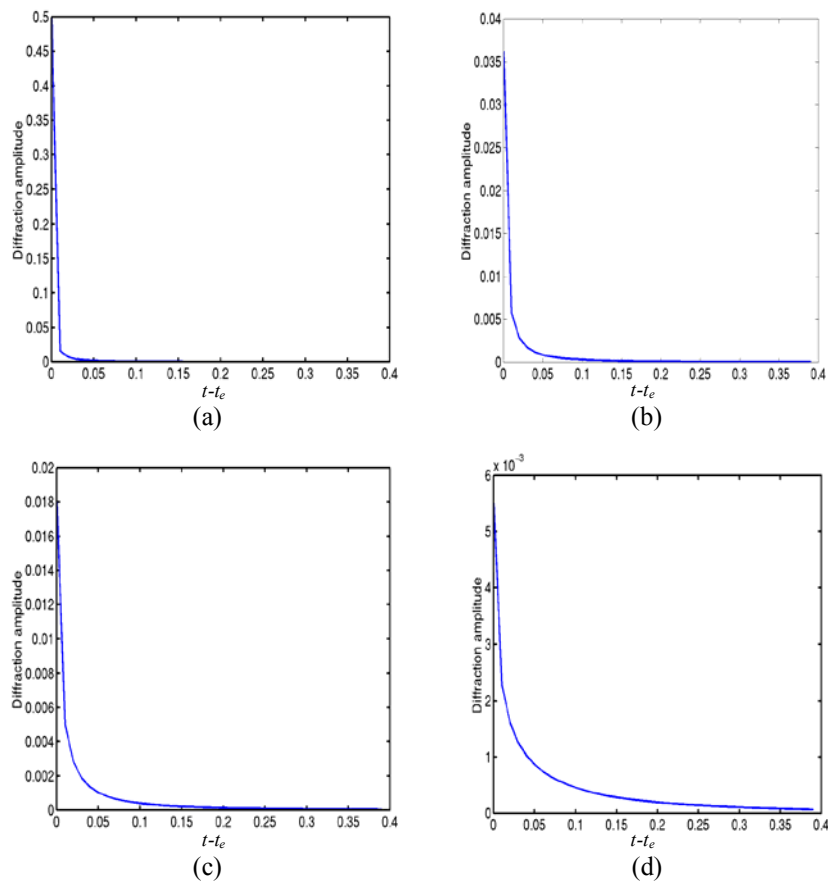
Figure 3.8. D_0 operator with same $t_e=1.0$ but different θ_0. (a) $\theta_0=0^0$; (b) $\theta_0=5^0$; (c) $\theta_0=10^0$; (d) $\theta_0=30^0$.

When θ_0 is 0 degrees, D_0 is a one-sample spike with a magnitude equal to exactly one-half. Convolving this with any wavelet simply reproduces the wavelet with one-half its original amplitude. As θ_0 increases, i.e. the reflector increases, and as the distance increases from the source to the edge of the reflector, the height of the initial peak decreases quickly. In other words, when the reflector reaches its certain size, the effect from the reflector edge can be ignored.

3.4.2 2-D Reflector Model

In 1970, Trorey created a 2D model that considered the diffraction at the edge of

the reflector, and I refer to it in this thesis as the edge effect. V is the reflection and D_1 and D_2 are diffractions from each edge. The total response, i.e. reflection together with diffraction D, was convolved with a Ricker wavelet. There are three typical cases, which need to be investigated:

1. The reflector size is smaller than the Fresnel zone;
2. The reflector size is equal to the Fresnel zone;
3. The reflector size is larger than the Fresnel zone.

The model used will be a reflector at a depth of *1500m* in a medium with velocity *3000m/s*. A *50hz* Ricker wavelet was convolved with the response D. After convolution the amplitude corresponding to the reflection coefficient changed its value to *0.024*.
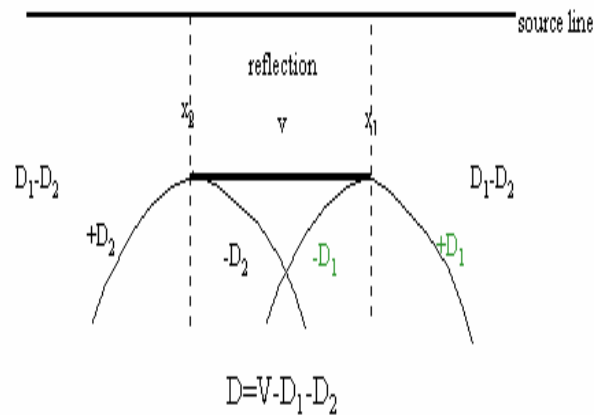
Figure 3.9. 2D model created by Trorey (1970).

Investigation of the amplitude response has a practical use when imaging the subsurface. Migration should eliminate the diffraction. Therefore recognition of the response near the edge of the reflector is important when designing the aperture size in a limited aperture migration.

3.4.3 Reflector size is smaller than the Fresnel zone

The edge effect is greatest on the amplitude when the reflector is smaller than the Fresnel zone as shown in Figure 3.9. Consider a reflector that is *100m* long and located from *2400* to *2500m* in the surface coordinates *x*. The reflected and diffracted responses of the reflector with zero-offset are displayed in Figure 3.10, assuming the sources and receivers are along the surface.
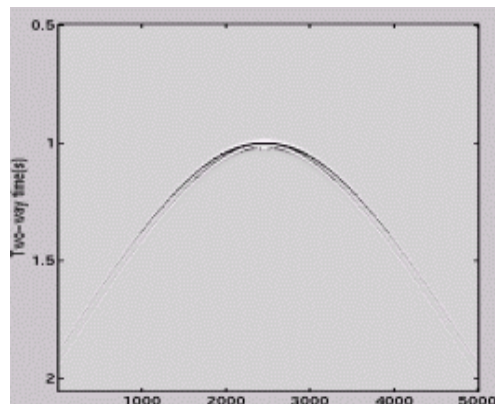
Figure 3.10. Reflected and diffracted responses of a reflector smaller than the Fresnel zone.

It is hard to tell if it is a diffraction point or a reflector. Thus, when the reflector is smaller than the Fresnel zone, the lateral resolution is obscured. Not only is the response smeared, but the amplitude of the response is neither reflection nor diffraction. Figure 3.11 displays the amplitude response.
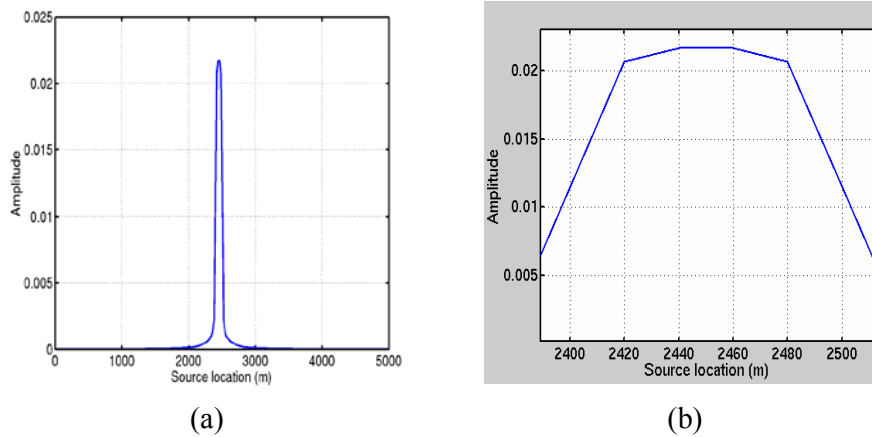
Figure 3.11. The amplitude response of a reflector smaller than the Fresnel zone.
(a)amplitude in total; (b) zoomed section.

3.4.4 Reflector size is equal to the Fresnel zone

When the length of the reflector equals the Fresnel zone, we can obtain an image as Figure 3.12 that shows a better spatial resolution.
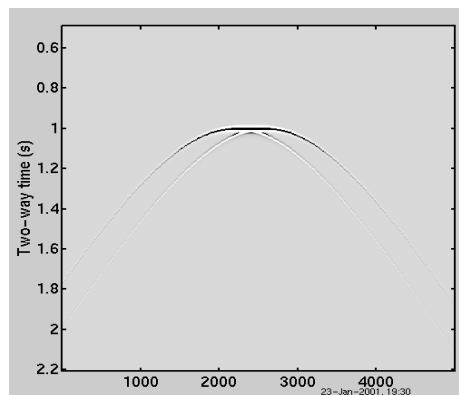
Figure 3.12. Reflected and diffraction response of a reflector whose size is equal to the Fresnel zone.

The effect of the diffraction on the reflection can be seen as the amplitude reaches its maximum in the middle of the reflector, which is the furthest point from the edge. The maximum amplitude at this point is the result of diffraction constructively contributing to the reflection, and it is greater than the reflection effect. Also the

response that is closer to the reflector edges is decreased, as in the above case, with the result is that the diffraction destructively contributes to reflection. Figure 3.13 displays this in detail.

(a)   (b)
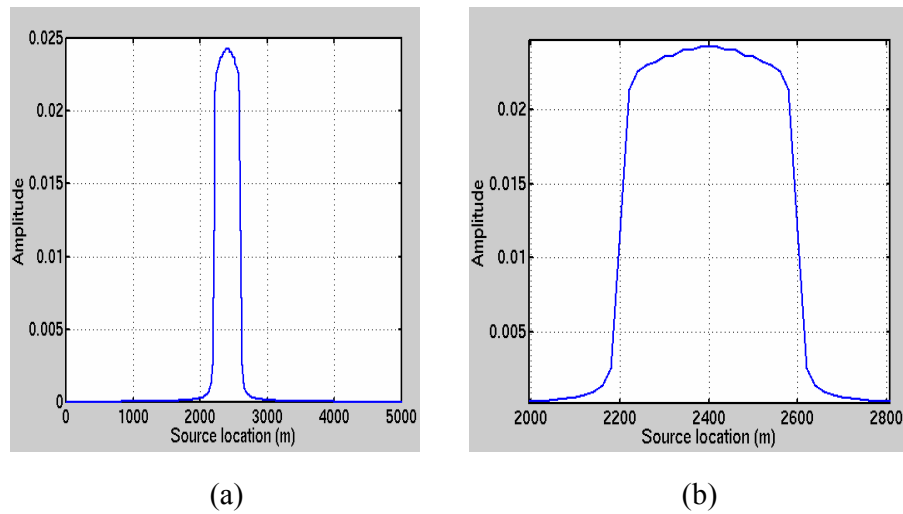
Figure 3.13. The amplitude response of a reflector equal to the Fresnel zone.

(a) whole view; (b) zoomed view.

3.4.5 Reflector size is larger than the Fresnel zone

In most cases, the reflector in the subsurface is larger than the Fresnel zone, but still the diffraction exists at the edge of the reflector.
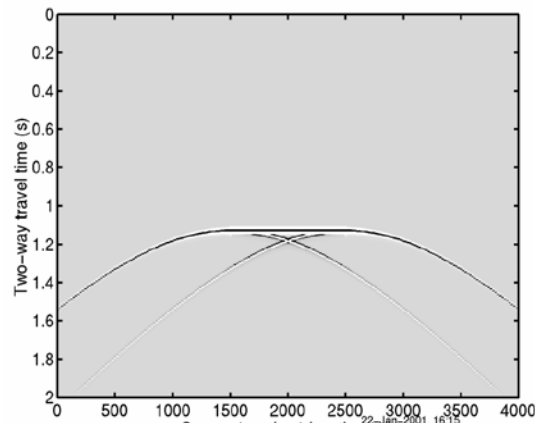
Figure 3.14. Response of a reflector larger than the Fresnel zone.

From the amplitude response in Figure 3.15, the diffraction constructively contributes to reflection when the reflection point is at a distance equal to the radius of the Fresnel zone from the edge. Nearer amplitude is smaller than reflection. When the distance between the reflection points and reflector edge is greater than the radius of the Fresnel zone, the amplitude response of the diffraction has a negligible effect, thus the amplitude is at the reflection strength.

(a)   (b)
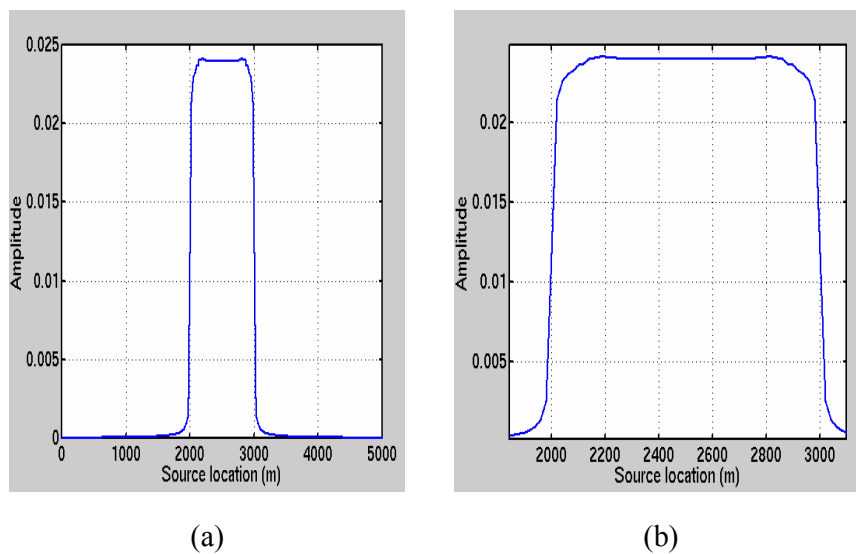
Figure 3.15. Amplitude response of a reflector larger than the Fresnel zone. (a) the whole view; (b) zoomed view.

3.5 Using the Diffraction theory explains the Fresnel zone

It is well known that the diffraction is the theoretical base for a diffraction stack or Kirchhoff-type migration. Generally migration is used for three purposes:

1. Repositioning subsurface reflections to their reflector location;

2. Improving horizontal resolution, which is also referred to as shrinking the Fresnel zone phenomena;

3. Repositioning the diffraction energy to the edge of the reflector.

Recently, as mentioned above, migration is also used for true-amplitude recovery to enable AVO analysis in the correct subsurface position. However, no matter what purpose the migration, there are two issues that must be considered:

1. Migration aperture;
2. Amplitude weighting function on the diffraction.

When the subsurface reflector ends at the edge, the diffraction will be the coherent noise of the data even after stack. Thus the migration aperture in a sense needs to be large enough to focus the diffractions energy. Consequently geophysicists investigate the relationship between the diffraction and the migration aperture. It is therefore important to view the diffraction using the Fresnel zone concept, and to recognize that the Fresnel zone be used to define the minimum migration aperture.

3.5.1 Horizontal reflector

The model used here is the horizontal reflector with a gap. The size of the gap reflected in the seismic section relates the Fresnel zone size. That means, if the gap is smaller than the radius of the Fresnel zone, then it is difficult to distinguish in the seismic section before migration. In the next several pictures, this relationship is presented. As with the previous section, the depth of the reflector used to test is *1500m* and velocity is *3000m/s*, convolved with a Ricker wavelet with wavelength *0.034s*.
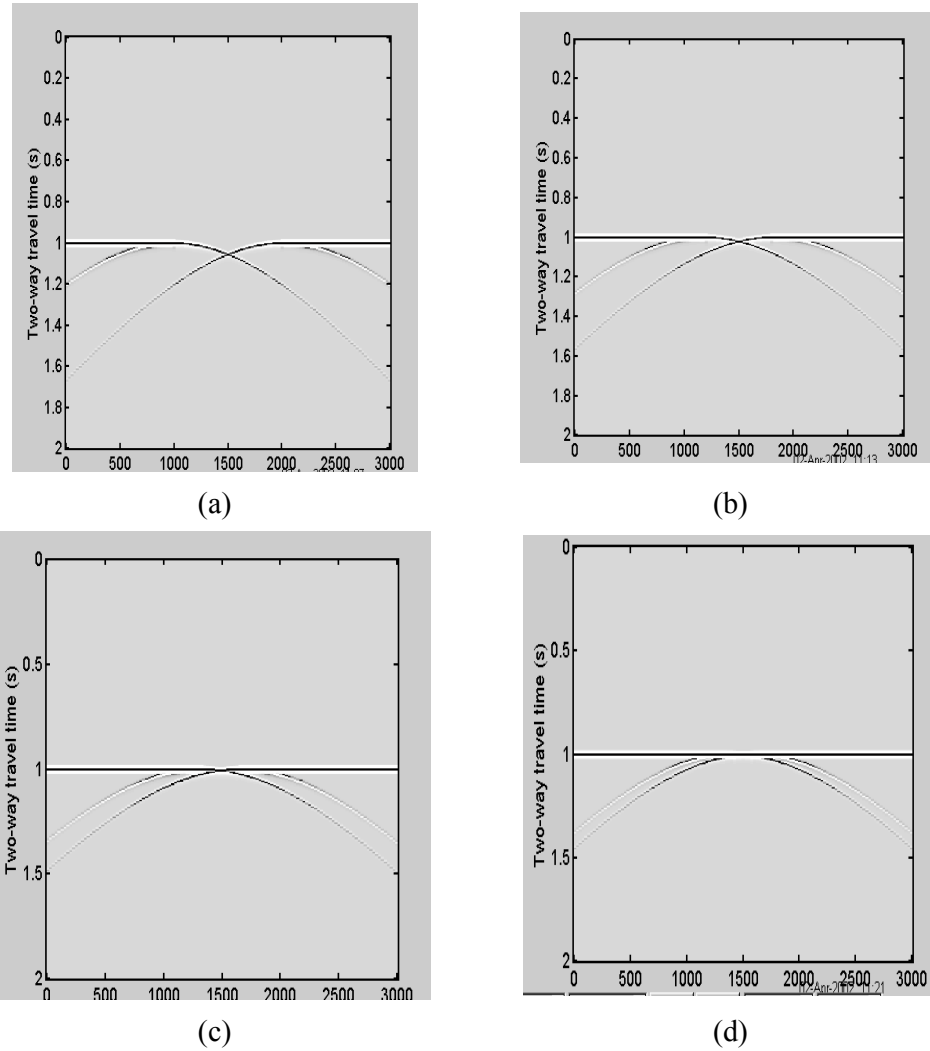
Figure 3.16. Diffraction response for a horizontal reflector with a gap in the middle, with gap size a) 1000m, b) 600 m, c) 280m,and d) 160m.

The radius of the Fresnel zone size is *280m,* the same as the gap size shown in Figure 3.16c. A larger gap would be evident in the stack section. However, even with the same size of Fresnel zone, the gap is difficult to be detected in the stack section. Migration does improve the gap image when the gap size is larger than 25% of wavelength (Margrave, 1999). The same phenomena will be depicted for a dipping reflector.

3.5.2 Dipping reflector
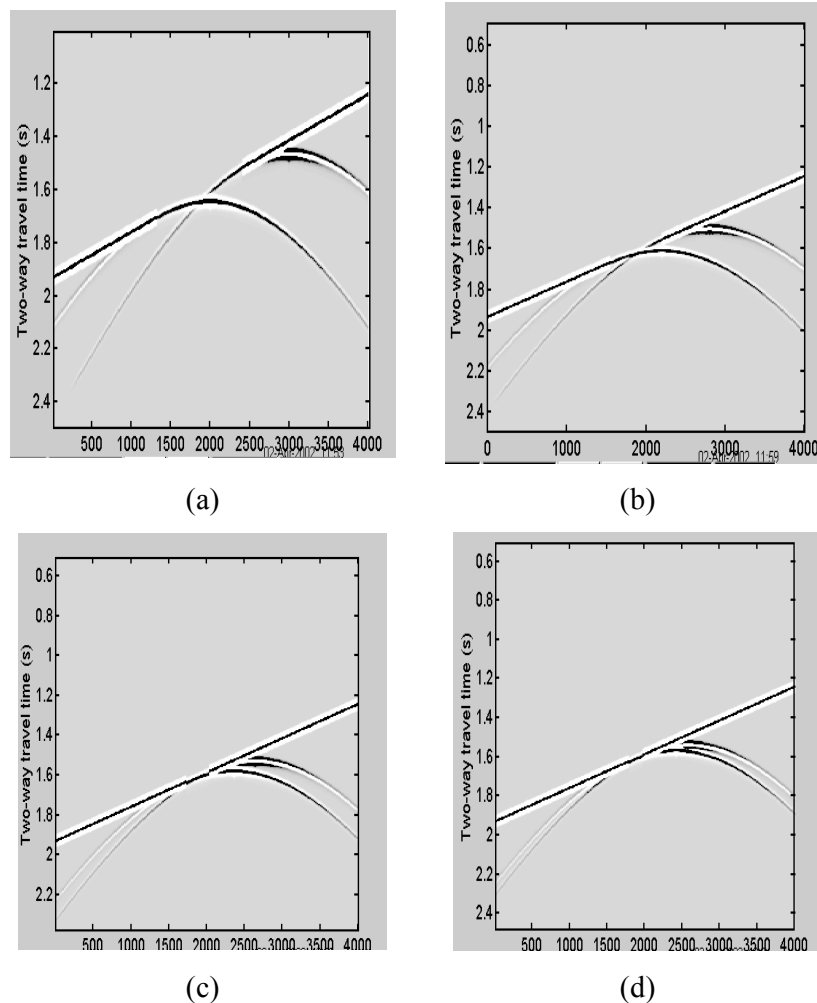
Figure 3.17. Diffraction response of a dipping reflector with a gap in the middle of the surface, with gap size a) 1000m, b) 600 m, c) 280m and d) 160m.

In Figure 3.17a, when the gap is much larger than the Fresnel zone, diffractions at the edges of the reflector are clearly identified on the stack section, and can be observed with different polarity. Furthermore the amplitude of the left side diffraction with a lower depth is smaller than the amplitude of the diffraction from the right side. When the gap size is much smaller, the gap cannot be distinguished on the stack section, as with the horizontal case. An estimation of the dipping Fresnel zone is made

by averaging the two Fresnel zones at each end of the gap.

3.6 The Fresnel zone concept expansions

Prestack data contains an additional dimension of offset and produces construction to the diffraction, thus it is worthwhile to define the Fresnel zone with half offset in prestack data volume, and use it to estimate the minimum migration aperture for prestack migration.

In the beginning of the 90's, geophysicists such as Schleicher (Schleicher, 1993), Hubral (Hubral, 1994) and Cerveny (Cerveny, 1994), devoted considerable time to define the Fresnel zone using a dynamic ray tracing or travel time calculation. However, in Kirchhoff prestack time migration, the travel time is kinematically determined by a surface that is referred to as Cheops Pyramid. Thus, defining the Fresnel zone on the surface of the Cheops Pyramid will contribute to the Kirchhoff prestack time migration as a convenient solution to estimate the minimum migration aperture.

3.6.1 The Fresnel zone definition for a horizontal reflector with offset

Figure 3.1 indicates the zero-offset Fresnel zone definition in the depth domain. In the time domain, which is more useful for Kirchhoff time migration, the Fresnel zone with zero-offset is the intersection with the hyperbola when the source wavelet travels down a half period ($\tau/2$) as illustrated in Figure 3.18.
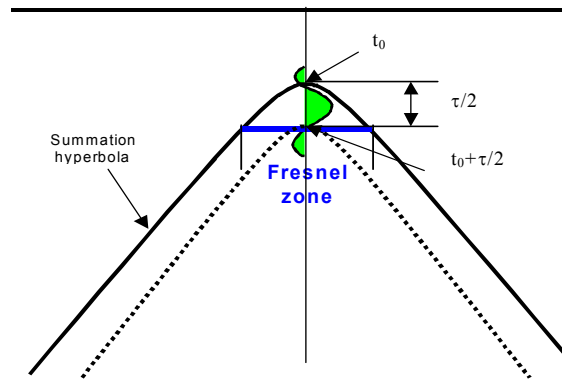
Figure 3.18. The Fresnel zone definition for

zero-offset in the time domain.

For prestack time migration, the Kirchhoff summation traveltime is a surface defined by the double-square-root (DSR) equation

$$t = \sqrt{\frac{t_0^2}{4} + \frac{(x+h)^2}{v^2}} + \sqrt{\frac{t_0^2}{4} + \frac{(x-h)^2}{v^2}} , \qquad (3.8)$$

where h is half source-receiver offset, t_0 is two-way vertical traveltime, v is RMS velocity at the scatter point, and x is the surface distance between the midpoint and the scatter point. This surface in the (x,h,t) volume is referred to as Cheops Pyramid.

A Fresnel zone is defined as the intercept when a spherical wave penetrates a plane to a depth of half a wavelength (Claerbout, 1985). For a horizontal reflector, according to Claerbout's definition mentioned above, the radius of the Fresnel zone x_f can be defined for an offset section as shown in Figure 3.19.
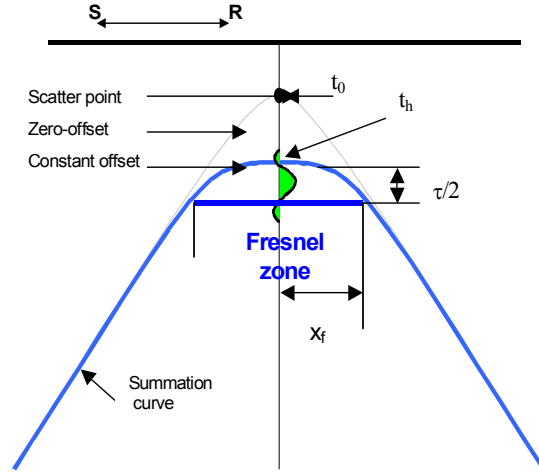
Figure 3.19. The Fresnel zone definition for

offset section in the time domain.

The DSR equation (3.8) can be rewritten exactly as:

$$t^2 = t_0^2 + \frac{4(x^2 + h^2 - \frac{4x^2 h^2}{v^2 t^2})}{v^2},$$ (3.9)

Using the offset Fresnel radius displacement x_f from Figure 3.19, and equation (3.9), we derive the time at the defined Fresnel zone by

$$(t_h + \frac{\tau}{2})^2 = (\sqrt{t_0^2 + \frac{4h^2}{v^2}} + \frac{\tau}{2})^2 = t_0^2 + \frac{4(x_f^2 + h^2 - \frac{4x_f^2 h^2}{v^2 t_h^2})}{v^2},$$ (3.10)

where t_h is the travel time at given half offset h and τ is the period of the wavelet. We can solve for the Fresnel zone radius x_f, assuming the ratio of τ to t_0 is small, giving:

$$x_f = \sqrt{\frac{\tau v^2 \sqrt{t_0^2 + \frac{4h^2}{v^2}}}{4 - \frac{16h^2}{v^2 t_0^2 + 4h^2}}}.$$ (3.11)

For zero offset, i.e. $h=0$, the Fresnel zone radius is exactly reduced to the same definition in Sheriff (1980), i.e.,

$$x_f = \frac{v}{2}\sqrt{t_0 \tau}.$$ (3.12)

Given a simple one horizontal reflector model as in Figure 3.20, and creating the

synthetic data of zero-offset, the convolutional model is used with a wavelet length of *0.04s*. The velocity is constant at *3000m/s* and the reflected point depth is *1500m*. Assuming there is no frequency decay in the source wavelet, the variation of the Fresnel zone radius versus the half source-receiver offset for a horizontal reflector is shown in Figure 3.21. As the Fresnel zone radius increases with half source-receiver offset, the migration aperture should also increase with half source-receiver offset.

surface

vp1, vs1, den1

reflector

vp2, vs2, den2
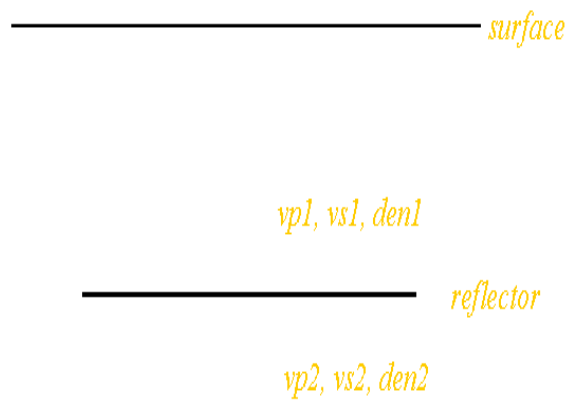
Figure 3.20. One horizontal reflector model.
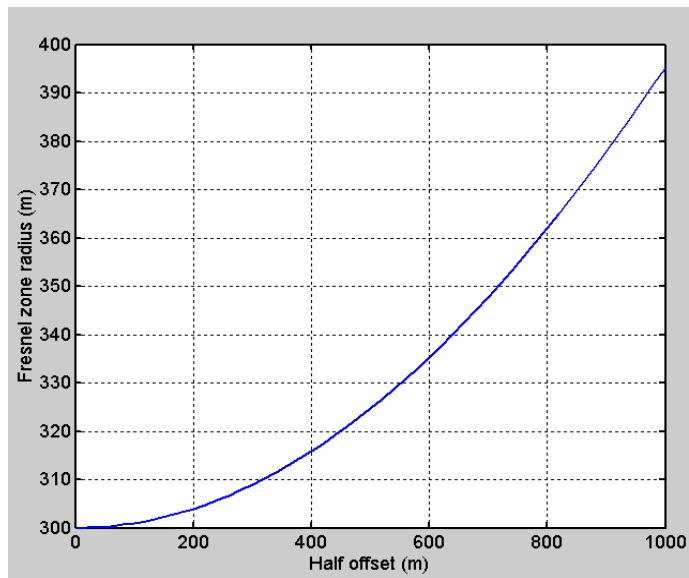
Figure 3.21. The Fresnel radius varying with half offset.

3.6.2 The Fresnel zone definition for a dipping reflector with offset

When the subsurface contains a dipping reflector, defining the Fresnel zone is more difficult than in the horizontal case, as Figure 3.22 indicates. In this figure the location of the reflection point $p(x_p, z_p)$, the source $(x_s, 0)$, and the receiver $(x_r, 0)$, are known. The dipping angle is β. The image of the source is defined by s'.
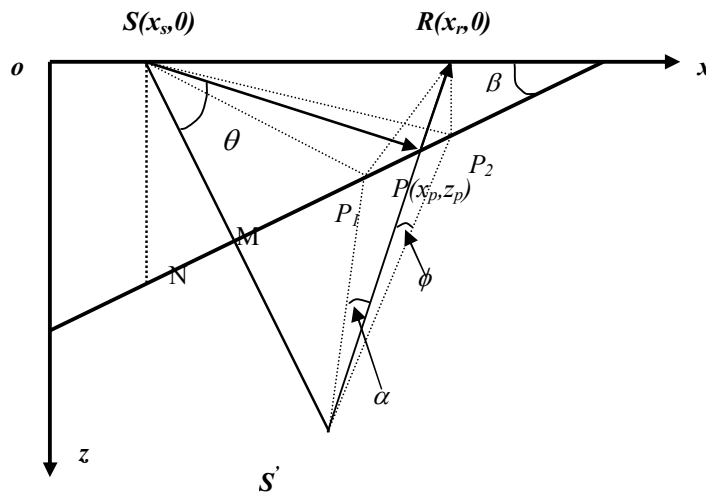
Figure 3.22. Geometric explanation of the Fresnel zone for a dipping reflector.

I have used the definition of the Fresnel zone in Sheriff (1980) to estimate the Fresnel zone. We know that

$$S'P_1 + P_1R = S'P_2 + P_2R = S'R + \frac{\lambda}{2} \ . \tag{3.13}$$

where λ is the length of wavelet, S' is the virtual source, and PP_1 and PP_2 are the left and right Fresnel radius.

To solve for the Fresnel radius, first solve for SM and SN, giving

$$SM = \left| x_p - x_s \right| \cdot \tan \beta + z_p = \left| x_p - x_s \right| \cdot \tan \beta + vt_0 / 2, \tag{3.14}$$

and

$$SN = \left| x_p - x_s \right| \cdot \sin \beta + z_p \cdot \cos \beta = \left| x_p - x_s \right| \cdot \sin \beta + \cos \beta \cdot v \cdot t_0 / 2. \tag{3.15}$$

Then solve for the angle θ,

$$S'R = 2 \cdot \sqrt{h^2 + SN^2 - 2h \cdot SN \cdot \sin\beta}, \qquad (3.16)$$

and

$$\cos\theta = \frac{2 \cdot SN - 2 \cdot h \cdot \sin\beta}{S'R}. \qquad (3.17)$$

Therefore

$$\theta = \arccos(\frac{2 \cdot SN - 2 \cdot h \cdot \sin\beta}{S'R}). \qquad (3.18)$$

After all these steps we can now solve for the left Fresnel radius PP_1

$$SP_1 + P_1 R = S'R + \frac{\lambda}{2}, \qquad (3.19)$$

and

$$P_1 R^2 = SP_1^2 + S'R^2 - 2 \cdot \cos\alpha \cdot S'R \cdot SP_1, \qquad (3.20)$$

also

$$SP_1 = \frac{SN}{\cos(\theta - \alpha)}. \qquad (3.21)$$

Together with

$$\cos(\theta - \alpha) = \cos\theta \cdot \cos\alpha + \sin\theta \cdot \sin\alpha, \qquad (3.22)$$

it can be determined that,

$$(\cos\theta \cdot \lambda \cdot S'R + \lambda^2 \cdot \cos\theta / 4 + 2 \cdot S'R \cdot SN) \cdot \cos\alpha + ...$$
$$(\lambda \cdot \sin\theta \cdot S'R + \lambda^2 \cdot \sin\theta / 4) \cdot \sqrt{1 - \cos\alpha^2} - (2 \cdot S'R + \lambda) \cdot SN = 0 \qquad (3.23)$$

To solve equation (3.23), let $(2 \cdot S'R + \lambda) \cdot SN = \delta_1$,

$\lambda \cdot \sin\theta \cdot S'R + \lambda^2 \cdot \sin\theta / 4 = \delta_2$, and $\cos\theta \cdot \lambda \cdot S'R + \lambda^2 \cdot \cos\theta / 4 + 2 \cdot S'R \cdot SN = \delta_3$,

then

$$\cos\alpha = \frac{\delta_3 \cdot \delta_1 + \sqrt{\delta_3^2 \delta_1^2 - (\delta_3^2 + \delta_2^2) \cdot (\delta_1^2 - \delta_2^2)}}{\delta_3^2 + \delta_2^2}. \qquad (3.24)$$

The left Fresnel radius is expressed by α and θ,

$$P_1 P = SN \cdot (\tan\theta - \tan(\theta - \alpha)). \qquad (3.25)$$

Now with equation (3.16), (3.17) and (3.18), PP_2 can be solved by the same way as for PP_1. The first step is to solve the angle ϕ, let $2 \cdot S'R \cdot SN + \lambda \cdot SN = \omega_1$, $\lambda \cdot \sin\theta \cdot S'R + \lambda^2 \cdot \sin\theta / 4 = \omega_2$ and $\cos\theta \cdot S'R \cdot \lambda + \lambda^2 \cdot \cos\theta / 4 + 2 \cdot S'R \cdot SN$, then obtain

$$\cos\phi = \frac{\omega_3 \cdot \omega_1 + \sqrt{\omega_3^2 \cdot \omega_1^2 - (\omega_3^2 + \omega_2^2) \cdot (\omega_1^2 - \omega_2^2)}}{\omega_3^2 + \omega_2^2} . \qquad (3.26)$$

Using angle ϕ and θ, the right Fresnel radius can be obtained as

$$PP_2 = SN \cdot (\tan(\theta + \phi) - \tan\theta) . \qquad (3.27)$$

During the derivation of the angle α and ϕ, there can be two roots for each angle. How to determine which root to use is up to the dipping direction. In this thesis all the dipping directions are as shown in Figure 3.22. However, no matter what the dipping direction is, the right Fresnel radius added to the left Fresnel radius is the same for the same reflected point. So in this thesis the plus sign is adopted.

The size of the Fresnel zone for a given point in the dipping reflector varies with half offset as the horizontal reflector. Figure 3.23 shows the variation of the radius of the Fresnel zone for left and right side.
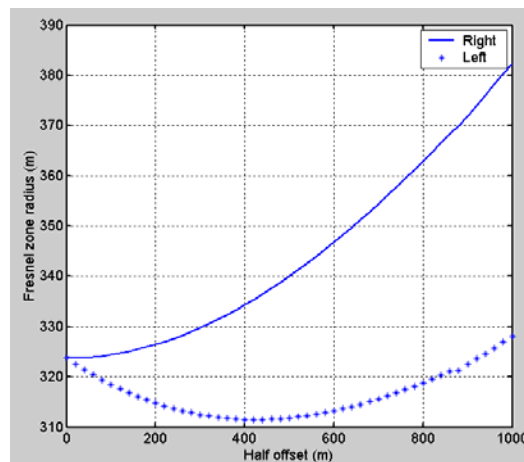
Figure 3.23. The Fresnel radius varies with half offset for a reflection point on a dipping reflector.

In addition, the total size of the Fresnel zone varies with half offset as depicted in Figure 3.24.
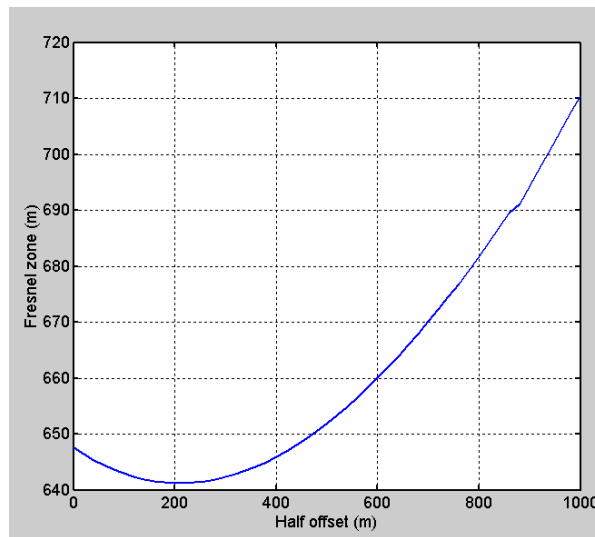
Figure 3.24. The Fresnel zone size variation with half offset for a reflection point on a dipping reflector.

From the figure above, we observe that the Fresnel zone first reduces in size then increases with increasing half offset. This initial reduction is one difference between a horizontal and a dipping reflector. Compared with the same depth point in a horizontal reflector, the Fresnel zone size in a dipping reflector is larger. Consequently, the migration aperture for a dipping reflector needs to be larger than for a corresponding horizontal reflector.

3.7 The Fresnel zone on Cheops Pyramid

An event may be constructed from a series of scatterpoints located along the event. In 2-D poststack forward modeling, the section is created by placing a hyperbola at each scatterpoint, the shape of which is defined by RMS velocity at the scatterpoint. In the prestack volume (x, h, t), the DSR equation describes the traveltime from a scatter point as a surface that is referred to as Cheops Pyramid (Claerbout, 1985). Rather than

use 2-D diffractions or hyperbolas as in the poststack model (x, t), prestack modelling uses the 3-D surface of Cheops Pyramid to recreate the reflection surface in (x, h, t). The prestack surface may be modeled by placing a Cheops Pyramid at each scatterpoint, with a shape defined by the RMS velocity at the scatterpoint.

To migrate the energy back to a scatterpoint, the prestack migration sums all the energy along the Cheops Pyramid. However the actual reflection energy, i.e. the 'specular' energy, from a linear reflector, comes from an area proportional to the size of the Fresnel zone.

3.7.1 The Horizontal Reflector

Modeling a horizontal reflector

Figure 3.25 shows a horizontal hyperbolic cylinder that represents the hyperbolic moveout from a horizontal reflector in a constant velocity medium. Below the hyperbolic cylinder is a Cheops Pyramid formed from one scatter point that lies on the horizontal reflector. The Cheops Pyramid is tangent to the hyperbolic cylinder at constant x, or at the CMP gather that passes through the scatter point.

The hyperbolic cylinder can be considered a reconstruction of many Cheops Pyramids from many horizontal scatter points. In Figures 3.25a - b, the Cheops Pyramid has had the time reduced by a small fraction, so that it will protrude through the hyperbolic cylinder, to illustrate the area of tangency. This area of tangency is more obvious in (b), surrounding the CMP gather located at the scatter point.
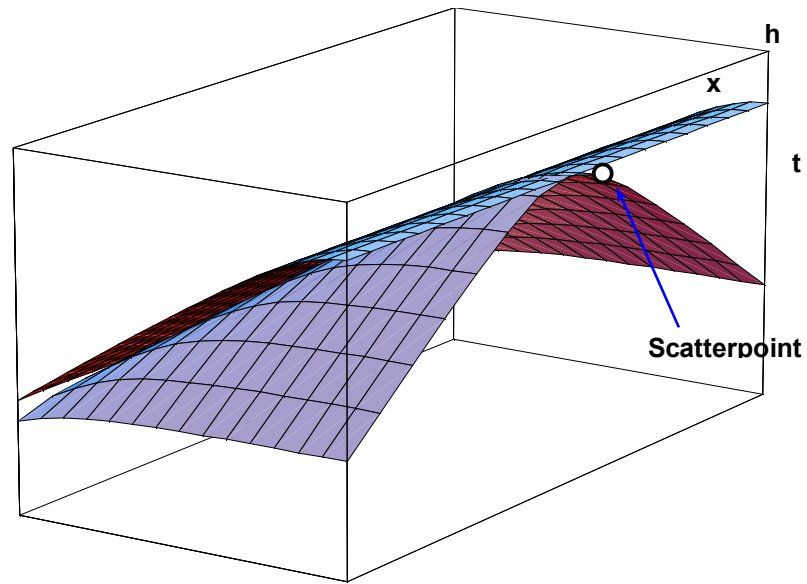
(a)
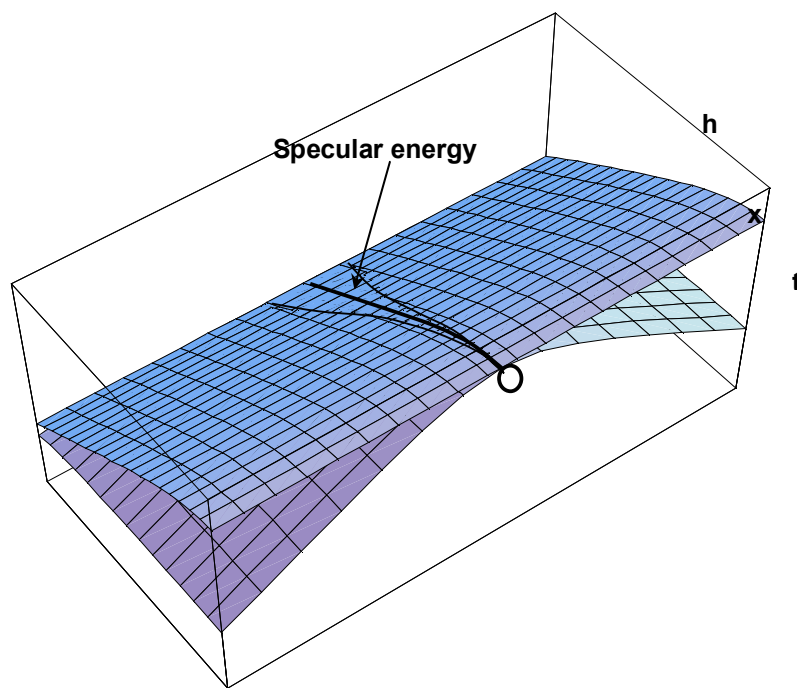
(b)

Figure 3.25. Two perspective views a) and b) of prestack surface from a horizontal reflector with a scatter point and Cheops Pyramid (Bancroft, 2002).

For a horizontal reflector, the high frequency 'specular' energy lies on a hyperbola

as shown by a solid curve in Figure 3.26a, and corresponds to a common midpoint (CMP) gather. A band limited Fresnel zone is also shown on Cheops Pyramid by the dash curves. The Fresnel zone can be seen more clearly by the vertical curves in the plan view of Cheops Pyramid as shown in Figure 3.26b. The shape of this Fresnel zone is defined by equation (3.11).
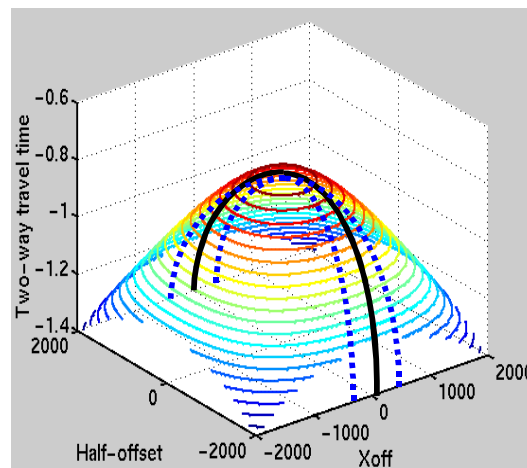
(a)
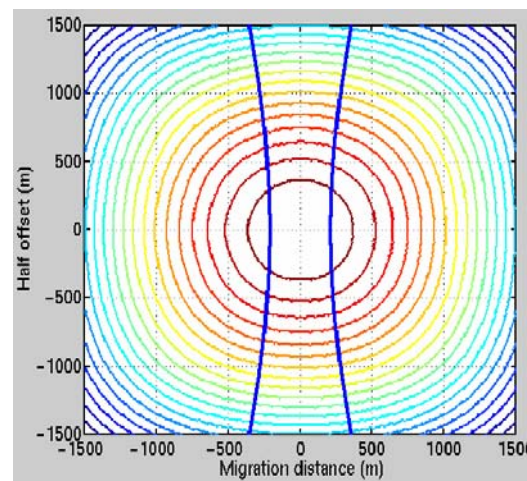
(b)

Figure 3.26. Specular energy and Fresnel zone of a horizontal reflector in a) Cheops Pyramid in (x, h, t), and b) contours of Cheops Pyramid in (x, h).

The shape of the Fresnel zone can also be illustrated by the intersection of Cheops

Pyramid with the prestack surface of the specular energy from a horizontal reflector: a hyperbolic cylinder. Raising the Cheops Pyramid by half period $\tau/2$ produces an intersection that maps the Fresnel zone as illustrated in Figure 3.27. The front view is shown in (a) and a view from above is shown in (b). In prestack migration, it is this overlapping area that contributes reflection energy to the migration result. Summation of energy over the remaining portion of Cheops Pyramid will only contribute noise.

(a)

(b)
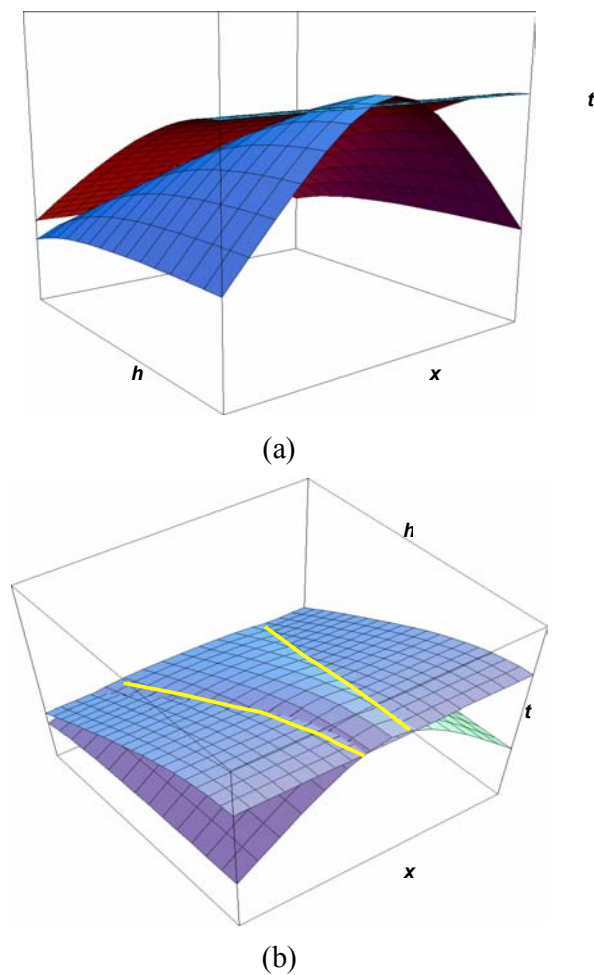
Figure 3.27. Prestack Fresnel zone for a horizontal reflector defined by intersection with a slightly raised Cheops Pyramid, a) frontal view and b) from above (Bancroft, 2002).

3.7.2 The Dipping Reflector

Modelling a dipping event

A 2-D dipping event, illustrated in the ray tracing of Figure 3.28, may be modelled in the prestack volume (*x, h, t*), to produce the surface in Figure 3.29a. This surface is exactly hyperbolic in each CMP gather. Dip-dependent moveout (DD-MO) corrects offset time in the CMP gathers to a zero-offset time; however the actual offset reflection points should move updip from this CMP gather (Figure 3.28a).

In a manner similar to 2D diffraction modelling, the prestack hyperbolic surface of Figure 4.2a, may also be modelled by a reconstruction of Cheops Pyramids, formed from a series of scatterpoints that are located along the dipping event, as illustrated by one scatterpoint in Figure 3.29b.

Figure 3.28b shows the various offset raypaths for a single reflecting point on the dipping event. As the offset *h* increases, the distance on the surface between CMP and the reflecting point increases, and more down dip as indicated by the black dots.

(a)   (b)
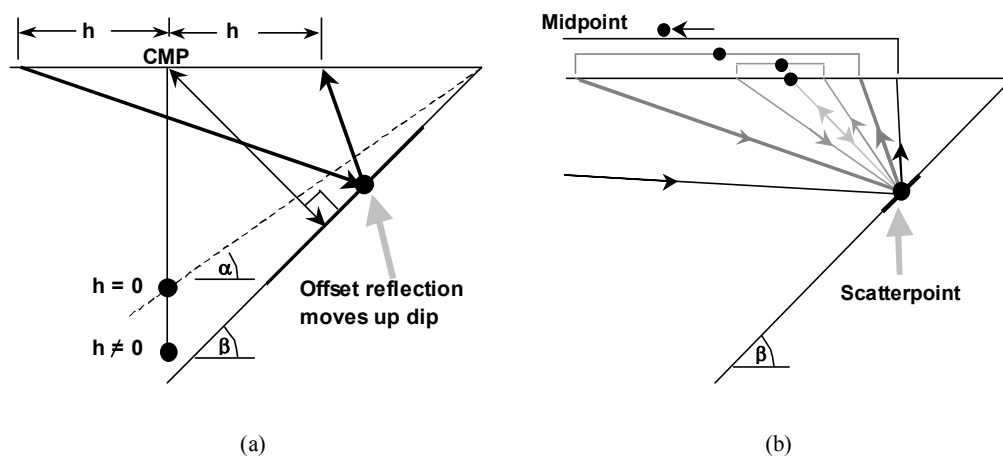
Figure 3.28. Dipping reflections illustrating in a) reflection times in a CMP gather, and b) the offset raypaths for a single reflection point (Bancroft, 2002).

The surfaces in Figures 3.29 (a) and (b) are combined in (c) to illustrate the area of tangency between the dipping surface and Cheops Pyramid. The black line defines the theoretical tangency location, while the gray band was formed by slightly reducing the time of Cheops Pyramid. As the offset is increased, the area of tangency curves down dip corresponding to that indicated in Figure 3.28b. It is the energy in this tangency band that should be summed to the reflection point, i.e. prestack migration by summing over Cheops Pyramid.

Summing the hyperbolic energy in a CMP gather does not accomplish the same task, but smears the reflection point energy along the zero-offset dip.

(a)   (b)
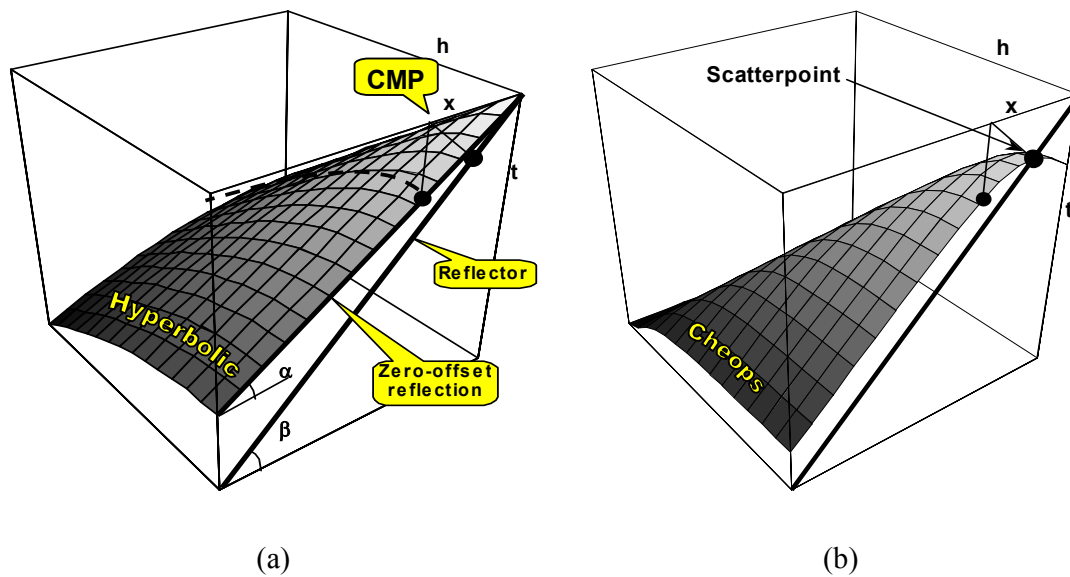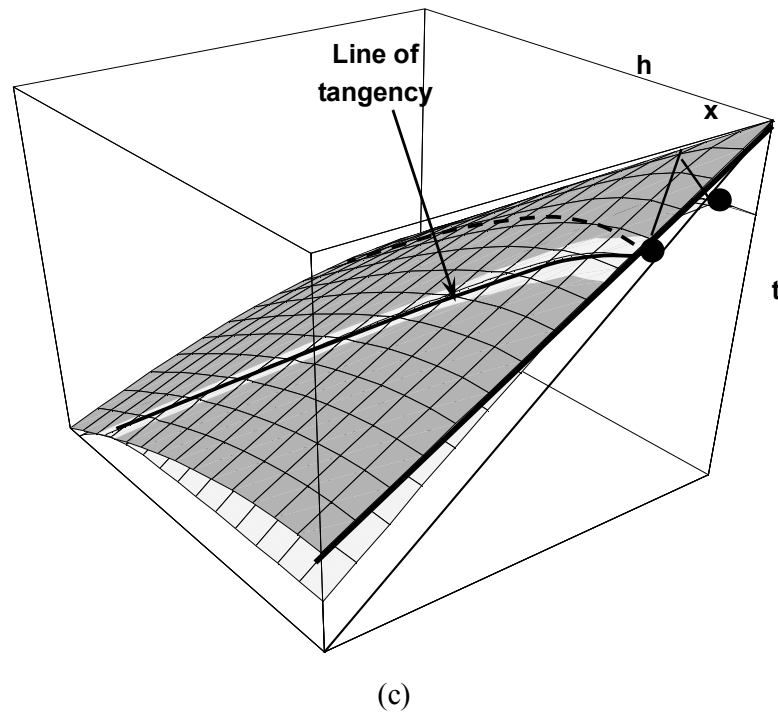
Figure 3.29. Dipping prestack surface from series of scatterpoints and Cheops Pyramids, a) the dipping prestack surface, b) Cheops Pyramid from one scatter point, and c) a combination of (a) and (b) showing the line of tangency (Bancroft, 2002).

For a dipping reflector, the reflected point is located on the zero offset section, which is not coincident with the scatterpoint. To define the Fresnel zone in Cheops Pyramid, we need first to define the distance *x* (surface distance from scatterpoint to common mid- point).
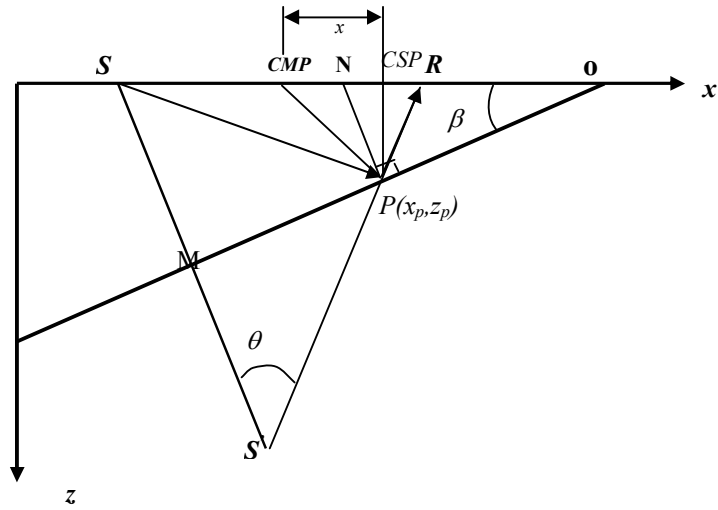
Figure 3.30. Geometric explanation of migration distance x.

Consider Figure 3.30, in which the surface distance between the CMP and CSP is given as x. When the source-receiver offset increases, the distance x increases too. To solve the relation between half offset h and migration distance x, assuming the half-offset h, the location of the reflected point $p(x_p, z_p)$ and the dip angle of the reflector β are known, the migration distance x can locate the tangent line in Cheops Pyramid.

In triangle $SS'R$, $SR = 2 \cdot h$, angle $S'SO$ equals 90^0-β. To solve the relation, first we need to obtain the angle θ.

In triangle OSM,

$$\frac{NP}{SM} = \frac{OP}{OP + PM},\tag{3.28}$$

and

$$PM = SM \cdot \tan\theta,\tag{3.29}$$

together with

$$NP = \frac{vt_0}{2 \cdot \cos\beta},\tag{3.30}$$

allow one to obtain

$$OP = \frac{SM \cdot \tan \theta \cdot vt_0}{2 \cdot \cos \beta \cdot SM - vt_0} . \tag{3.31}$$

Then $\cos\theta$ can be solved using

$$\sin \beta = \frac{vt_0 \cdot (\cos \beta \cdot SM - vt_0 / 2)}{SM \cdot \tan \theta \cdot vt_0} , \tag{3.32}$$

to get

$$\cos \alpha = \frac{SM \cdot \sin \beta}{\sqrt{SM^2 + (vt_0 / 2)^2 - vt_0 \cdot \cos \beta \cdot SM}} . \tag{3.33}$$

After obtaining of $\cos\theta$, SM can be obtained.

$$S'R^2 = 4 \cdot h^2 + 4 \cdot SM^2 - 2 \cdot \sin \beta \cdot 2 \cdot SM \cdot 2 \cdot h , \tag{3.34}$$

with

$$4 \cdot h^2 = 4 \cdot SM^2 + S''R^2 - 2 \cdot 2 \cdot SM \cdot \cos \theta \cdot S'R , \tag{3.35}$$

and equation (3.33), the SM can be solved as below. Let

$$b = \frac{2 \cdot \sin^3 \beta \cdot h - 2 \cdot \sin \beta \cdot h - vt_0 \cdot \cos \beta}{\cos^2 \beta} , \tag{3.36}$$

$$c = \frac{v^2 t_0^2 / 4 + 2 \cdot \sin \beta \cdot \cos \beta \cdot vt_0 \cdot h}{\cos^2 \beta} , \tag{3.37}$$

$$d = -\frac{\sin \beta \cdot h \cdot v^2 t_0^2 / 2 + vt_0 \cdot \cos \beta \cdot \sin^2 \beta \cdot h^2}{\cos^2 \beta} , \tag{3.38}$$

$$e = \tan^2 \beta \cdot h^2 \cdot v^2 \cdot t_0^2 / 4 . \tag{3.39}$$

Then let

$$A = -c , \tag{3.40}$$

$$B = b \cdot d - 4 \cdot e , \tag{3.41}$$

$$C = 4 \cdot c \cdot e - b^2 \cdot e - d^2 , \tag{3.42}$$

$$p = B - A^2 / 3 , \tag{3.43}$$

$$q = \frac{2 \cdot A^3}{27} - \frac{A \cdot B}{3} + C, \tag{3.44}$$

and

$$M = (-\frac{q}{2} + \sqrt{(\frac{q}{2})^2 + (\frac{p}{3})^3})^{\frac{3}{2}} + (-\frac{q}{2} - \sqrt{(\frac{q}{2})^2 + (\frac{p}{3})^3})^{\frac{3}{2}}, \tag{3.45}$$

$$Y = M - \frac{A}{3}, \tag{3.46}$$

$$H(1,2) = \frac{1}{2}(b \pm \sqrt{b^2 - 4 \cdot c + 4 \cdot Y}, \tag{3.47}$$

$$I(1,2) = \frac{1}{2}(Y \pm \sqrt{Y^2 - 4 \cdot e}), \tag{3.48}$$

Thus *SM* is obtained as:

$$SM = \frac{-H \pm \sqrt{H^2 - 4 \cdot I}}{2}. \tag{3.49}$$

However, there are four roots in equation (3.49), and which one is physically relevant depends on the dipping direction. In this thesis, all dipping direction is the same as shown in Figure 3.30 or Figure 3.22. In this kind of dipping environment we get

$$SM = \frac{-H_2 + \sqrt{H_2^2 - 4 \cdot I_2}}{2}. \tag{3.50}$$

To get the distance *x*, two separated situations need to be considered:

1. The incident angle is smaller than the dipping angle;
2. The incident angle is larger than the dipping angle.

With the first condition, distance *x* is,

$$i_{incident} = \arctan(\frac{2 \cdot SM}{\sin \beta \cdot v \cdot t_0} - \frac{1}{\tan \beta}) - \beta, \tag{3.51}$$

and

$$x = h + \tan(i_{incident} - \beta) \cdot v \cdot t_0 / 2. \tag{3.52}$$

With the second condition x is,

$$x = \frac{\tan \beta \cdot v \cdot t_0}{2} + h - \frac{h \cdot v \cdot t_0}{2 \cdot SM \cdot \cos \beta} \; . \tag{3.53}$$

For example, assume the scatter point depth is *2000 m* and velocity is *3000 m/s*. Then x increases with h as described in Figure 3.31.
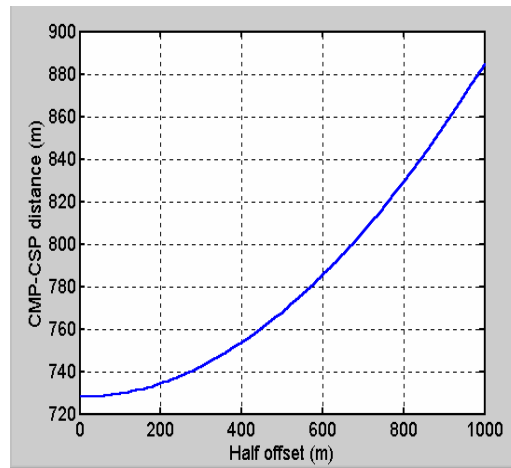
Figure 3.31. The distance x varying with half offset for the given reflection point.

For a dipping reflector the high frequency 'specular' energy of the scatter point is shown in Figure 3.32a by a solid curve. The band limited Fresnel zone as a function of the half source-receiver offset in Cheops Pyramid is shown by the dash curves. The offset Fresnel zone can be seen more clearly by the contours in the plane view of Cheops Pyramid as shown in Figure 3.32b.
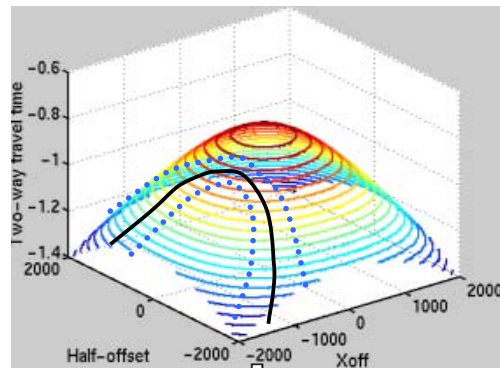
(a)
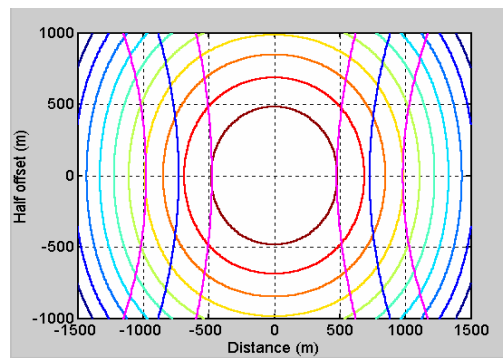
(b)

Figure 3.32. Specular energy and the Fresnel zone of a dipping reflector in a) Cheops Pyramid in (x, h, t), and b) contours of Cheops Pyramid in (x, h).

3.8 The migration aperture relates to the Fresnel zone

Migration is used not only for structural correction but also for estimating the true reflection amplitude. To get the true reflection amplitude, both the migration aperture and its location are the determining factors. However, for a horizontal reflector, the tangent point, i.e. the reflection point, is the same point as the scatter point. In this case the migration aperture is centered at the scatter point. For a dipping reflector, the area of tangency between the reflection and diffraction curve identifies the migration aperture.

What is the minimum migration aperture really needed to migrate a point to get the true reflection amplitude? Traditionally we use a migration aperture that is as large as possible, assuming that it can give the best migration result. In fact, the migration aperture need not be so large to give the complete reflection amplitude from a linear reflector. In such cases the minimum migration aperture should guarantee the true reflection amplitude. A larger migration aperture makes no improvement on the migration amplitude (for a linear reflector). Numerical examples show that the minimum prestack migration aperture, to preserve the true amplitude, should be the size of the Fresnel zone defined in the above sections.

3.8.1 The two layer model

The minimum migration aperture is suitable not only for the zero-offset section but also for the offset-section. The discussion of migration aperture in the next section will be divided into two parts: a zero-offset section and an offset section. I will use the same two layer model as Ostrander's model in 1984.

Table 1 Parameters for model

	Vp(m/s)	Vs(m/s)	Density(g/c)	Depth(m)
First layer	3048	1244	2.4	1500
Second layer	2438	1625	2.14	2000
Below second layer	3048	1244	2.4	2000

3.8.2 The Fresnel radius size for these two layers

The Fresnel zone sizes for both layers are shown in Figure 3.33. As the reflector gets deeper, the Fresnel radius increases. The second layer Fresnel radius is obtained using RMS velocity.
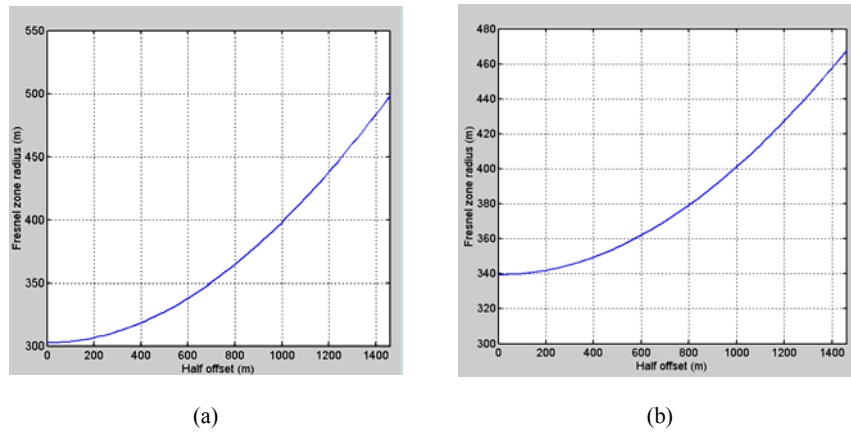
Figure 3.33. The Fresnel radius varies with half offset for both layers of the modes. (a)
The first layer;(b) The second layer.

3.8.3 Migration results for zero-offset section

In exploration seismology the stack section is assumed to be a zero-offset section, and thus post-stack migration is used after stack for geological structural correction. However, in a prestack constant offset migration algorithm, migrating the zero-offset section is similar to migrating an offset section and the zero-offset section becomes a special case. The migration aperture investigation in this thesis is based on a constant offset prestack algorithm, and furthermore, it is also suitable for post-stack. A series of pictures is shown in Figure 3.34, in which the migration was carried out with varying size of aperture. In each case the amplitude was picked and plotted against the aperture size. These Figures reveal that a migration aperture, the size of the Fresnel zone, will produce a stable amplitude response, and a larger aperture cannot improve the amplitude processing.

Fresnel zone size
Fresnel zone size
Migration amplitude
Migration aperture (m)
-0.5
-0.45
-0.4
-0.35
-0.3
-0.25
-0.2
-0.15
-0.1
-0.05
0
0.5
0.45
0.4
0.35
0.3
0.25
0.2
0.15
0.1
0.05
0
200
400
600
800
1000
1200
1400

(a) (b)
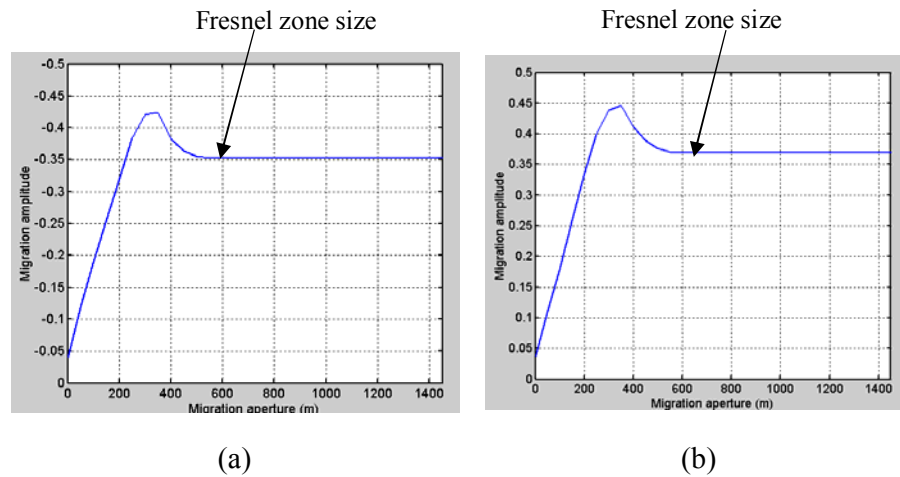
Figure 3.34. Zero-offset migration results. (a) the first layer; (b) the second layer

In these two pictures, the migration amplitude first goes up to a maximum, then reduces to stable level, at a point corresponding to an aperture with the Fresnel zone size. An aperture larger than it will produce no improvement to migration amplitude. This stable point also indicates a minimum aperture size for true amplitude migration.

3.8.4 Migration results for offset section

The discussion on the zero-offset case is also suitable for an offset section. Figure 3.35 shows the offset migration results from our model using a constant source-receiver offset of *2000m*.

Fresnel zone size
Fresnel zone size
Migration amplitude
Migration aperture (m)
-0.6
-0.5
-0.4
-0.3
-0.2
-0.1
0
0.6
0.5
0.4
0.3
0.2
0.1
0
200
400
600
800
1000
1200
1400

(a) (b)
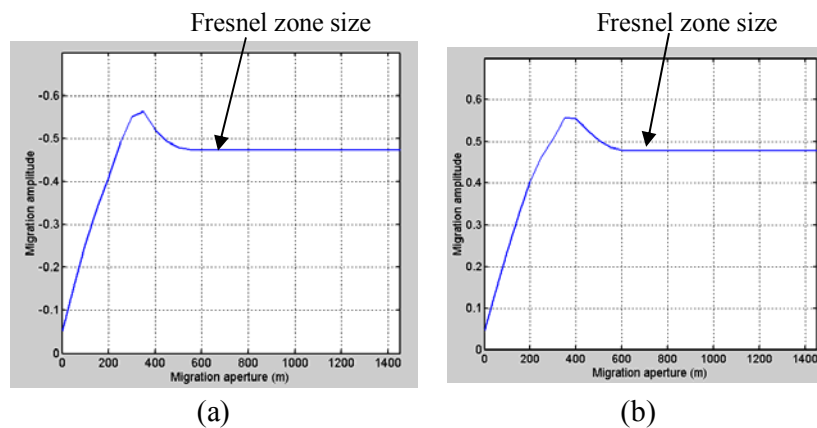
Figure 3.35. Offset migration results. (a) the first layer; (b) the second layer.

The results are similar to the zero offset case where the migration amplitude first

goes up, then goes down, and then down to be stable. Once again the first stable point indicates a minimum migration aperture is the size of the Fresnel zone.

3.8.5 The taper width effect

In the diffraction stack algorithm, there is another factor called the taper function used to reduce the migration noise. Does it have an effect on migration amplitude? It doesnot if the migration aperture is large enough as shown previously, and if the taper starts after the stable point. The type of taper used has no influence on migration amplitude, as illustrated in Figure 3.36. The migration aperture used to test the taper effect is *1000m*. In these Figures, there is no change in the migration amplitude when the taper size is varied.
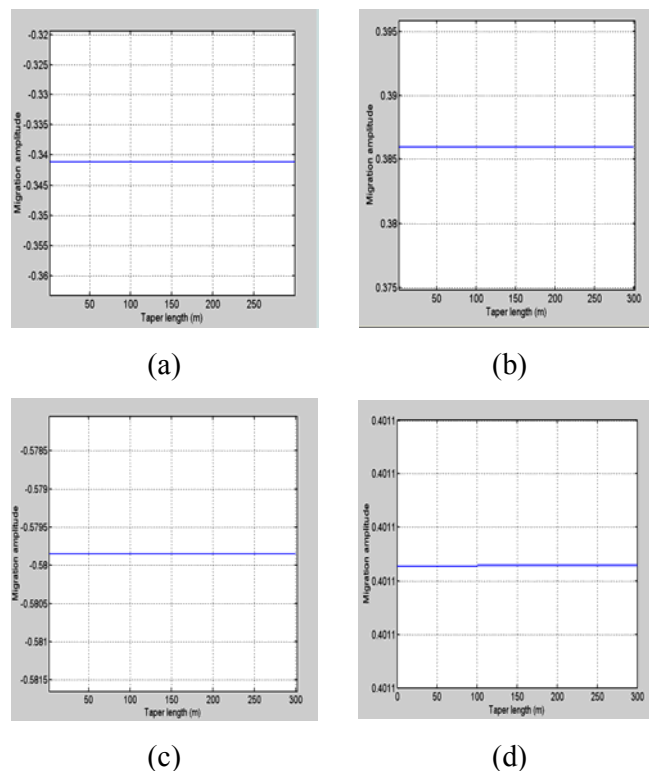
Figure 3.36. Taper size has no effect on migration amplitude when migration aperture is large enough. With zero-offset section a) the first layer, b) the second layer; and offset section c) the first layer, d) the second layer.

In summary, the minimum migration aperture is related to the size of the Fresnel zone in both the post-stack case and the prestack case. We therefore use the Fresnel zone concept to define the aperture size in the migration algorithm. The minimum migration aperture, as discussed above, is defined by the Fresnel zone size with a Ricker wavelet. This size of aperture will save computer time.

3.9 Chapter Conclusions

First, the Fresnel zone size depends on the source wavelet. As demonstrated in Section 3.3, with a limited bandwidth seismic wavelet, the reflected energy reaches its maximum when the size of the reflector is the size of the Fresnel zone.

Second, the amplitude of the reflection is influenced by the reflector size. When the reflector size is smaller than the Fresnel zone, the reflected energy collected is not the reflection coefficient. At the edge of the reflector the diffraction constructively builds the reflected energy.

Third, the Fresnel zone concept can be expanded to the offset section as defined in Section 3.6. In addition, the Fresnel zone in prestack data volume, i.e. Cheops Pyramid is described. With this discussion, it becomes easier to define the migration aperture in prestack data volume.

Finally, in this Chapter, the minimum migration aperture was evaluated for the detection of stable migration amplitude. It was concluded that the minimum migration aperture should be the size of the Fresnel zone. Migration apertures larger than this size will make no improvement to migration amplitude.

Chapter 4

CSP gather used for AVO analysis

4.1 Chapter summary

As introduced in Chapter 2, the equivalent offset method (EOM) of prestack migration was first introduced by Bancroft and his co-workers at the University of Calgary (Bancroft and Geiger, 1994). EOM is mainly a Kirchhoff prestack migration algorithm that is made up of two steps: common scatterpoint (CSP) gathering and Kirchhoff NMO and stack. Because of these two steps, EOM is easier to implement and faster than a conventional Kirchhoff prestack migration algorithm. Based on the Kirchhoff migration theory, the CSP gather provides a common scatter point gather, which uses the equivalent offset to locate data within the gather. It is worthwhile to investigate using the CSP gather as an AVO analysis tool.

In Chapter 3, the migration aperture was discussed. In this Chapter, the relationship between equivalent offset and incident angle along the specular energy will be discussed first. Then the different weighting functions will be used for CSP gathering and the results will be compared. Synthetic data examples verify that amplitude in a CSP gather is proportional to the reflectivity. In addition, the amplitude anomalies in a CSP gather can be used as an AVO indicator. Seismic processing can never produce amplitude close to the reflectivity, only relative amplitude that may be scaled using well log information. Limited aperture migration can be a dangerous procedure, as the migration will tend to match that of the geological model. It is assumed in this thesis that an accurate geological model has been developed, validating a limited aperture migration.

4.2 Equivalent offset and incident angle

Prestack migration moves the specular energy along the surface of Cheops Pyramid to the reflection point (or scatterpoint). The first step in the EOM, is the CSP gathering that moves the specular energy around Cheops Pyramid at the same time to form an equivalent hyperbola. We now investigate how this movement of data affects the angle of incidence.

In forward modelling, the high frequency reflection energy from one reflecting element on a horizontal reflector, i.e. specular energy, lies in one CMP gather and forms a hyperbola as a function of offset. This specular energy corresponds to the same traveltime band on a Cheops Pyramid when the scatterpoint is at the same location as the reflecting element and is shown as the solid line in Figure 4.1. Each point on the hyperbola of specular energy corresponds to a different raypath, and a different incident angle, where the incident angle varies with half offset h.
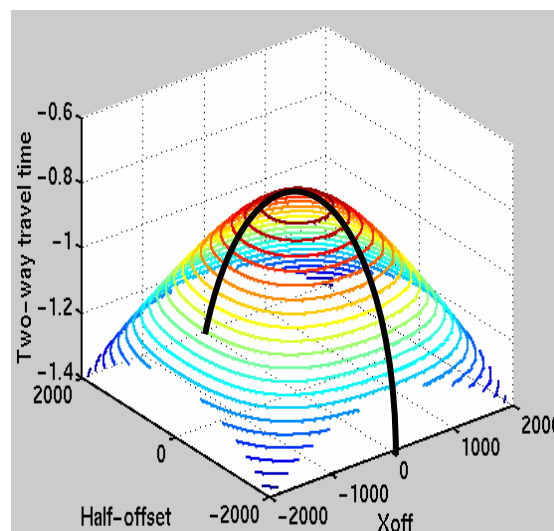

Figure 4.1. Reflection energy of a reflection point on a horizontal reflector forms a hyperbola on Cheops Pyramid.

When forming a CSP gather, the energy on the surface of Cheops Pyramid is summed to the location of the hyperbola in Figure 4.2 and is referred to as the equivalent

hyperbola. Any specular energy, i.e. the reflection energy, which is intersected by the Cheops Pyramid, is moved to its corresponding position in the equivalent hyperbola. The location of the specular energy varies with the incident angle θ or half source-receiver offset h. However, the equivalent offset h_e is also a function of h. The equivalent offset can be a function of the incident angle as represented in equation (4.1).

$$h_e^2(h,\theta) = h^2(\theta) + x_{off}^2 - \frac{4 x_{off}^2 h^2(\theta)}{(VT(\theta))^2}$$

(4.1)

When a reflector is horizontal the specular energy lies on the CMP gather or on the equivalent hyperbola and the equivalent offset h_e is equal to the half source-receiver offset h, i.e. when x_{off} is zero in equation (4.1). This location is shown as the vertical gray line in Figure 4.2a. The angle of incidence along this curve is shown in Figure 4.2b with the incidence angle for horizontal reflector shown above the curve. When the reflector is dipping, the specular energy moves down the side of Cheops Pyramid as indicated by the black curve in Figure 4.2a. This curve shows the location of specular energy for a dip of 30^0. Specular energy from the dipping event follows the contours of Cheops Pyramid to the equivalent hyperbola. Note, in Figure 4.21, that the zero-offset dipping energy moves to an offset location on the equivalent hyperbola as indicated by the curved arrow. The remaining data, when mapped to the equivalent hyperbola will be at increasing offset. This effect is illustrated in Figure 4.2b by the dip values displayed below the equivalent hyperbola.

Figure 4.2 applies only to high frequency specular energy, when the equivalent offset provides a one-to-one mapping of the incidence angle to the CSP gather. Band limited data will map a band of energy to the equivalent hyperbola. The mapping of this data provides a bridge between CSP gathers and amplitude analysis in common reflection point (CRP) gathers.
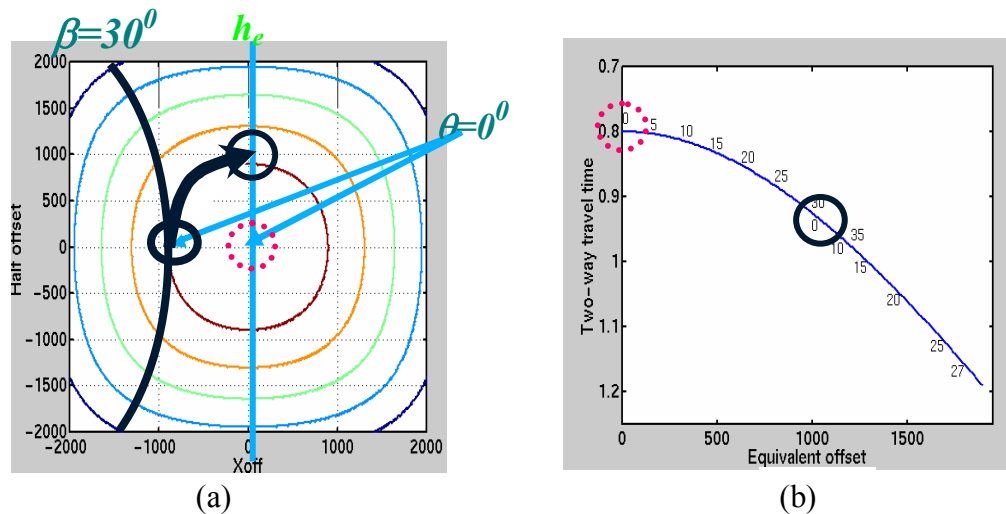
Figure 4.2. a) Contour of Cheops Pyramid relates equivalent offset, dipping angle β and incident angle θ; b) Relationship between equivalent offset and incident angle for horizontal and dipping reflector.

In forward modelling, incident angle corresponds to a unique equivalent offset. CSP gathering is an inverse process that collects all possible energy to CSP gather, where the energy moved to a certain equivalent offset position should correspond to a certain specific angle of incidence. The relationship between the equivalent offset and incident angle during CSP gathering, will be investigated to establish the uniqueness.

The CSP gathering is a mapping process from data in a CMP gather, (x,h,t), to a CSP gather (x,h_e,t) as defined by the hyperbola in Figure 4.1. To realize the mapping, there are three loops as shown in Figure 4.3

Loop 1: All CSP locations. (Outer loop)

⇩

Loop2: All input traces. (Middle loop)

⇩

Loop3: Each sample at a time at a computed EO (Inner loop)

Figure 4.3. CSP gathering process loops.

Initially the maximum equivalent offset is defined by using the maximum traveltime and velocity information in a seismic section. Then according to the trace information, calculate the CMP to CSP distance x_{off}, half offset h and loops over every input trace. The equivalent offset is then computed for 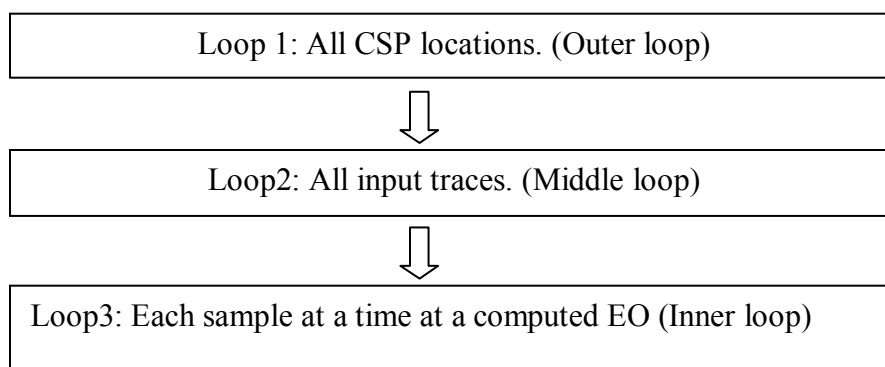all samples in the trace, summed into the appropriate location in the CSP gather (In production code, this algorithm is much more efficient than illustrated here). The whole CSP gathering is thus completed. Generally the equivalent offset is larger than the half offset but with the same interval. In doing this CSP gathering is naturally an anti-aliasing process (Bancroft et al, 1998).

CSP gathering was applied to the simple horizontal layer model shown in Figure 3.20. The same geometry was used as in Chapter 3 and a central surface location was chosen for comparing the amplitudes of a CMP gather with a CSP gather. Figure 4.4b shows the one sided CSP gather, with an energy distribution quite different from the one sided CMP gather shown in Figure 4.4a. This modeled data is perfect for a CMP gather where there is no noise, and the estimated amplitude is exact. The CSP gather is formed by summing all traces within the migration aperture and requires a reconstruction process to form the specula event on the equivalent hyperbola.

We therefore used the modeled data of the CSP gather in Figure 4.4b to illustrate this energy distribution. Note that all this energy is used in all full aperture prestack migrations, but is typically not visible to the user. It is a prestack migration gather, i.e. the CSP gather, which displays this information, and understanding its origin and effect on the migration result will aid in producing a better migration for imaging and AVO analysis.
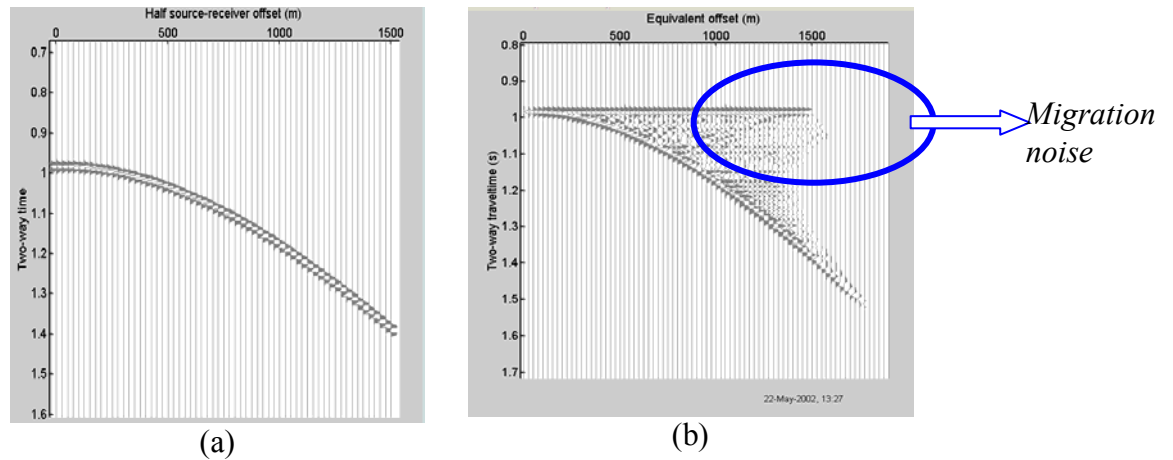
Figure 4.4. Comparison of a CSP gather with a CMP gather at the same surface location.

Figure 4.5a shows the amplitudes versus offset (AVO) extracted from the modeled CMP gather in Figure 4.4a. It is this amplitude distribution that we are intending to extract from the CSP gather. Figure 4.5b shows the amplitudes verses equivalent offset (EO) from the modeled CSP gather in Figure 4.4b. The comparison indicates it may not be a trivial task to extract amplitudes from the CSP gather as from CMP gathers, because of the energy that is collected and distributed when forming the CSP gather. For example, the zero-offset energy from the neighboring CMP gathers forms the flat event in Figure 4.4b. After movement correction, this energy curves up to zero time and is stacked out. It is the hyperbolic energy that becomes flat and is then stacked to define the reflector.

Figure 4.5. Amplitudes extract from a) CMP gather and b) CSP gather from Figure 4.4 correspondingly.

The main factor in equation (4.1) that affects the equivalent offset h_e is x_{off}. The other factors of T and V have only a time tuning effect. Thus, whether or not the migration noise comes from x_{off}, will be investigated below.
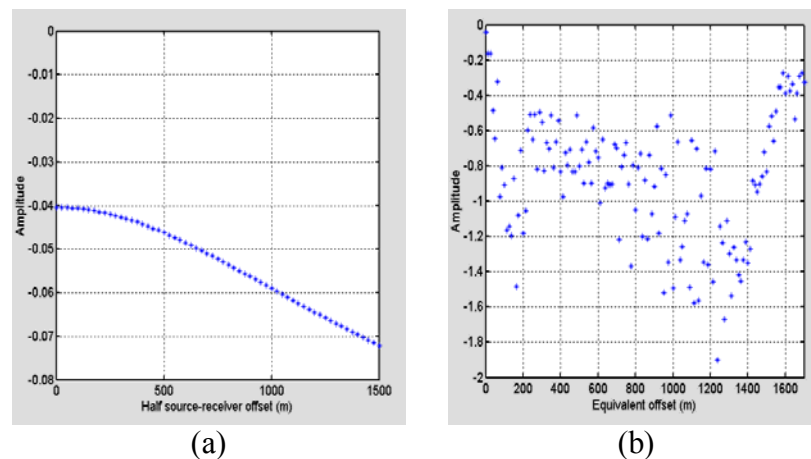
Smearing factor x_{off}

Equation (4.1) expresses the relationship between migration distance x_{off}, half offset h and equivalent offset h_e. To examine the relationship between migration distance x_{off} and equivalent offset h_e, a constant offset gather with constant half offset h is used to form the CSP gather. Figure 4.6 is the zero-offset section and its CSP gather is displayed in Figure 4.7, where, (a) is the CSP gather and (b) is the amplitude extracted from the CSP gather.
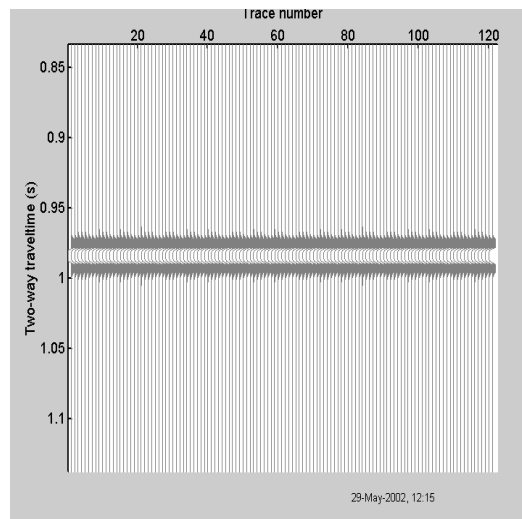
Figure 4.6. Zero-offset section

Figure 4.7 indicates that the horizontal event in the CSP gather of Figure 4.3b comes from the zero offset data and reaches its maximum at the edge of the survey. Although the zero equivalent offset corresponds to zero incident reflectivity, the other offsets could be eliminated.

<div align="center">(a)   (b)</div>
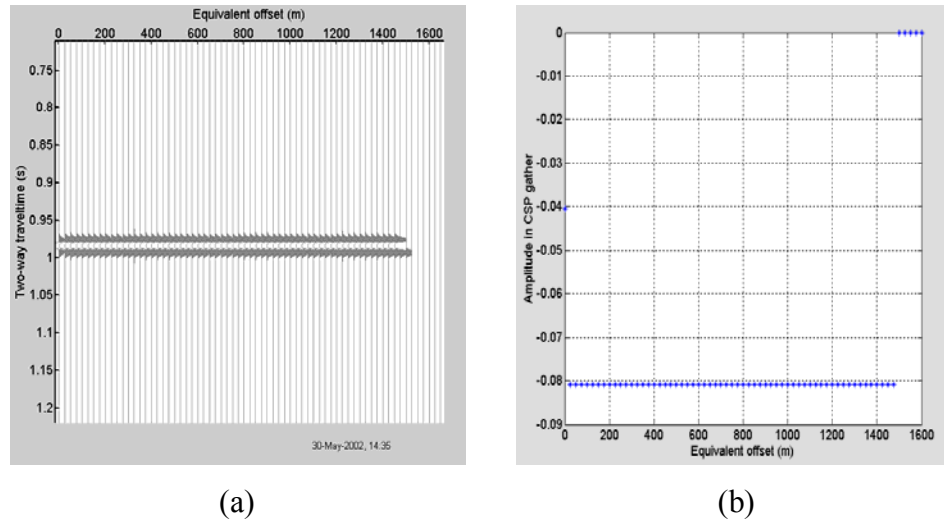
Figure 4.7. A CSP gather formed from the zero-offset section. a)CSP gather; b)
Amplitude in CSP gather.

Figure 4.8 is the constant offset gather with half offset *500m*. Forming a CSP gather from this section, is similar to a zero-offset section. The energy is spread between the zero offset event and the equivalent hyperbola. Most of this energy will destructively cancel, but when more offsets are used, some will align on the equivalent hyperbola. Amplitude from that data is meaningless, except that on the equivalent hyperbola.
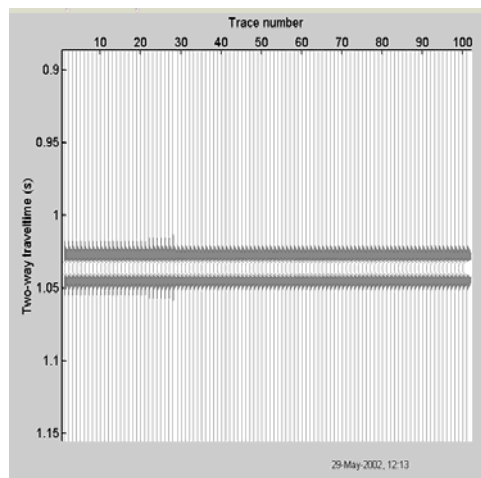
Figure 4.8. Common-offset gather with half offset 500m.

(a)   (b)
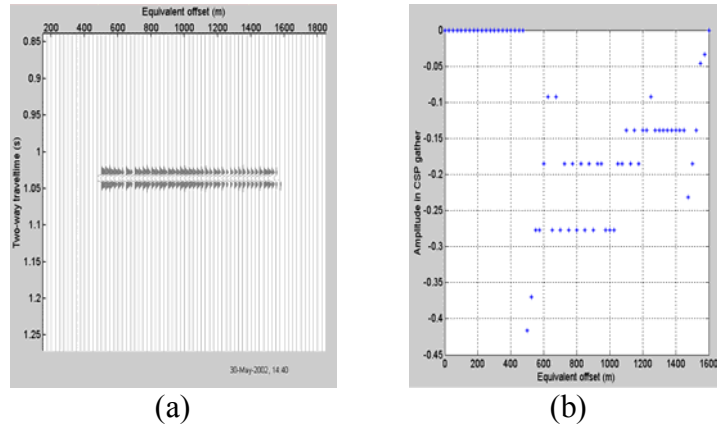
Figure 4.9. CSP gather using the data above. a) CSP gather; b) Amplitude in CSP gather.

For a linear reflector, the reflected energy comes from the Fresnel zone centered at the tangent point. In Chapter 3, using the Fresnel zone concept, the minimum migration aperture was obtained. EOM with a limited migration aperture is called as limited aperture EOM. Here, one thing should be emphasized: EOM has the merit of high fold when used as imaging, but when used as an AVO analysis tool, the aperture should be limited. With the limited aperture, the migration signal also eliminates a lot of non-specular energy. The results for zero-offset and constant-offset data with the limited aperture are depicted in the following figures, where Figure 4.10 shows the zero offset data and Figure 4.11 shows the offset data that is now confined to an area close to the equivalent hyperbola.

(a)   (b)
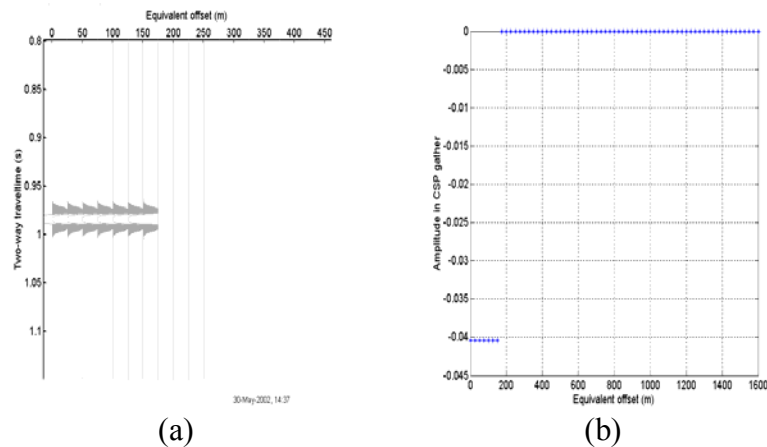
Figure 4.10. CSP gather using zero-offset data with limited aperture. a) CSP gather; b) Amplitude in CSP gather.

(a)   (b)
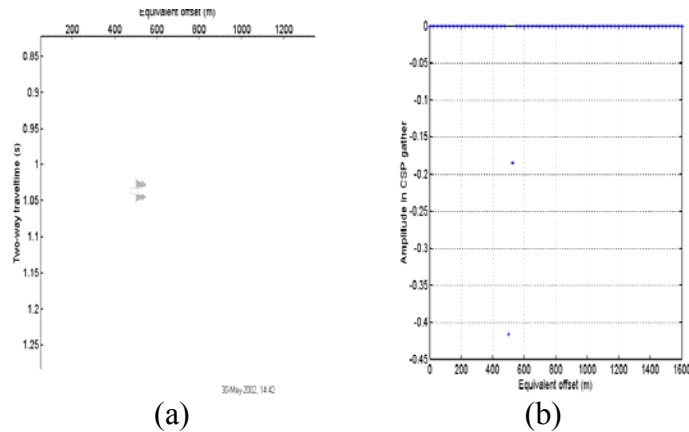
Figure 4.11. CSP gather using 500m offset section with limited aperture. a) CSP gather;

b) Amplitude in CSP gather.

The effect of the limited aperture improving the CSP gather is clearer in the *500 m* offset results. The smearing was reduced to two traces, of which one is at the correct position and the other one is still migration noise. Is there signal lost during limiting the aperture gathering? From both sections above, the amplitude in the CSP gather is larger than it should be, verifying there is sufficient energy. This method was tested with all offsets to form the CSP gather in Figure 4.12, and when compared with the CSP gather with no limited aperture in Figure 4.4b, the migration noise has been significantly reduced. Only near the equivalent offset does it remains. In this sense, limited aperture CSP gathering provides a superior method to obtain the reflectivity.

(a)   (b)
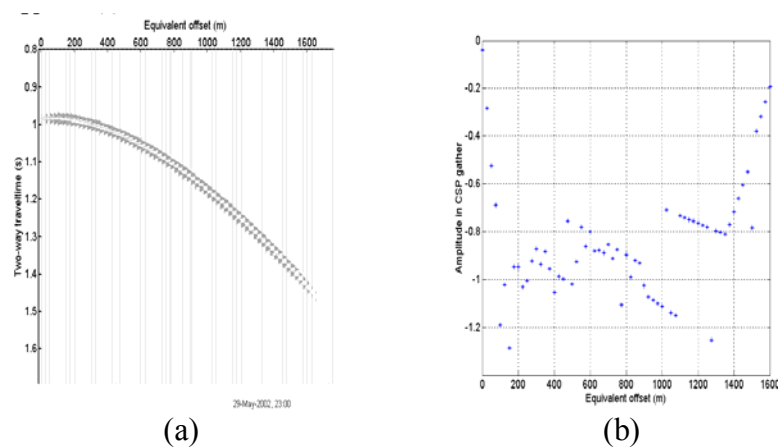
Figure 4.12. CSP gather with limited aperture formed using whole data. a) CSP gather;

b) Amplitude in CSP gather.

4.3 Fold consideration

Fold is considered as another reason for the larger amplitude variations in CSP gathering. In CSP gathering the fold can be calculated sample by sample and becomes larger with equivalent offset. Normally dividing the CSP gather by the fold provides a chance to correct anomalous amplitude in the CSP gather.

Figure 4.13 shows an example of a CSP gather divided by sample-by-sample fold when using a migration aperture that is equal to the Fresnel zone. Observe the amplitude in the CSP gather in Figure 4.13(b), where it is obvious that the amplitude in the CSP gather has been divided by a value that is too large.

(a)   (b)

Figure 4.13. CSP gather divided by fold with the Fresnel zone as aperture. a) CSP gather; b) Amplitude in CSP gather.

This results when the energy, which has been collected into a CSP gather, is both specular energy and noise. The fold, however, is calculated each time when energy is added to the CSP gather. Based on such consideration, a smaller aperture of a half Fresnel zone will be tested. Limiting migration aperture to a half theFresnel zone means not only the energy within the aperture is mainly made of specular energy, but also the

fold calculation can be more reliable. Figure 4.14 shows the plausible results compared with reflectivity indicated by triangles in Figure 4.14(b).
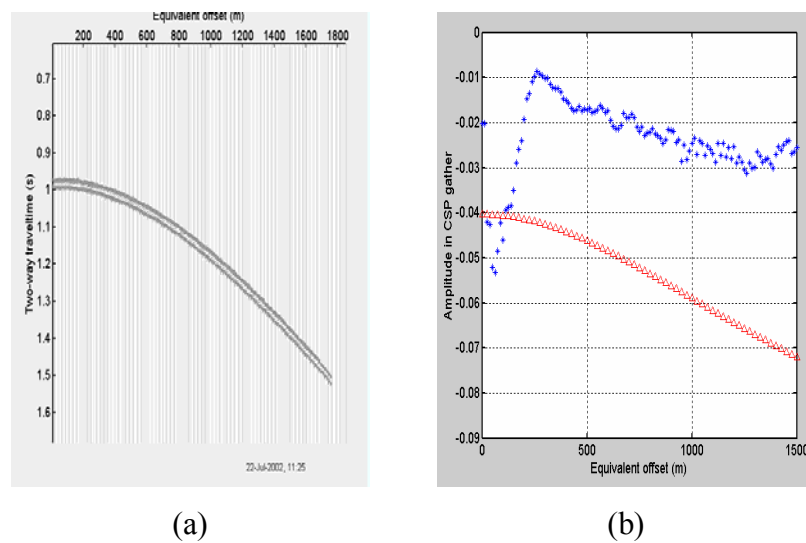

(a)   (b)
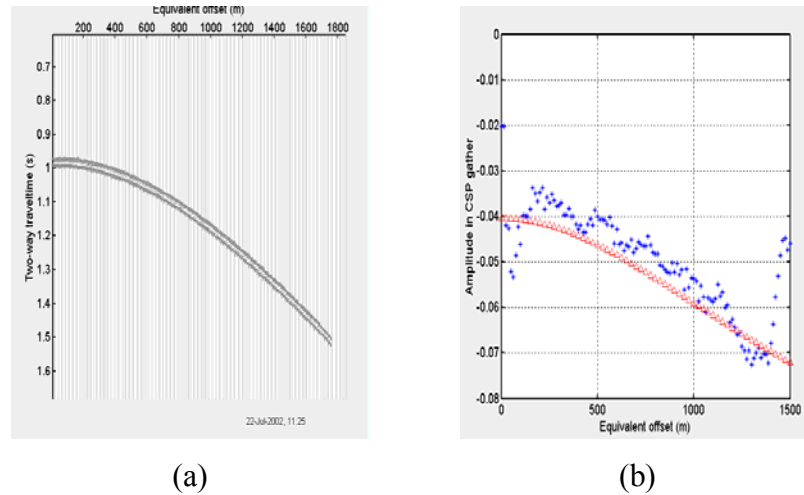
Figure 4.14. CSP gather divided by fold with half the Fresnel zone as aperture. a) CSP gather; b) Amplitude in CSP gather.

When using half the Fresnel zone as the migration aperture, and divided by the sample-by-sample fold, the amplitude in CSP gather approximates reflectivity. This provides a first step in using a CSP gather as an amplitude analysis tool.

Some geophysicists have devoted themselves to developing a true-amplitude migration algorithm for AVO analysis. According to the literature on true-amplitude migration, the weighting function or scaling factor was the most important factor in a Kirchoff migration. In the next part of this Chapter, different scaling factors will be discussed and tested using the same simple model as above.

4.4 Scaling factors during CSP gathering

4.4.1 Post-stack approximation τ/T_n

Li (1999) pointed out, that for CSP gathering, the post-stack migration obliquity factor, the ratio of migration output time τ to the zero-offset time T_n, i.e. τ/T_n is a good

approximation as scaling factor. For CSP gathering this approximation can be expressed as (Li, 1999):

$$scaling = \frac{\tau}{T_n} = \sqrt{\frac{T^2 - \frac{4h_e^2}{V^2}}{T^2 - \frac{4h^2}{V^2}}} = \sqrt{\frac{V^2 T^2 - 4h_e^2}{V^2 T^2 - 4h^2}} \, . \qquad (4.2)$$

Using this scaling factor, and the Fresnel zone as an aperture, there is little improvement in the amplitude of the CSP gather as evident in Figure 4.15.

(a)   (b)

Figure 4.15. CSP gather using the Fresnel zone as an aperture with scaling factor τ/T_n. a) CSP gather; b) Amplitude in CSP gather.

4.4.2 Approximation τ/T

Li (1999) also pointed out that for CSP gathering the extension of post-stack approximation as τ/T, the ratio of migration output time τ directed to traveltime T, can be another good approximation for an offset obliquity factor. For CSP gathering, this scaling factor can be expressed as (Li, 1999):

$$scaling = \frac{\tau}{T} = \frac{\sqrt{T^2 - \frac{4h_e^2}{V^2}}}{T} = \frac{\sqrt{V^2 T^2 - 4h_e^2}}{VT} \, . \qquad (4.3)$$

As in the previous section, the result shows no improvement of the amplitude in CSP gather as Figure 4.16 indicates.

(a)   (b)

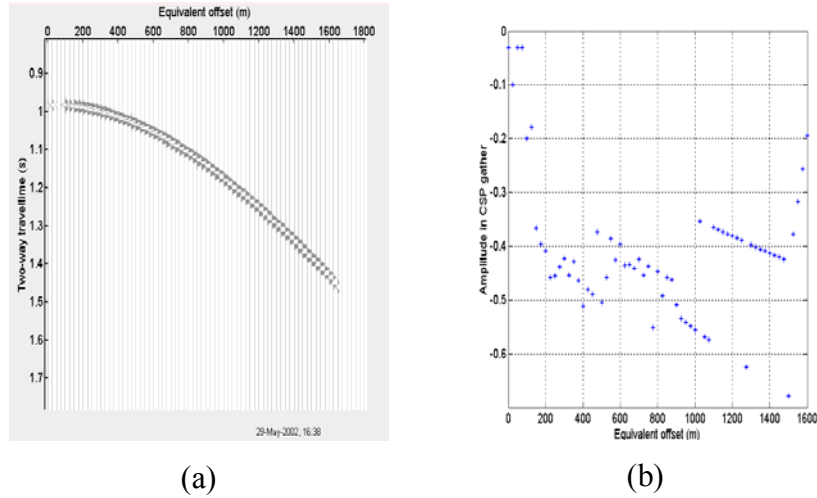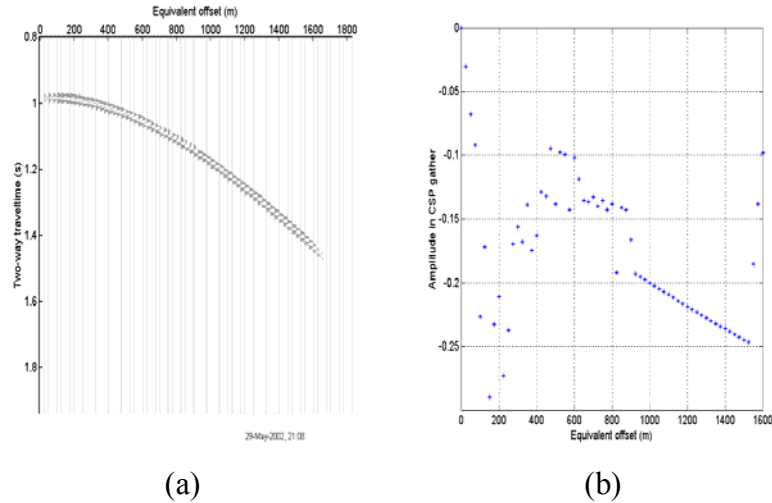*Figure 4.16. CSP gathering using the Fresnel zone as an aperture with scaling τ/T. a)*
CSP gather; b) Amplitude in CSP gather.

4.4.3 Margrave's approach

Margrave (et al., 1999) first introduced the Fourier prestack migration by using the equivalent wavenumber (EWM). He also evaluated the time migration EOM's scaling factor. In the next several pages, his EWM method and time scaling factor approximated from EWM will be introduced in detail.

Margrave (et al., 1999), began this derivation from Stolt prestack wavefield construction as:

$$\psi(x, h = 0, t = 0, z) = \iiint \phi_0(k_x, k_h, \omega) \exp(ik_z z) \exp(ik_x x) dk_x dk_h d\omega, \qquad (4.4)$$

In equation (4.4) the Fourier double square root can be rewritten as a single square root involving an equivalent wavenumber. The equivalent wavenumber k_e can be expressed implicitly as:

$$k_z = \frac{1}{2}\sqrt{k^2 - (k_x - k_h)^2} + \frac{1}{2}\sqrt{k^2 - (k_x + k_h)^2} = \sqrt{k^2 - k_e^2}, \qquad (4.5)$$

where $k=2\omega/v$.

The algebraic solution for k_e is

$$k_e^2 = k_x^2 + k_h^2 + \frac{k_x^2 k_h^2}{k_z^2} = \frac{1}{2}(k_x^2 + k_h^2 + k^2) - \frac{1}{2}\sqrt{(k^2 - k_x^2 - k_h^2)^2 - 4k_h^2 k_x^2}. \quad (4.6)$$

Changing the variables in equation (4.4) from (k_x, k_h, k) to (k_x, k_e, k), the results are

$$\psi(x, h = 0, t = 0, z) = \frac{v}{2} \iint \overline{\phi}(x, k_e, k) \exp(iz\sqrt{k^2 - k_e^2}) dk_e dk, \quad (4.7)$$

where

$$\overline{\phi}(x, k_e, k) = \int f(k_x, k_e, k)\phi_0(k_x, k_h, k) \exp(ik_x x) dk_x, \quad (4.8)$$

and

$$f(k_x, k_e, k) = \frac{k_e}{k_h(k_e)}\left[1 - \frac{k_e^2 - k_h^2(k_e)}{k^2 + k_x^2 - k_e^2}\right], \quad (4.9)$$

with

$$k_h(k_e) = sign(k_e)\sqrt{\frac{[k^2 - k_e^2][k_e^2 - k_x^2]}{k^2 - k_e^2 + k_x^2}}. \quad (4.10)$$

Since

$$\sin(\theta_x) = \frac{k_x}{k} = \frac{2(x - x_0)}{vT}; \; \sin(\theta_h) = \frac{k_h}{k} = \frac{2h}{vT}; \; \sin(\theta_e) = \frac{k_e}{k} = \frac{2h_e}{vT}, \quad (4.11)$$

then the scale function f can be written in space-time domain as

$$f = \frac{\sin(\theta_e)}{\sin(\theta_h)}(1 - \frac{\sin^2(\theta_e) - \sin^2(\theta_h)}{1 + \sin^2(\theta_x) - \sin^2(\theta_e)}). \quad (4.12)$$

Using equation (4.12) as a scaling factor together with the Fresnel zone as aperture, the result shows that except for near offset there are several singular points, the other amplitudes in the equivalent hyperbola are ideal as reflectivity.

(a)   (b)
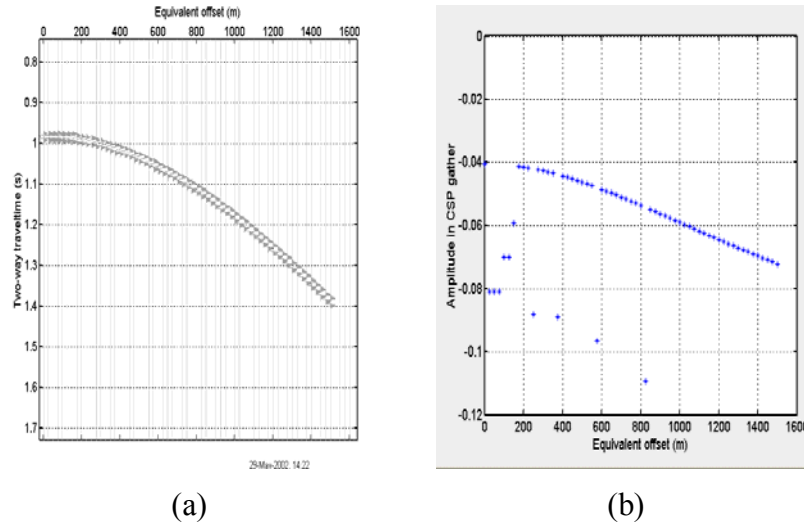
Figure 4.17. CSP gather using scaling factor from EWM. a) CSP gather; b) Amplitude in CSP gather.

4.4.4 Sun's 2D limited aperture migration solution

In Chapter 2, the limited aperture migration concept and Sun's (1998) approach to true-amplitude migration method were introduced. The last scaling factor in this thesis is Sun's approach as equation (4.13). τ'' in equation (4.13) is the second derivative of difference between reflection and diffraction time.

$$scaling = \left| \frac{\tau''(x)}{2\pi} \right|^{\frac{1}{2}}. \tag{4.13}$$

The result of using this scaling factor for CSP gathering is shown in Figure 4.18. The amplitudes of the near offset information tend to zero. Amplitudes in the CSP gather show more coherent amplitude, but the amplitudes do not accurately represent the reflectivity.

(a)   (b)
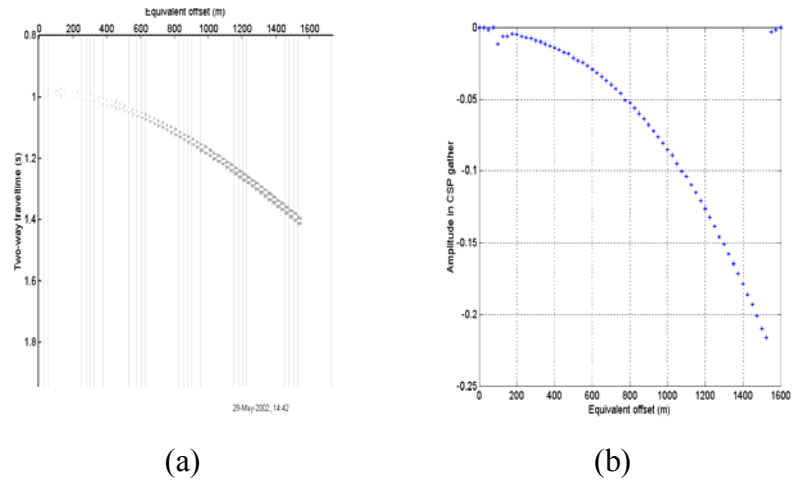
Figure 4.18. CSP gather using all data with scaling equation (4.13). a) CSP gather; b)
Amplitude in CSP gather.

4.5 Scaling by aperture normalization

This approach comes from scaling using aperture normalization. The basic idea is amplitude scaling by the ratio between migration aperture and migration distance x_{off}. Three different approaches will be considered.

4.5.1 The Linear Approach: $1-x_{off}/x_{aper}$

A linear scaling factor $1-x_{off}/x_{aper}$ is first considered as scaling factor during CSP gathering, where x_{aper} denotes migration aperture and x_{off} denotes migration distance. Using this linear approach, the amplitudes are smooth in the CSP gather but their values are not close to the reflectivity.

(a)   (b)
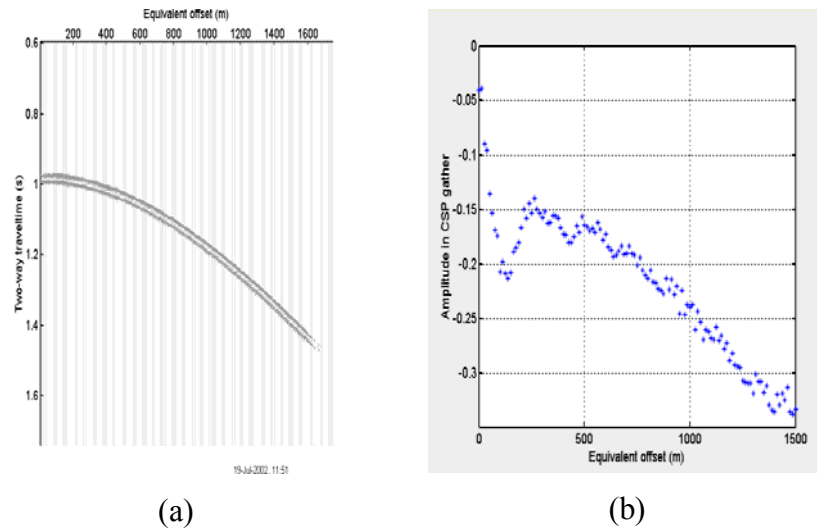
Figure 4.19. CSP gather uses linear approach of aperture normalization with the Fresnel zone as aperture. a) CSP gather; b) Amplitude in CSP gather.

Limiting the aperture to half the Fresnel zone, is also considered with the linear approach but there is no improvement as Figure 4.20a depicts. Similarly enlarging the migration aperture to double Fresnel zone does not improve the amplitude, as shown in Figure 4.20b.

(a)   (b)

Figure 4.20. CSP gather using linear approach with a) half the Fresnel zone as an aperture and b) double the Fresnel zone as an aperture.

4.5.2 The Reciprocal Approach: x_{aper}/x_{off}

In the reciprocal approach, the ratio of migration distance to migration aperture will be used. As x_{off} tends to zero, the reciprocal approach tends to *1*. Also as the migration distance becomes larger the scaling factor becomes smaller. Figure 4.21 shows CSP gather using the reciprocal scaling factor. The next two figures, i.e. Figure 4.22a and b, show poor results with half and double the Fresnel zone as the migration aperture.
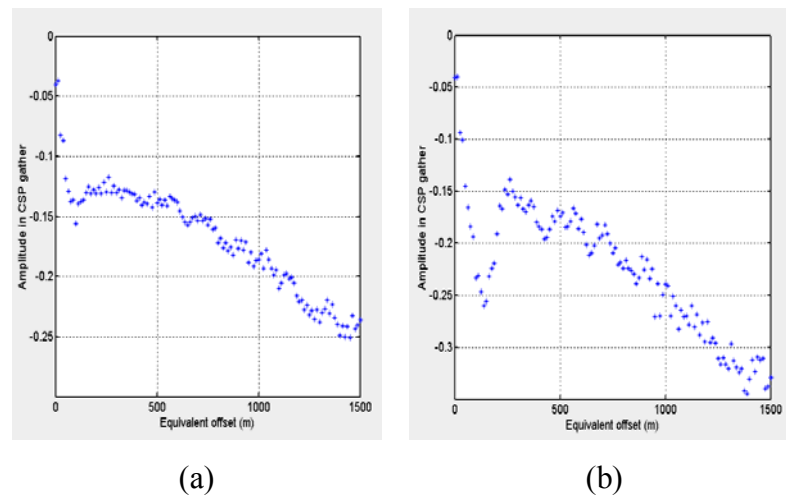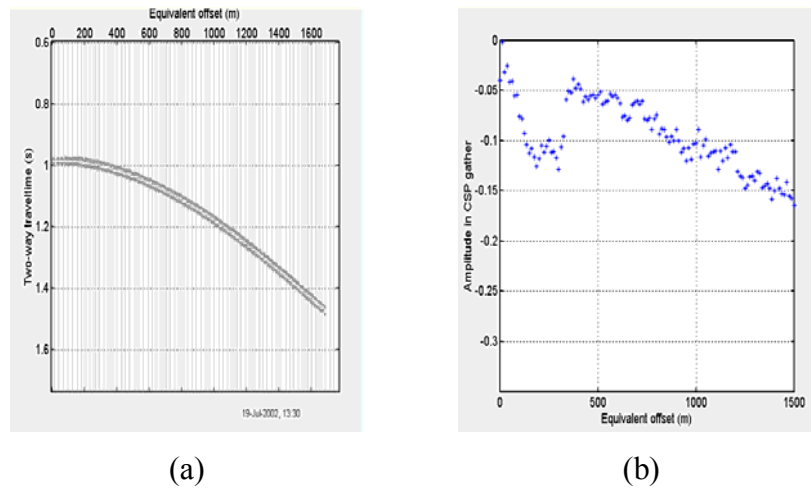

(a)   (b)

Figure 4.21. CSP gather scaled using reciprocal approach with aperture limited to the Fresnel zone. a) CSP gather; b) Amplitude in CSP gather.
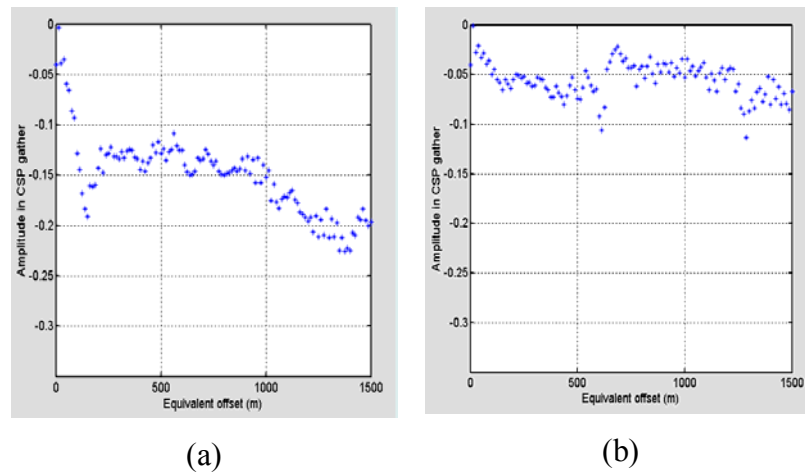

(a)   (b)

Figure 4.22. CSP gather scaled using reciprocal approach with a) half the Fresnel zone as an aperture and b) double the Fresnel zone as an aperture.

4.5.3 The Exponential Approach: $0.25 * e^{(-|x_{off}/x_{aper}|)}$

The third approach to aperture normalization is called the exponential approach, i.e. $0.25 * e^{(-|x_{off}/x_{aper}|)}$. The exponential approach comes from the diffraction theory, as discussed in Chapter 3, that shows the amplitude decreases exponentially within the Fresnel zone with the distance to the edge of the reflector.

The first example in Figure 4.23 shows the result of using the Fresnel zone to define the migration aperture. Amplitude in the CSP gather not only indicates the amplitude anomalies, but also approximates the reflectivity, that is identified by the triangles.

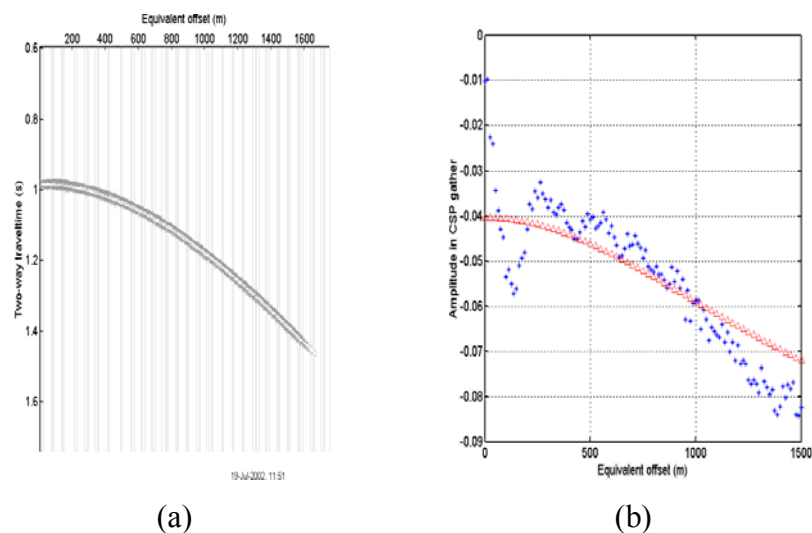(a)   (b)

Figure 4.23. CSP gather uses exponential approach of aperture normalization with the Fresnel zone as aperture. a) CSP gather; b) Amplitude in CSP gather.

Repeating this method using a half and double the Fresnel zone is shown in Figure 4.24. Results are good and tend to approximate the reflectivity.
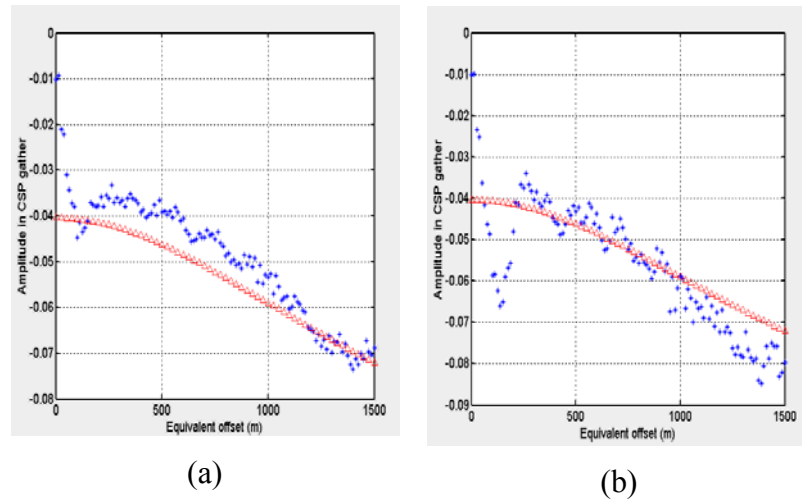
Figure 4.24. CSP gather scaled using exponential approach with a) half the Fresnel zone as an aperture and b) double the Fresnel zone as an aperture.

Discussion

In section 4.6.3 the migration aperture was limited to a certain size. What will happen if the migration aperture is not limited and the exponential approach modified to $0.25 * e^{\left(-\left|x_{off} / x_{fre}\right|\right)}$, in which x_{fre} is the size of Fresnel zone. Figure 4.25 depicts a) the CSP gather, b) the CSP gather after normal moveout correction (NMO) and c) amplitude in the CSP gather. Although migration noise appears in the CSP gather, after NMO correction, the amplitude approximates the reflectivity. Such results indicate that using this modified scaling factor, even with no limited aperture, the CSP gather provides a good match to the reflectivity.
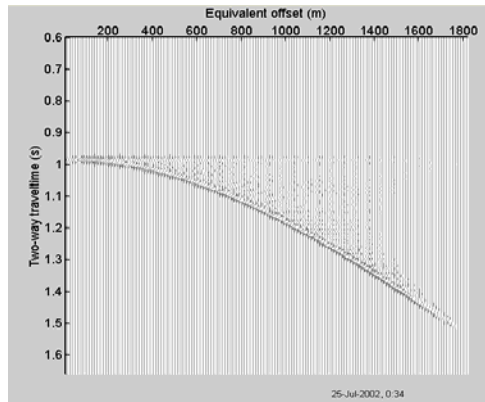
(a)
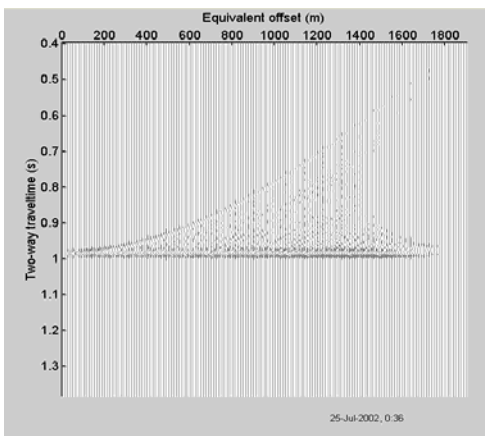
(b)
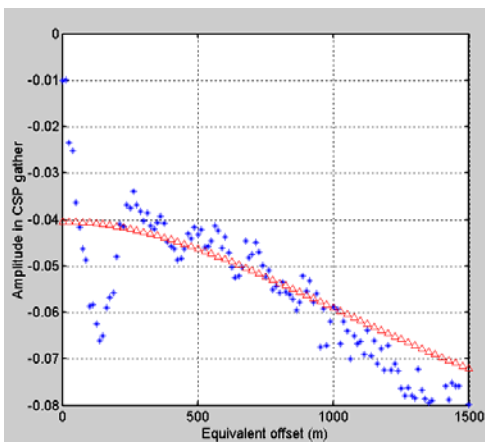
(c)

Figure 4.25. CSP gather scaled by exponential approach but with no aperture limit. a)
CSP gather; b) NMO of CSP gather; c) Amplitude in CSP gather.

4.6 Chapter conclusions

In summary, this Chapter discussed the smearing factors during CSP gathering of migration distance x_{off}.

Three useful approaches were obtained

1. Divided CSP gather by sample-by-sample fold with half the Fresnel zone aperture, amplitude in CSP gather approaches the reflectivity. In this thesis, it is called the first kind of approach to obtain reflectivity in CSP gather.

2. For CSP gathering with a Fresnel zone based aperture, four scaling factors were tested. With EWM's factor the amplitude in CSP gather approaches reflectivity. With Sun's approach there are AVO anomalies but not the reflectivity. With the other two scaling factors, neither the AVO anomalies nor the reflectivity were achieved. In this sense, when using CSP gather for AVO analysis, the best scaling factor is EWM's. This is called the second kind of approach.

3. Another good approximation of scaling during CSP gathering was introduced: exponential scaling within the Fresnel zone. Results show it can provide reflectivity in CSP gather no matter what size of aperture used. This is called the third approach.

4. CSP gather has no spatial limition for AVO analysis.

All three approaches are based on the Fresnel zone concept. To limit migration aperture to the Fresnel zone, tangent point should be located first. For both time and depth migration, the tangent point can be established by using the method described in Katz and Henyey(1992). However this is still a challenge to locate the tangent point. In a mild structure, the size of the Fresnel zone does not change significantly and can be approximated by the horizontal case. Thus, the amplitude in the CSP gather, no matter which kind of approach was used, can be used to estimate the reflectivity.

Chapter 5

Applications and Discussions

5.1 Chapter summary

This chapter will present results of the application of limited aperture CSP gathering to synthetic data and field data. The limited aperture CSP gather will first be applied to the synthetic data, which has a part of gas sand in the middle of the sand layer. Then it will be applied to the Blackfoot data.

All the results show that the method in this thesis provides CSP gather as a stable and reliable AVO analysis tool.

5.2 Part gas sand layer synthetic data

5.2.1 Earth model and acquisition geometry

The experiments presented in this part are based on the simple earth model, called part gas sand layer model as shown in Figure 5. 1. The earth properties are:

P-wave velocities: in Shale *3048 m/s*, in sand (no gas and gas) *2438 m/s*;

S-wave velocities: in Shale *1244 m/s*, in sand no gas *995* m/s, in sand with gas *1625 m/s*;

Densities: in Shale *2.4 g/cm^3*, in sand (no gas and gas) *2.14 g/cm^3*.

According to the Zoeppritz equation, when the *P*-wave travels through subsurface with these earth parameters, the seismic section splits to two parts. With the gas sand, there are strong AVO anomalies, while with no gas sand there is no such phenomena.
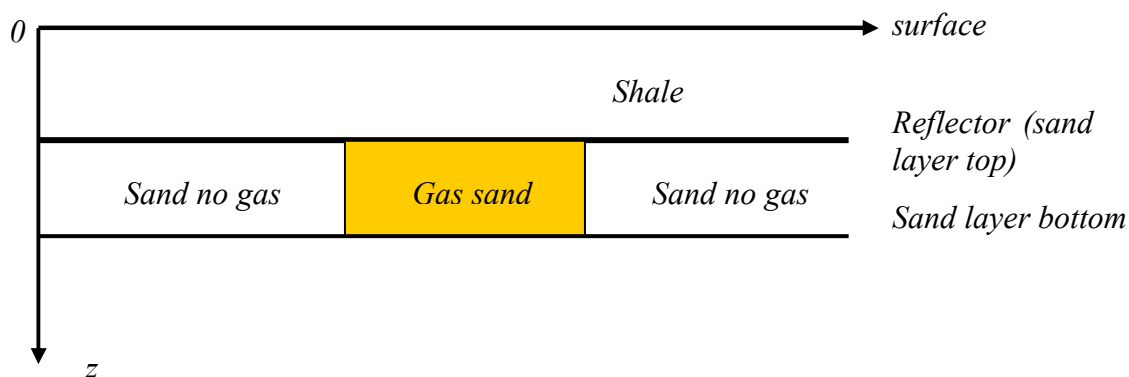
Figure 5.1. Simple part gas sand layer model.

A synthetic dataset is generated. The survey geometry is the same as in the last chapter and illustrated in Figure 5. 2. In this survey, sources and receivers are located in the surface. Receivers are fixed from *0* to *4000* at *25*m intervals. Sources move along the surface from *500*m to *3500*m also at *25*m intervals. This geometry creates prestack data with fold high up to *121*.
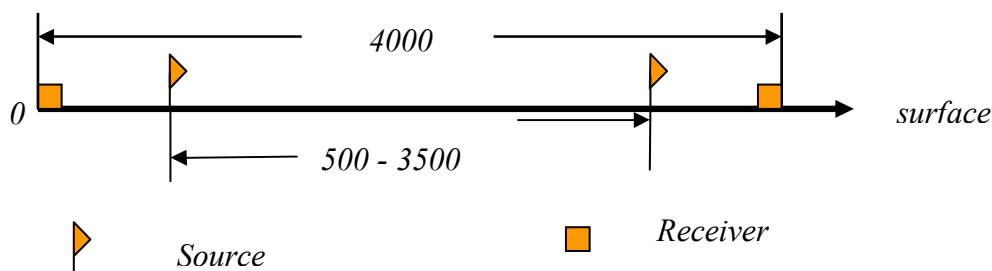
Figure 5.2. Geometry used to acquire a set of data over earth subsurface model shown in Figure 5.1.

The synthetic seismic data is numerically generated using MatLab, in which reflection coefficients calculated by Aki and Richards approximation to the Zoeppritz equation were convolved with the Ricker wavelet with wavelet length *0.04 s*. The time sample rate is *2* milliseconds. Only the primary *P-P* reflection was modeled.

5.2.2 AVO analyses in CMP gather for gas sand

For the horizontal layer, AVO analysis in a CMP gather traditionally provides reliable amplitude information. When the CMP is located within the gas sand, such as the surface location at *1800 m*, the AVO anomalies to be expected are described in Figure 5.3.


(a)   (b)
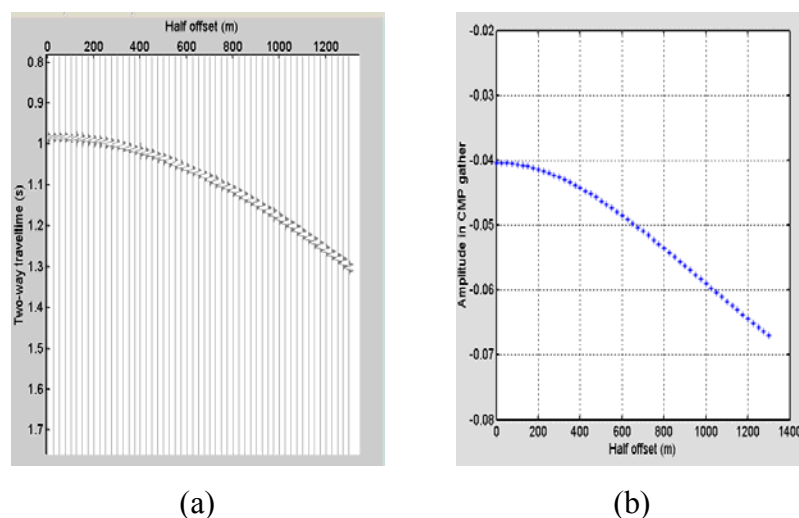
Figure 5.3. CMP gather within gas sand area. a) Seismic section; b) Amplitude varying with half offset.

For this classic gas sand model, reflection coefficients become smaller when half offset or the incident angle increases. The reflection coefficients are negative and become more negative. Half offset h varies from *0* to *1300* meters. Amplitudes, which are reflection coefficients convolved with the Ricker wavelet, vary from *–0.04* to *–0.068*, the trough becomes dramatically larger with half offset h.

5.2.3 AVO analyses in CSP gather for gas sand

As obtained in Chapter 4, there are three approaches in getting correct amplitude in CSP gather. Now the three approaches will be applied to synthetic data separately.

First approach: half the Fresnel zone as aperture divided by fold

A CSP gather was formed in the same location as the CMP gather using the first approach, given the data in Figure 5.4. The triangles represent amplitude in the CMP gather, which are the reflectivity convolved with the wavelet. The amplitude in the CSP gather is a good fit to reflectivity in this circumstance.

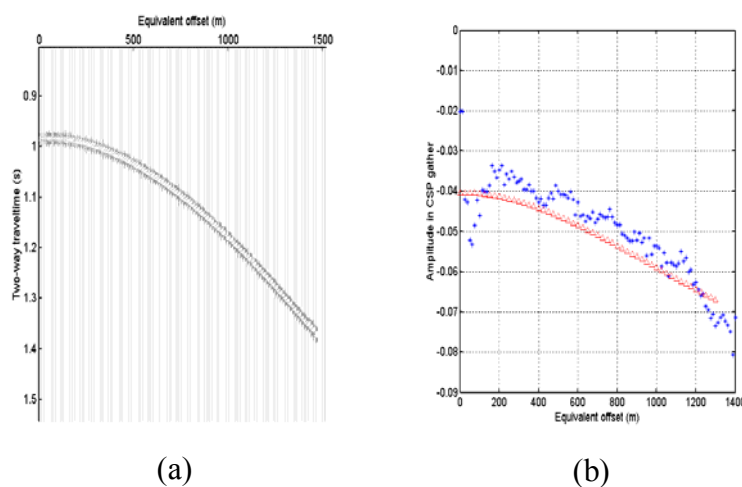| (a) | (b) |

Figure 5.4. CSP gather is formed using first approach in gas sand area. a) CSP seismic section; b) Amplitude in such gather.

Second approach: the Fresnel zone as aperture with scaling factor EWM's

A CSP gather with limited aperture and EWM's scaling factor can provide the accurate amplitude. The amplitude in CSP gather, as expected, are shown in Figure 5.5.

(a)   (b)
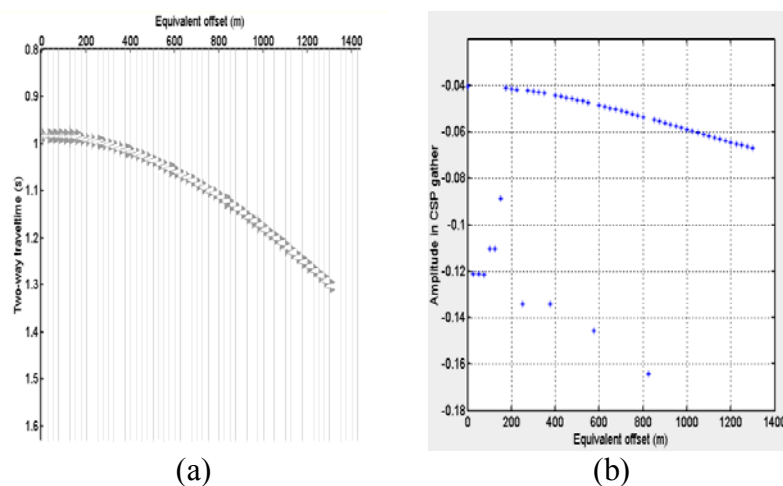
Figure 5.5. CSP gather is formed using EWM's approach in gas sand area. a) CSP seismic

section; b) Amplitudes in CSP gather.

In the amplitude of Figure 5.5b, there are several singularity points with large amplitude at the near equivalent offset. The rest of it is the same as CMP gather's amplitude.

Third approach: the Fresnel zone as aperture with aperture exponential scaling

A CSP gather formed using exponential scaling of aperture can also provide a good fit to reflectivity. Figure 5.6 shows this result. In the CSP gather, the amplitude shows a trend that tends to match the CMP gather, which is in triangles.

(a)   (b)

Figure 5.6. CSP gather is formed using the exponential approach. a) CSP gather; b)

Amplitude in the CSP gather.

In summary, the three approaches applied in the last chapter can provide correct amplitude estimates in the gas sand area.

5.2.4 AVO analyses in CMP gather for no gas sand

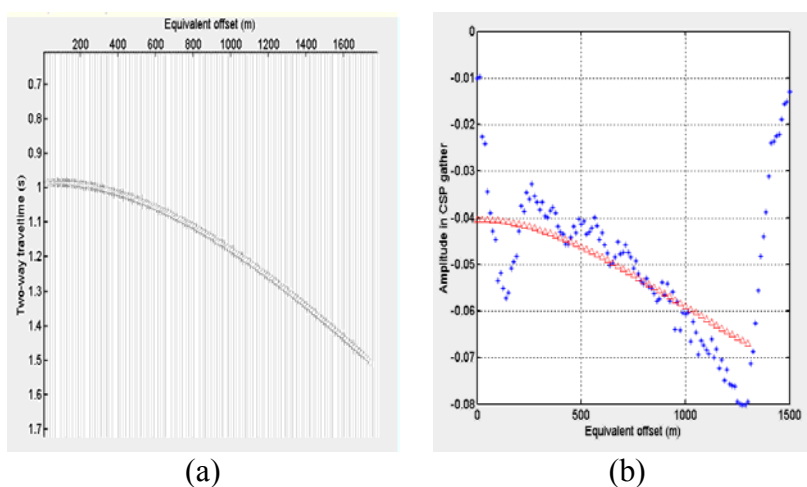The CSP gather is formed in the area for which the lower layer is sand without gas. The reflection from Shale to no gas sand is still negative but now tends to zero with increased offset. The reflection coefficient of normal incidence is the same as from Shale to gas sand. Detailed comparisons for these two kinds of situations were shown in Figure 1.3.

The same procedure used to generate the CMP gather for this no gas sand model is described in the next figures, and the amplitude in CMP gather is described as well. The CMP locates in surface at *2500* m.

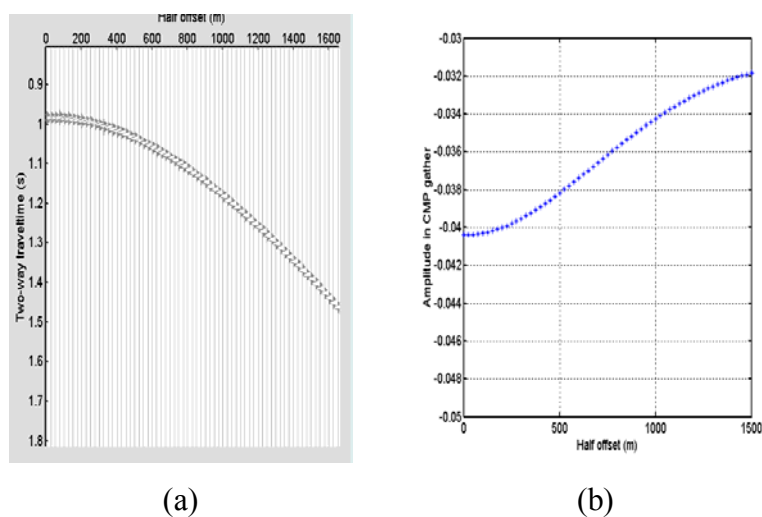(a)   (b)

Figure 5.7. CMP gather within no gas sand area. a) CMP gather at surface location 2500m; b) Amplitude in CMP gather.

Amplitude in this CMP section tends to have a lower value. It varies from *−0.04* to *−0.032* with half offset varying from *0* to *1500* m as illustrated in the theoretical result of Figure 5.7.

5.2.5 AVO analyses in CSP gather for no gas sand

The limited aperture CSP gathering will be applied to form a CSP gather at the surface location *2500m*, the same as the previous CMP gather.

First approach: half the Fresnel zone as aperture with dividing by fold

A CSP gather was formed with half the Fresnel zone aperture and divided by fold with results in Figure 5.9. The amplitude tends to fit the amplitude in the CMP gather.

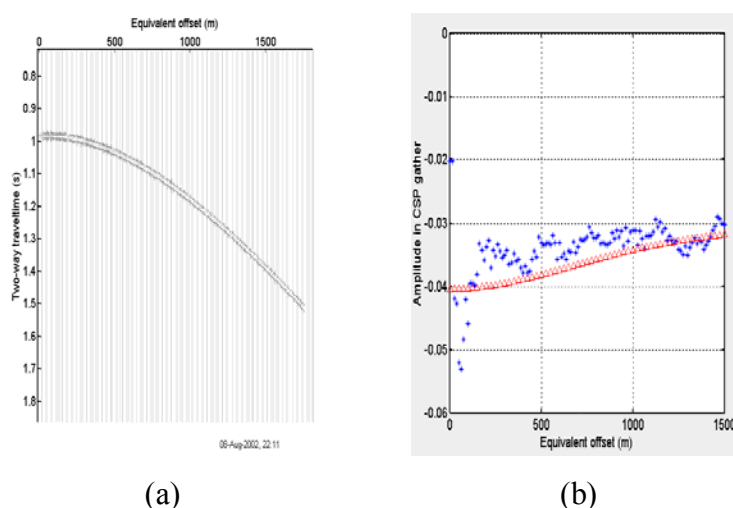(a)   (b)

Figure 5.8.CSP gather is formed using first approach in no gas sand area. A) CSP gather;

b) Amplitude in CSP gather.

Second approach: the Fresnel zone as aperture with EWM's scaling factor

The amplitude and CSP section using EWM's approach are shown in Figures 5.9.

(a)   (b)

Figure 5.9. CSP gather is formed using EWM's approach in no gas sand area. a) CSP seismic section; b) Amplitude in CSP gather.

There are several extreme amplitude points, however, the rest of the amplitude is the same as in CMP gather. This is illustrated in Figure 5.9.

Third approach: the Fresnel zone as aperture with aperture exponential scaling

A CSP gather was formed using aperture exponential scaling and Figure 5.10 represents the results. Amplitude in CSP gather tend to the amplitude in CMP gather, except that the near equivalent offset amplitude in CSP gather is extremely larger than it should be than the rest part of it.
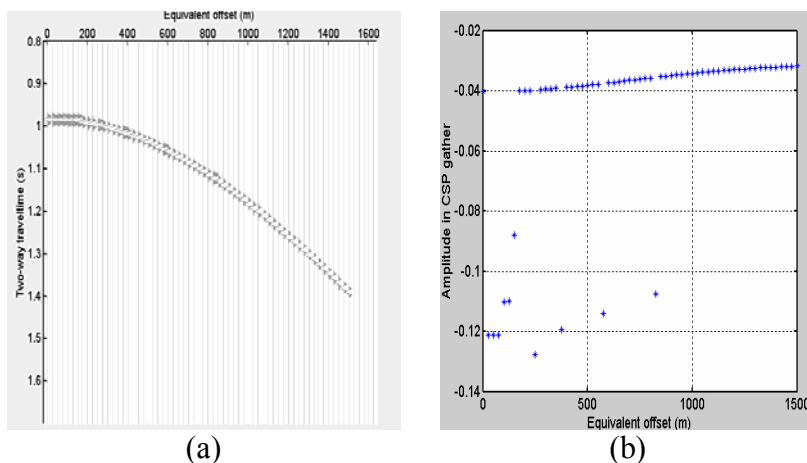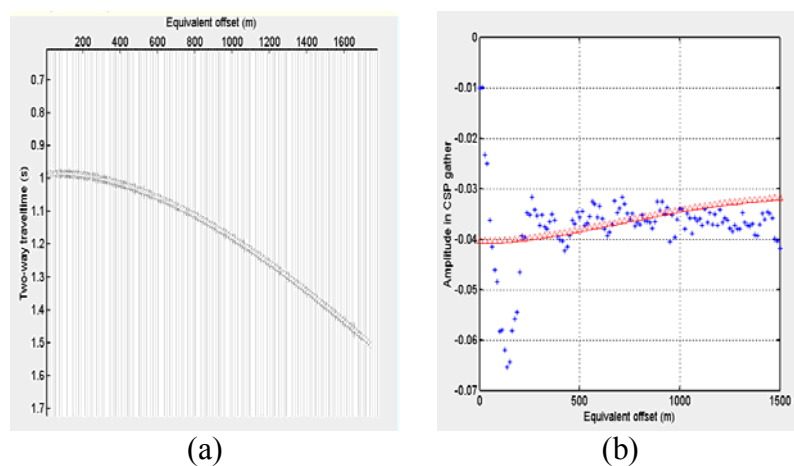

(a)   (b)

Figure 5.10. CSP gather is formed using exponential approach in no gas sand area. a) CSP seismic section; b) Amplitude in CSP gather.

In summary, half the Fresnel zone aperture divided by fold and aperture exponential scaling approaches used to form CSP gather can obtain the correct amplitude. The EWM's approach provides perfect amplitude in CSP gather except for some singular points. Thus the three approaches in this thesis can be used for CSP gathering as AVO analysis tool after prestack migration.

5.3 Blackfoot data example

The Blackfoot data discussed here was acquired in *1997*. The Blackfoot field is located southeast of Calgary, Alberta, in Canada. In this area, the subsurface can be approximated as a layered structure with little lateral velocity variation. In this data set, there are *200* shots and all the *151* receivers are active for each shot. Within this data, an amplitude anomaly can be seen clearly at around *1.0* second. In this section, the amplitude anomaly both in the CMP gather and in the CSP gather after pre-processing will be discussed.

The pre-processing steps include:
1. Elevation statics;
2. True amplitude recovery;
3. Surface consistant deconvolution;
4. TV spectral whitening;
5. Refraction statics;
6. Residual statics;
7. Trim statics;
8. Trace muting.

5.3.1 AVO anomalies in CMP gather

After pre-processing, the CMP locations from *331* to *343* generate a super CMP gather to enhance the amplitudes, as shown in Figures 5.11. An amplitude anomaly is indicated by the rectangle around *1.0* second from absolute offset *650-1100*m.

Figure 5.11a shows the super CMP gather using a wiggle trace display, which amplitude anomaly has a trough that becomes larger with offset. The AVO phenomenon is more visible in the density display in Figure 5.11b.
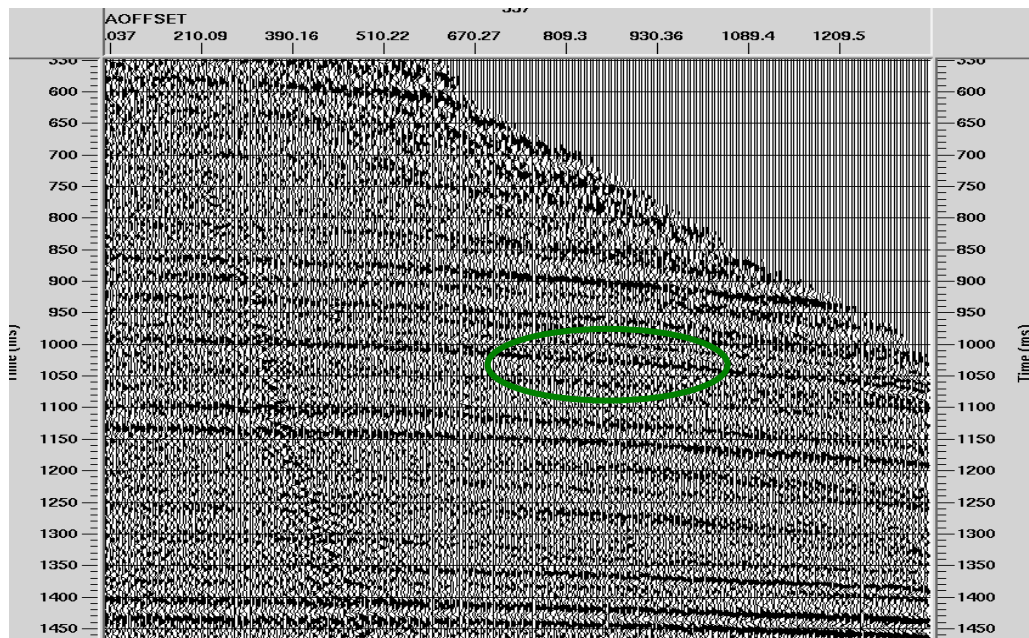
(a)
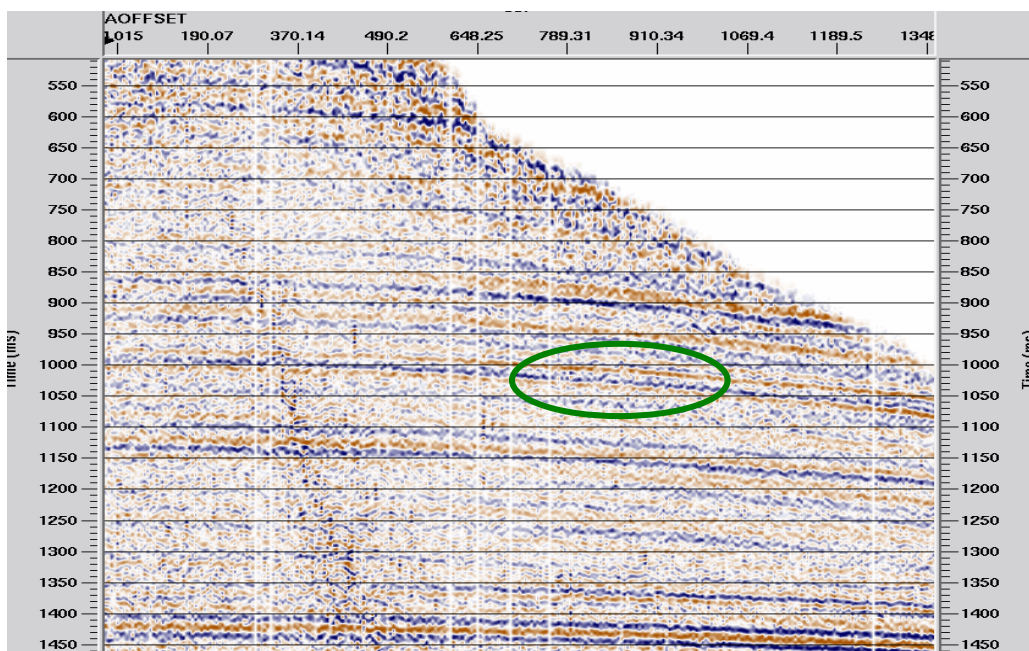
(b)

Figure 5.11. Amplitude anomaly of field data in CMP gather is shown in ellipse. a) As wiggle display; b) Density display.

5.3.2 AVO anomalies in CSP gather

The pre-processing data are used to form a number of CSP gathers in the same locations as the CMP gathers. These gathers are then summed to form a super CSP gather. The three different approaches, which were discussed previously in the above Chapter, will be used to generate CSP gather.

First approach – half the Fresnel zone as aperture divided by fold

The super CSP gather using half the Fresnel zone as aperture divided by fold is shown in Figure 5.12, with the amplitude anomaly again showing in the same ellipse as in the CMP gather. The variable density display clearly represents amplitude anomalies in the circle. In the near offset, because of the method, the amplitude is broken up more than it is in the CMP gather.

(a)

(b)

Figure 5.12. Amplitude anomaly in CSP gather of field data using first approach is shown

in ellipse. a) Wiggle display; b) Density display.

Second approach – EWM's approach

The second approach mentioned in the last Chapter gives perfect results when applied to synthetic data. When scaling the field data with it, the results are depicted in Figures

5.13. Not only is the AVO phenomenon not clear, but also the whole section is full of migration noises. For AVO analysis, no doubt, it is not a good choice. For computation time, it is more than the first and third approaches.

(a)

(b)

Figure 5.13. Amplitude of field data in CSP gather using second approach.
a) Wiggle display; b) Density display.

Third approach – exponential scaling approach

The third amplitude scaling approach that uses exponential scaling is in Figures 5.14. Due to the scaling factor, the near offset amplitude is broken up. In the density display, the AVO phenomenon can be seen clearly from offset *700*m to *1100*m. The main reflector around *1425* msec is also clearly represented.
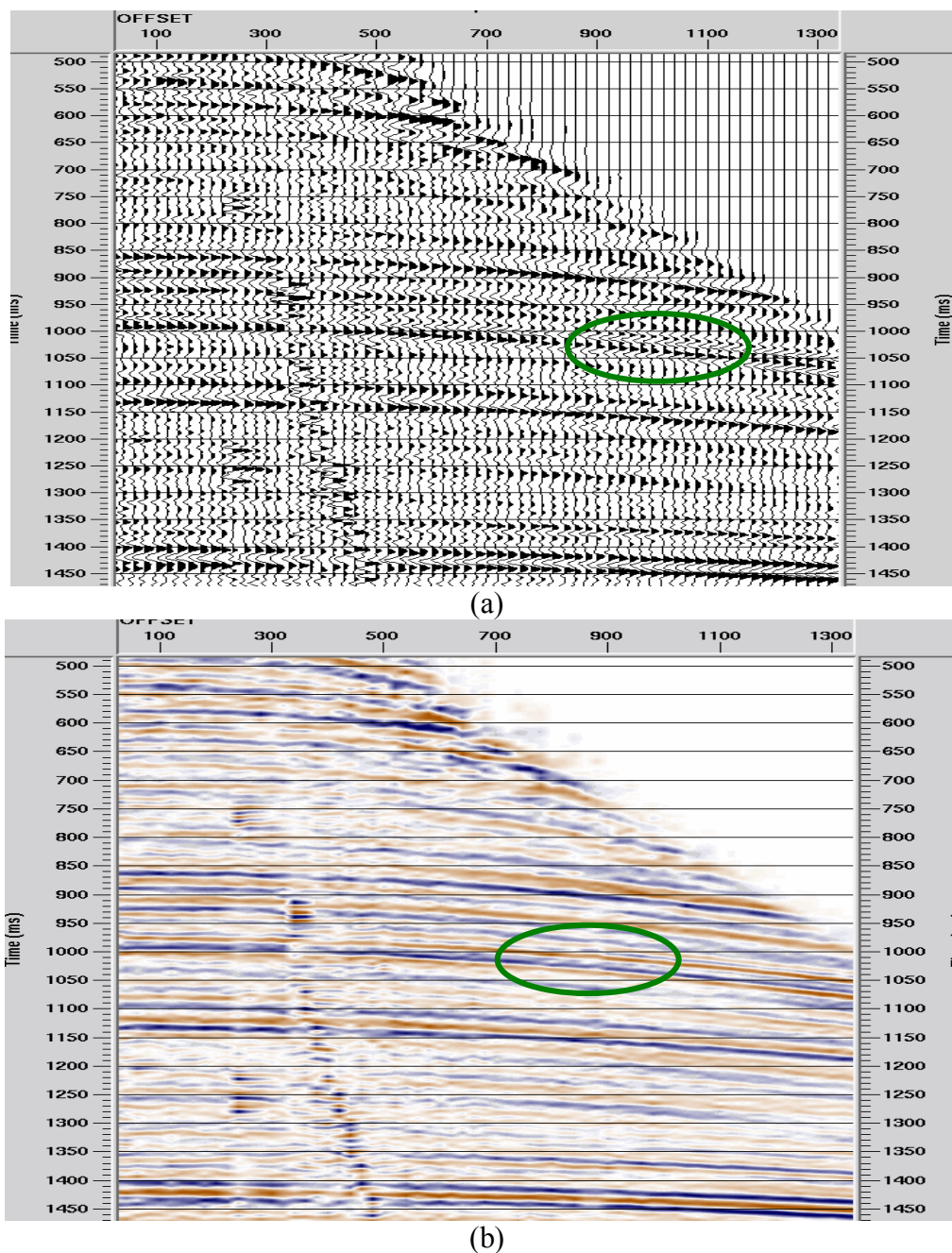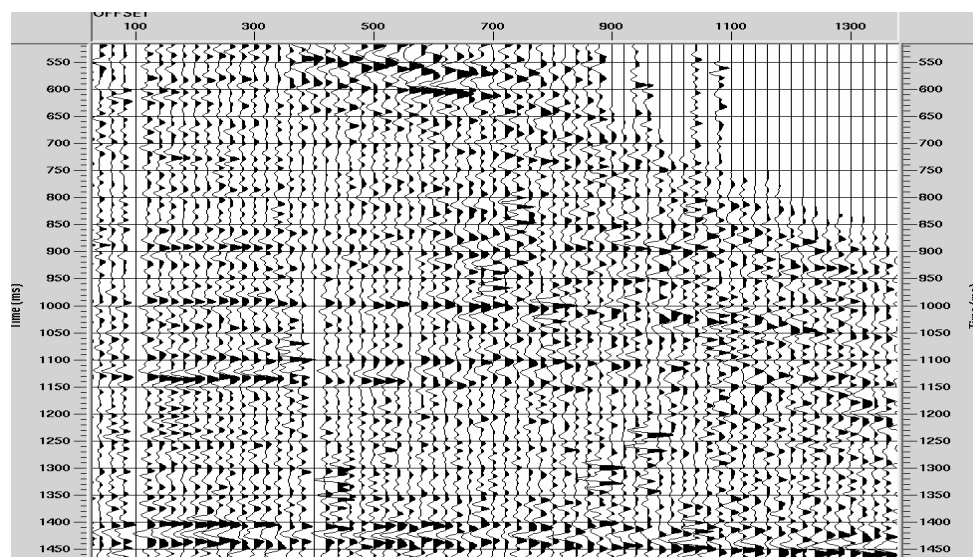

(a)

(b)
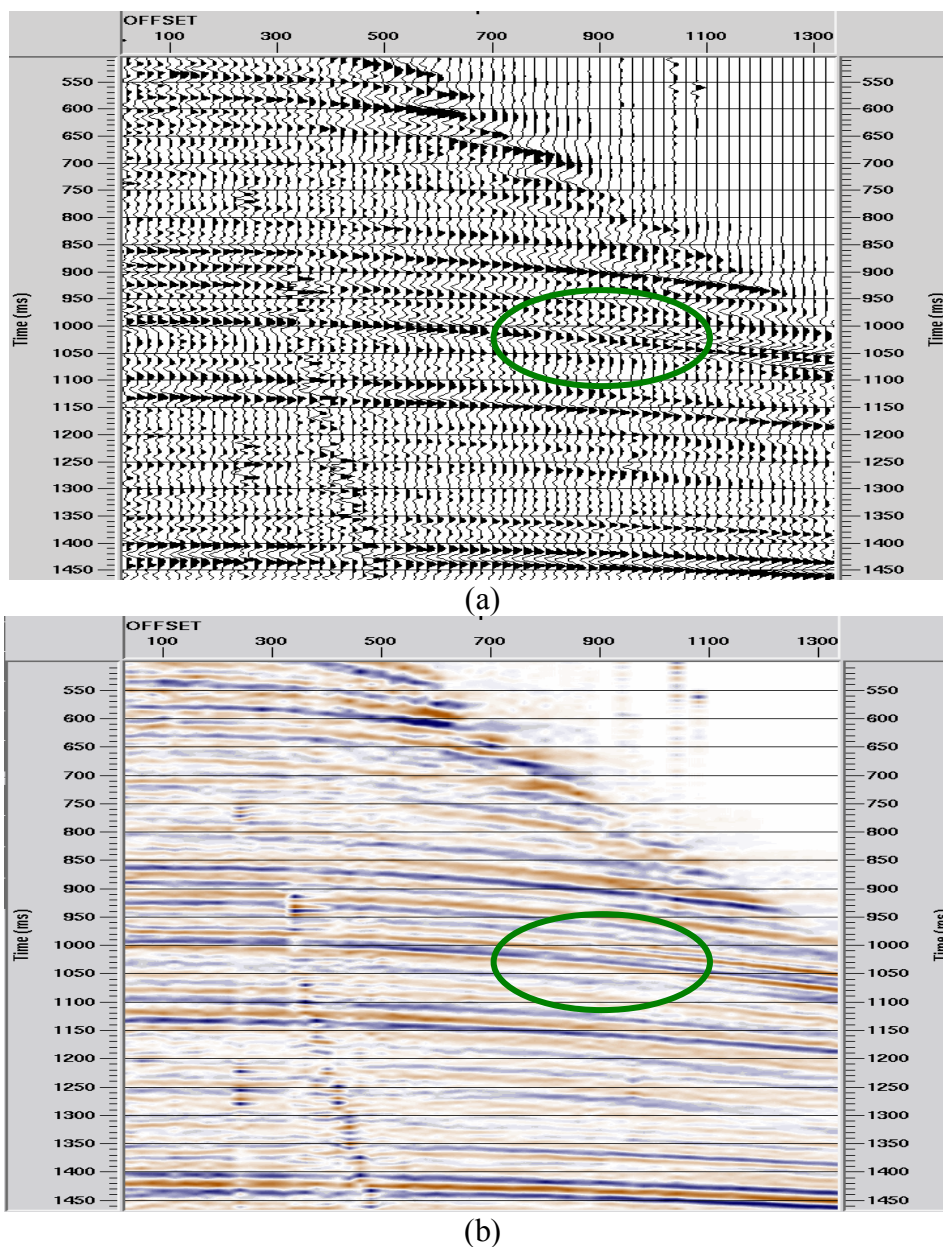
Figure 5.14. Amplitude anomaly in CSP gather of field data using third approach is shown
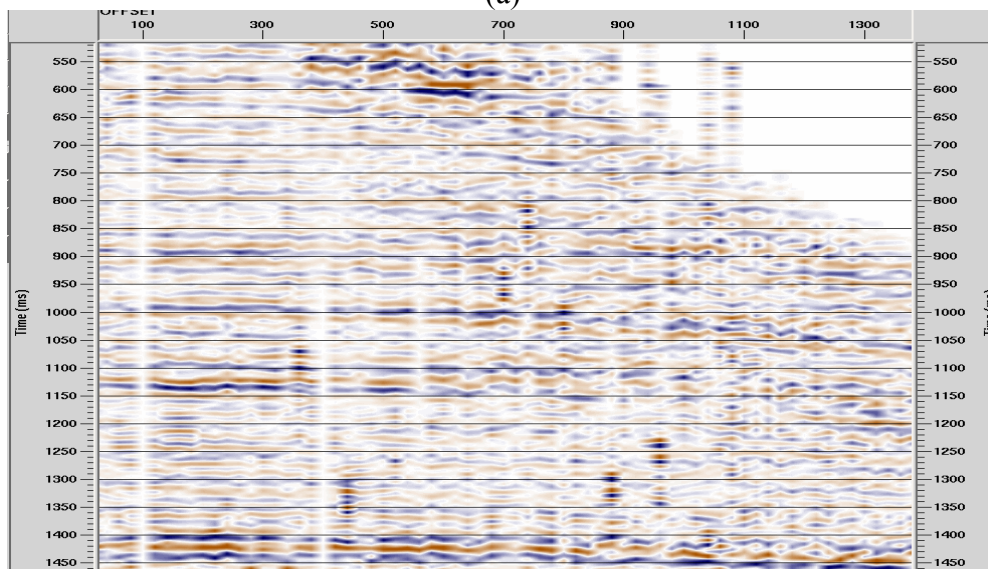
in ellipse. a) Wiggle display; b) Density display.

5.4 Chapter summary

In this Chapter, the limited CSP gathering method was applied both to synthetic data and field data.

The synthetic data has two amplitude phenomena, one with the AVO anomaly and the other without. The results show that the amplitude in the CSP gather is the reflectivity and provide reliable amplitude information.

The field data in the Blackfoot dataset was acquired in 1997. Within this data the AVO anomaly can seen around *1.0* seconds both in CMP gather and the CSP gather. Results show that CSP gathers of field data using half the Fresnel zone as aperture divided by fold and exponential scaling approaches provide the AVO analysis tool as well as in the CMP gather. The EWM's approach is full of migration noises and needs more running time.

Chapter 6

General conclusions

6.1 Conclusions

In this thesis, the CSP gather was examined for use as a tool for AVO analysis. Both synthetic data and field data indicate that CSP gathers, with limited aperture and proper scaling factor, provide a reliable amplitude variation when compared with the CMP gather. The general conclusions include:

1. Seismic reflection is angle dependent. This property leads to the AVO technique as a tool for gas detection or lithology indicator. Geophysicists use the Zoeppritz equations and their approximations as an AVO analysis tool. Among these approximations, Aki and Richards gave a simpler reflectivity approximation of P-P wave.

2. Both the migration aperture and weighting function determine the migration results. In this thesis, the Fresnel zone concept is used to determine the migration aperture both in the zero-offset section and offset section.

   (1). The Fresnel zone size depends on the source wavelet. With a limited band seismic wavelet, summation of the reflected energy reaches its maximum at the radius of the Fresnel zone size. This conclusion is useful for data acquisition design to get the strongest reflected energy.

   (2). The amplitude of reflection is influenced by the reflector size. When the reflector size is smaller than the Fresnel zone, the reflected energy collected is not the reflection coefficient. At the edge of the reflector, the diffraction constructively builds the reflected energy.

(3). The Fresnel zone concept can be expanded to the offset section. The Fresnel zone in prestack data volume, i.e. Cheops Pyramid, is described. With this discussion, it is easy to define the migration aperture in prestack data volume.

(4). The minimum migration aperture should be the size of the Fresnel zone size for prestack migration. The migration aperture larger than this size makes no improvement to migration amplitude.

3. EOM is made up of two main steps: CSP gathering and Kirchhoff NMO to finish the prestack migration. CSP gather not only provides the true subsurface point location but also reliable amplitude. During CSP gathering, similar to other Kirchhoff prestack migration algorithm, both the aperture and scaling factor affect the migration results. In this thesis, minimum migration aperture together with proper scaling factors were investigated.

(1). The smearing factors during CSP gathering depend on the migration distance x_{off}.

(2). Dividing CSP gather by sample-by-sample fold with half the Fresnel zone aperture, amplitude in CSP gather approaches the reflectivity. In this thesis, it is called the first kind of approach to obtain reflectivity in CSP gather.

(3). For CSP gathering with the Fresnel zone aperture, four scaling factors were tested. With EWM's factor the amplitude in CSP gather is reflectivity. With Sun's approach there is AVO anomalies but not the reflectivity. With the other two scaling factors, neither the AVO anomalies nor the reflectivity were achieved. In this sense, using CSP gather as AVO analysis, the best scaling factor is EWM's. It is the second kind of approach.

(4). Another good approximation of scaling during the CSP gathering was introduced: exponential scaling within the Fresnel zone. Results show it can provide reflectivity in CSP gather no matter what size of aperture used. This is the third approach.

(5). All three approaches are based on the Fresnel zone concept. To limit migration aperture to the Fresnel zone, the tangent point should be located first. For both time and depth migration, the tangent point can be established by using the method described in Katz and Henyey(1992). However, how to locate the tangent point effectively is still a challenge for geophysicists. In mild structure, the Fresnel zone does not change too much and can be approximated by the horizontal case. Thus, the amplitude in the CSP gather, no matter which kind of approach was used, can be trusted as reflectivity.

4. The limited CSP gathering method was applied to both the synthetic data and the field data.

(1). The synthetic data has two different AVO phenomena. The results show that the amplitude in the CSP gather is the reflectivity and provides reliable amplitude information.

(2). The field data in the Blackfoot dataset was acquired in *1997*. Within this data, an AVO anomaly can be seen around *1.0* second both in the CMP gather and the CSP gather. Results show that the CSP gathers of the field data using the first and third approaches, provide an AVO analysis tool that matched the CMP gather. The second approach was full of migration noises and required more running time.

References

Aki, K., and Richards, P. G., 1980, Quantitative Seismology: W.H. Freeman and Co., San Francisco, United States.

Bancroft, J. C., Geiger, H. D., Foltinek, D., and Wang, S., 1995, Prestack migration by equivalent offsets and common scatter point (CSP) gathers: 57th Mtg.Eur. Assoc. Expl Geophys., Extended Abstracts, Session: P124.

Bancroft, J. C., 1996, Natural antialiasing in equivalent offset prestack migration: 66th Annual Internat. Mtg., Soc. Expl. Geophys., Expanded Abstracts, 1465-1466.

Bancroft, J.C., 1998a, Dip limits on pre- and poststack Kirchhoff migrations: CREWES Project Research Report, Vol.9, Ch.25.

Bancroft, J.C., 1998b, Computational speed of EOM relative to standard Kirchhoff Migration: CREWES Project Research Report, Vol.9, Ch.43.

Bancroft, J.C., 1998c, Optimum CSP gathers with fixed equivalent offset: CREWES Project Research Report, Vol.9, Ch.44.

Bancroft, J.C. Geiger,H.D. and Margrave, G.F., 1998, The equivalent offset method of Prestack time migration: Geophysics, 63, 2042-2053

Bancroft, J.C., Xu,Y., 1998, Equivalent offset migration for vertical receiver arrays: CREWES Project Research Report,Vol9, Ch.29.

Bancroft, J. C., 1999, Practical understanding of migration and DMO: Course note, SEG Publish.

Berryhill, J.R., 1977, Diffraction response for nonzero separation of source and receiver: Geophysics, 42, 1158-1176.

Bleistein, N., 1987, On the imaging of reflectors in the earth: Geophysics, 52, 931-942.

Born, M., and Wolf, E., 1970, Principles of optics: Pergamon Press, Inc.

Bortfeld, R., 1961, Approximation to the reflection and transmission coefficients of plane longitudinal and transverse waves: Geophys. Prosp., **9**, 485-503.

Castagna, J. P., and Backus, M. M., 1993, AVO analysis-tutorial and review, *in* Castagna, J. and Backus, M., Eds, Offset-dependent reflectivity – Theory and practice of AVO analysis: Soc. Expl. Geophys., 3-37.

Castagna, J.P. and Backus, M.M., 1997, Offset-dependent reflectivity-theory and practice Of AVO analysis, SEG No.8.

Cerveny, V., and Soares, J.E.P., 1992, Fresnel volume ray tracing: Geophysics, 57, 902-915.

Chiburis, E. F., 1984, Analysis of amplitude versus offset to detect gas-oil contacts in Arabia Gulf: 54th Ann. Internat. Mtg., Soc. Expl. Geophys., Expanded Abstracts, 669-670.

Claerbout, J. F., 1978, Fundamentals of geophysical data processing: McGraw Hill Book Co.

Claerbout, J. F., 1985, Imaging the earth's interior: Blackwell Scientific Publications.

Gray, S.H., 1997, True-amplitude seismic migration: A comparison of three approaches: Geophysics, 62, 929-936.

Hagedoorn, J.G., 1954, A process of seismic reflection interpretation: Geophysics Prosp., 2, 85-127

Hanitzsch, C., Schleicher, J., and Hubral, P., 1994, True-amplitude migration of 2-D synthetic data: Geophys. Prosp., 42, 445-462.

Hubral, P., Schleicher, J., Tygel, M., and Hanitzsch, C., 1993, Determination of Fresnel zones from traveltime measurements: Geophysics, 58, 703-712.

Katz, S., and Heyney, T., 1992, Post-stack diffraction-type migration of the signal component of the wavefield: Geophys. J. Internat., 109, 517-524.

Knapp, R. W., 1991, Fresnel zones in the light of broadband data: Geophysics, 56, 354-359.

Knott, C. G., 1899, Reflexion and refraction of elastic waves with seismological applications: Phil. Mag., 48, 64-97.

Koefoed, O., 1955, On the effect of Poisson's ratios of rock strata on the reflection coefficients of plane waves: Geophys. Prosp., 3, 381-387.

Li, X., Residual Statics analysis using prestack equivalent offset migration: 1999, M. Sc. Thesis, University of Calgary.

Lindsey, J. P., 1989, The Fresnel zone and its interpretive significance: The Leading Edge, 33-39.

Margrave, G. F., 1999, The methods of seismic data processing: The Department of Geology and Geophysics, the University of Calgary.

Margrave, G. F., John C. Bancroft and Hugh D. Geiger, 1999, Fourier prestack migration by equivalent wavenumber: Geophysics, 64, 197-207.

Newman, P., 1975, Amplitude and phase properties of a digital migration process: First Break, 8, 397-403.

Ostrander,W.J.,1982,Method for interpretation of seismic records to yield indication of Gaseous hydrocarbons: United States Patent No.4316268.

Ostrander, W. J., 1984, Plane-wave reflection coefficients for gas sands at nonnormal angles of incidence: Geophysics, 49, 1637-1648.

Schleicher, J., Tygel, M., and Hubral, P., 1993, 3-D true-amplitude finite-offset migration: Geophysics, 58, 1112-1126.

Sheriff, R. E., 1980, Nomogram for Fresnel-zone calculation: Geophysics, V 45, P. 968-972.

Sheriff, R. E., 1991, Encyclopedic Dictionary of Exploration Geophysics: Third Edition, SEG Publication.

Shuey, R. T., 1985, A simplification of the Zoeppritz equation: Geophysics, 50, 609-614.

Stolt, R. H., and Weglein, A.B., 1985, Migration and inversion of seismic data: Geophysics, 50, 2458-2472.

Sun, J., and Gajewski, D., 1998, On the computation of the true-amplitude weighting functions: Geophysics, 63, 1648-1651.

Sun, J., 1998, On the limited aperture migration in two dimensions: Geophysics, 63, 984-994.

Sun, J., 2000, Limited-aperture migration: Geophysics, 65, 584-595.

Trorey, A. W, 1970, A simple theory of seismic diffraction: Geophysics, 35, 762-784.

Waters, K. H., 1981, Reflection Seismology: A tool for energy resource exploration: John Wiley & Sons, Inc.

Yilmaz O. 1987. Seismic data processing: Society of Exploration Geophysicists.

Zoeppritz, K., 1919, Erdbebenwellen VIIIB, On the reflection and propagation of seismic waves: Göttinger Nachrichten, I, 66-84.